Phononic Frequency Combs

Adarsh Ganesan

Queens' College

A dissertation submitted to the University of Cambridge in partial fulfilment of the requirements for the degree of

Doctor of Philosophy

Department of Engineering,

University of Cambridge,

Cambridge, United Kingdom

September, 2017

Dedicated to my late Amma

Preface

This dissertation is of the author's own work and contains nothing which is the outcome of work done in collaboration with others, except as declared in the Preface and specified in the text. No part of the work presented in this thesis has already been, or is currently being submitted for any other degree, diploma or qualification. The composition of this dissertation is approximately 17,000 words in length (including figure captions, appendices and references), including a total of 76 figures.

Adarsh Ganesan

Abstract

Optical frequency combs have resulted in significant advances in optical frequency metrology and found wide application to precise physical measurements and molecular fingerprinting. A direct analogue of frequency combs in the phononic or acoustic domain has not been reported to date. This thesis describes a series of results to provide the first clear evidence for the generation of phononic frequency combs in the domain of micromechanical resonators. These results are supported by a theoretical framework which was originally developed to predict the existence of such features of combs in physical systems described by Fermi-Pasta-Ulam dynamics.

The phononic frequency combs is mediated by nonlinear coupling between a primary driven mode and one or more parametrically excited internal modes. We provide experimental evidence for the formation of such phononic frequency combs in systems comprising of 2 or more coupled modes, with results qualitatively consistent with previous numerical studies based on Fermi-Pasta-Ulam dynamics. Additionally, externally pumped comb processes are also reported. Through systematic experiments at different drive frequencies and amplitudes, we portray the well-connected processes of phononic frequency comb formation and define attributes to control their concomitant features. Further, the interplay between these new nonlinear resonances and the well-established Duffing phenomenon is also discussed.

While the experimental verification of the existence of phononic frequency combs is of scientific interest, several potential engineering applications exist including the unique capability to track resonant frequency of a micromechanical resonator without the requirement for an external feedback loop to sustain oscillations at the resonant frequency. The initial experimental results also demonstrate that good short-term frequency stability may be obtained for such micromechanical resonators operated under ambient conditions.

Acknowledgement

I extend my sincere gratitude to my PhD supervisor Prof. Ashwin Seshia for his pivotal role in streamlining the progress of my doctoral research. I would also like to thank my PhD advisor Prof. Eugene Terentjev for his advice and feedback during the start of my doctoral work. I am indebted to my collaborator: Dr. Cuong Danh Do for enlightening technical discussions and morale support.

I would like to thank the members and staff of Queen's College and of Nanoscience Centre for creating a stimulating environment to conduct research on day-to-day basis. Finally, I would like to thank my kind and caring family members including Amma, Appa, Paatis, Thathas and Avinash for providing me with both emotional and financial support in my upbringing.

I would like to acknowledge the Cambridge Commonwealth, European & International Trust for the funding to pursue my PhD study at Cambridge.

Contents

List of Figures

11. Figure 2.4: **Force Applied on a Mass-Spring System.** If force F is applied on the system consisting of mass m and spring k, then the net time-varying displacement (x) of system can be computed based on both Hooke's and Newton's laws.

12. Figure 2.5: **Analogy of Mass-Spring System.** Any physical system can be represented by a coupled mass m – spring k framework. However, the virtual values of m and k are calculated based on the specific properties of physical system under consideration.

13. Figure 2.6: **Disagreement between Theory and Experiment.** A and B: The theoretical and experimental responses respectively.

14. Figure 2.7: **Damped Frequency Responses.**

15. Figure 2.8: **Agreement between Theory and Experiment.** A and B: The theoretical and experimental responses associated with linear resonance respectively.

16. Figure 2.9: **Duffing Phenomenon.** The frequency responses get skewed at large drive levels of P_D. Reprinted figure with permission from [C. Stambaugh and H. B. Chan, *Physical Review B,* vol. 73, p. 172302, 2006.] Copyright (2006) by the American Physical Society.

17. Figure 2.10: **Duffing Phenomenon.** The frequency responses for $\omega_\theta = 1; \zeta_\theta = 0.05; P_D = 1$ and varying levels of β.

18. Figure 2.11: **Parametric Resonance.** A: An electrical signal $S_{in}(\omega_D)$ is injected into a micromechanical resonator; B: The corresponding output response of resonator; C: The displacement amplitude at $\frac{\omega_D}{2}$ as a function of drive power level. When the drive power level is increased above a threshold value Th, the displacement amplitude is increased from '0' to a large value of approximately 30 nm.

19. Figure 3.1: **Fermi-Pasta-Ulam Chain.**

20. Figure 3.2: **Spectral Signature of Frequency Combs.** A-B: The frequency spectra corresponding to phonon modes Q_1 and Q_{10} respectively. Here, $(P_D, \alpha_{FPU}, \omega_D) =$

Here, $S_{in}\left(\frac{\omega_D}{2\pi} = 3.855\ MHz\right) = 4\ dBm; S_{in}\left(\frac{\omega_P}{2\pi} = 3.86\ MHz\right) = 12\ dBm$. Here, $S_{in}\left(\frac{\omega_D}{2\pi} = 3.855\ MHz\right) = 0 - 22\ dBm;\ S_{in}\left(\frac{\omega_P}{2\pi} = 3.86\ MHz\right) = 14\ dBm.$

42. Figure 5.10: **Drive Frequency Dependence.**
The frequency responses corresponding to different drive frequencies $\frac{\omega_D}{2\pi} = 3.85, 3.854, 3.857\ 3.858, 3.859, 3.86, 3.861, 3.862, 3.863, 3.866$ and $3.87\ MHz$ (1-11); $S_{in}\left(\frac{\omega_D}{2\pi}\right) = 4\ dBm; S_{in}\left(\frac{\omega_P}{2\pi} = 3.86\ MHz\right) = 14\ dBm.$

43. Figure 5.11: **Subharmonic Excitations.** A: $S_{in}\left(\frac{\omega_D}{2\pi} = 3.86\ MHz\right) = 15\ dBm;$ B: $S_{in}\left(\frac{\omega_P}{2\pi} = 3.864\ MHz\right) = 15\ dBm.$

44. Figure 5.12: **Observations of Frequency Combs.** Here, $S_{in}\left(\frac{\omega_D}{2\pi} = 3.86\ MHz\right) = 15\ dBm;\ S_{in}\left(\frac{\omega_P}{2\pi} = 3.864\ MHz\right) = 15\ dBm.$

45. Figure 5.13: **Thresholds for Subharmonic Excitations [77].** The displacement contours: A: $S_{in}\left(\frac{\omega_D}{2\pi} = 3.86\ MHz\right) = -15 - 20\ dBm$; B: $S_{in}\left(\frac{\omega_P}{2\pi} = 3.864\ MHz\right) = -15 - 20\ dBm.$

46. Figure 5.14: **Transitional Characteristics of Frequency Combs.** A: The displacement contour: $S_{in}\left(\frac{\omega_D}{2\pi} = 3.86\ MHz\right) = 10\ dBm;\ S_{in}\left(\frac{\omega_P}{2\pi} = 3.864\ MHz\right) = -15 - 20\ dBm$; B-C: The frequency spectra for $S_{in}\left(\frac{\omega_D}{2\pi} = 3.86\ MHz\right) = 10\ dBm;\ S_{in}\left(\frac{\omega_P}{2\pi} = 3.864\ MHz\right) = 0\ dBm$, $S_{in}\left(\frac{\omega_D}{2\pi} = 3.86\ MHz\right) = 10\ dBm;\ S_{in}\left(\frac{\omega_P}{2\pi} = 3.864\ MHz\right) = 12\ dBm$ and $S_{in}\left(\frac{\omega_D}{2\pi} = 3.86\ MHz\right) = 10\ dBm;\ S_{in}\left(\frac{\omega_P}{2\pi} = 3.864\ MHz\right) = 18\ dBm$ respectively.

47. Figure 5.15: **Phononic Frequency Combs via Three-Mode Four-Wave Mixing.** The frequency spectrum of output electrical signal S_{out} for $S_{in}\left(\frac{\omega_D}{2\pi} = 3.857\ MHz\right) = 15\ dBm$; 1-5: The zoomed views of spectral features 1-5 respectively.

48. Figure 5.16: **Drive Level Dependence of Frequency Combs.** The S_{out} contours of frequency combs formed around A: ω_D ; B: ω_m ; C: ω_n respectively for $S_{in}\left(\frac{\omega_D}{2\pi} = 3.857\ MHz\right) = 4 - 23.8\ dBm$. The inset figures show the vibration mode shapes

corresponding to the respective frequency combs and the colours red and blue in these figures correspond to maximum and minimum displacements.

49. Figure 5.17: **Drive Level Dependence of Frequency Combs (Contd.).** A-C: The drive level S_{in} dependence of $\frac{\omega_{n+}}{2\pi}$, $\frac{\omega_m}{2\pi}$, $\frac{\omega_m+\omega_{n+}}{2\pi}$ respectively. Here again, $S_{in}\left(\frac{\omega_D}{2\pi} = 3.857\ MHz\right) = 4 - 23.8\ dBm$.

50. Figure 5.18: **Frequency Comb Spacing.** The spacing of frequency combs formed around ω_m, ω_n and ω_D respectively. Here again, $S_{in}\left(\frac{\omega_D}{2\pi} = 3.857\ MHz\right) = 4 - 23.8\ dBm$.

51. Figure 5.19: **Frequency Comb Spacing (Contd.).** The spacing of frequency combs for $S_{in}\left(\frac{\omega_D}{2\pi} = (3.85\ MHz - 3.865\ MHz)\right) = 4 - 23.8\ dBm$. The absence of colour or white-colour indicates the absence of frequency comb for that drive condition. The dotted black line indicates the parametric resonance threshold. The drive level S_{in} above this threshold line leads to the excitation of $\frac{\omega_m}{2\pi}$ and $\frac{\omega_{n+}}{2\pi}$.

52. Figure 5.20: **Comb vs. Non-Comb Processes.** A-C: The value of $\frac{\omega_m}{2\pi}$, $\frac{\omega_{n+}}{2\pi}$ and $\frac{\omega_m+\omega_{n+}}{2\pi}$ for different drive frequencies $\frac{\omega_D}{2\pi}$ and drive levels S_{in} respectively. The colour-maps indicate the values of these frequencies. The absence of colour or white-colour indicates the absence of frequency comb for that drive condition. The sketched planes correspond to the nominal $\frac{\omega_D}{2\pi}$ dependence of $\frac{\omega_m}{2\pi}$, $\frac{\omega_{n+}}{2\pi}$ and $\frac{\omega_m+\omega_{n+}}{2\pi}$ i.e. in the absence of three mode four-wave mixing. Note: The projections of 3-D plots on the $S_{in} - \frac{\omega_D}{2\pi}$ plane are also shown for clarity.

53. Figure 5.21: A-B: Phononic frequency combs via two-mode pumped three-wave mixing and three-mode pumped four-wave mixing respectively.

54. Figure 5.22: A-B: Phononic frequency combs via two-mode three-wave mixing and two-mode pumped three-wave mixing respectively; C: Coexistence of A and B.

55. Figure 5.23: A-B: Phononic frequency combs via two-mode three-wave mixing and three-mode four-wave mixing respectively; C: Coexistence of A and B.

List of Abbreviations

LR	Linear Resonance
DP	Duffing Phenomenon
PR	Parametric Resonance
FPU	Fermi-Pasta-Ulam
PFC	Phononic Frequency Comb
FEM	Finite Element Method
LCC	Leadless Chip Carrier
LDV	Laser Doppler Vibrometer
DNR	Direct Nonlinear Resonance
PL	Poincare-Lindstedt

List of Symbols

Chapter 1: Introduction

ω_{off}	Offset Frequency of Frequency Combs
$\Delta\omega$	Equidistant Frequency of Frequency Combs
ω_{known}	Known Frequency of a Laser
$\omega_{unknown}$	Unknown Frequency of the Target Light
ω_{θ}	Resonant Frequency of a Mode θ
$\delta\omega_{FO}$	Measured Level of Resonant Frequency Fluctuations using Feedback Oscillator Topology
$\delta\omega_{PFC}$	Measured Level of Resonant Frequency Fluctuations using Phononic Frequency Combs

Chapter 2: Established Resonant Phenomena

ω_{θ}	Resonant Frequency of a Mode θ
F_D	Amplitude of Oscillatory Force
ω_D	Frequency of Oscillatory Force
g	Acceleration due to Gravity
L	Length of the rope of a Swing
m	Mass of an Object

k	Spring Constant of an Object
x	Displacement of the Object
$x_{F_0}^{(H)}$	Extension of Spring due to Force F_0
$x_{2F_0}^{(H)}$	Extension of Spring due to Force $2F_0$
$x_{F_0}^{(N)}$	Displacement of Mass due to Force F_0
F	Applied Force
γ	Coefficient of Damping
x_A	Amplitude of Oscillatory Displacement
ζ_θ	Damping Ratio of a Mode θ
P_D	Amplitude of Oscillatory Drive
β	Cubic Nonlinear Coefficient
S_{in}	Electrical Drive Power Level
Th	The Threshold Value of Electrical Drive Power Level for Parametric Resonance
ω_x	Resonant Frequency of Mode x
ω_y	Resonant Frequency of Mode y
ζ_x	Damping Ratio of Mode x
ζ_y	Damping Ratio of Mode y
α_{yy}	Quadratic Nonlinear Coefficient of Mode y
α_{yx}	Quadratic Coupling Coefficient between Modes y and x
ϵ	Detuning Level for Parametric Resonance
μ	Ratio of Exponential Growth of Amplitude associated with Parametric Resonance

Chapter 3: Fermi-Pasta-Ulam Chains and Phononic Frequency Combs

m	Mass of a Particle
k	Spring Constant associated with the Coupling of Masses m
α_{FPU}	Quadratic Nonlinear Coefficient of Fermi-Pasta-Ulam Chain
β_{FPU}	Cubic Nonlinear Coefficient of Fermi-Pasta-Ulam Chain
Q_q	Displacement of Mode q
ω_q	Resonant Frequency of Mode q
$A_{q,i,j}$	Coefficient of Quadratic Coupling between Modes i and j which affects the Motion of Mode q
$B_{q,i,j,k}$	Coefficient of Cubic Coupling among Modes i, j and k which affects the Motion of Mode q
ζ_q	Damping Ratio of Mode q
P_D	Amplitude of Oscillatory Drive
ω_D	Frequency of Oscillatory Drive
N_{eff}	Effective Phonon Number
$\widetilde{\omega}_q$	Amplitude Dependent Resonant Frequency of Mode q

Chapter 5: Observation of Phononic Frequency Combs in a Micromechanical Resonator

α_{FPU}	Quadratic Nonlinear Coefficient of Fermi-Pasta-Ulam Chain
Q_q	Displacement of Mode q
ω_q	Resonant Frequency of Mode q

$A_{q,i,j}$	Coefficient of Quadratic Coupling between Modes i and j which affects the Motion of Mode q
ζ_q	Damping Ratio of Mode q
P	Drive
P_D	Amplitude of Oscillatory Drive
ω_D	Frequency of Oscillatory Drive
P_P	Pump Amplitude
ω_P	Pump Frequency
$\Delta\omega$	Equidistant Frequency Spacing of Frequency Combs
ω_i	Resonant Frequency of Mode i
$\widetilde{\omega}_i$	Amplitude Dependent Resonant Frequency of Mode i
S_{in}	Electrical Drive Power Level
ω_m, ω_n, ω_{n+}	Self-Excited Frequencies associated with Three-Mode Four-Wave Mixing
ω_1	Resonant Frequency of Mode 1
$\widetilde{\omega}_1$	Amplitude Dependent Resonant Frequency of Mode 1
ω_2	Resonant Frequency of Mode 2
ω_3	Resonant Frequency of Mode 3
ω_4	Resonant Frequency of Mode 4
δ_{PFC}	Detuning Threshold for Phononic Frequency Combs

Chapter 6: Conclusion

ω_1	Resonant Frequency of Mode 1
$\widetilde{\omega}_1$	Amplitude Dependent Resonant Frequency of Mode 1

ω_2	Resonant Frequency of Mode 2
ω_3	Resonant Frequency of Mode 3
ω_4	Resonant Frequency of Mode 4
ω_D	Frequency of Oscillatory Drive
ω_P	Pump Frequency

Chapter 7: Future Work

α_{FPU}	Quadratic Nonlinear Coefficient of Fermi-Pasta-Ulam Chain
Q_q	Displacement of Mode q
ω_q	Resonant Frequency of Mode q
$A_{q,i,j}$	Coefficient of Quadratic Coupling between Modes i and j which affects the Motion of Mode q
ζ_q	Damping Ratio of Mode q
P	Drive
P_D	Amplitude of Oscillatory Drive
ω_D	Frequency of Oscillatory Drive
A_q	Amplitude of Oscillatory Motion associated with Mode q
ω_θ	Frequency of Oscillatory Motion associated with a Mode θ
A_θ	Amplitude of Oscillatory Motion associated with a Mode θ
S_{in}	Electrical Drive Power Level
σ	Allan Deviation associated with Phononic Frequency Comb based Resonant Tracking
τ	Integration Time

Appendix B: Analytical Formulation of Two-Mode Three-Wave Mixing

α_{FPU}	Quadratic Nonlinear Coefficient of Fermi-Pasta-Ulam Chain
Q_a	Displacement of Mode a
Q_b	Displacement of Mode b
ω_a	Resonant Frequency of Mode a
ω_b	Resonant Frequency of Mode b
$\widetilde{\omega}_a$	Amplitude Dependent Resonant Frequency of Mode a
ζ_a	Damping Ratio of Mode a
ζ_b	Damping Ratio of Mode b
$A_{i,j,k\in\{a,b\}}$	Coefficient of Quadratic Coupling between Modes j and k which affects the Motion of Mode i
P_D	Amplitude of Oscillatory Drive
ω_D	Frequency of Oscillatory Drive
$\Delta\omega$	Equidistant Frequency Spacing of Frequency Combs

Appendix C: Analytical Formulation of Two-Mode Pumped Three-Wave Mixing

α_{FPU}	Quadratic Nonlinear Coefficient of Fermi-Pasta-Ulam Chain
Q_a	Displacement of Mode a

Q_b	Displacement of Mode b
ω_a	Resonant Frequency of Mode a
ω_b	Resonant Frequency of Mode b
ζ_a	Damping Ratio of Mode a
ζ_b	Damping Ratio of Mode b
$A_{i,j,k\in\{a,b\}}$	Coefficient of Quadratic Coupling between Modes j and k which affects the Motion of Mode i
P	Drive
P_D	Amplitude of Oscillatory Drive
ω_D	Frequency of Oscillatory Drive
P_P	Pump Amplitude
ω_P	Pump Frequency
$\Delta\omega$	Equidistant Frequency Spacing of Frequency Combs

Appendix D: Analytical Formulation of Three-Mode Four-Wave Mixing

α_{FPU}	Quadratic Nonlinear Coefficient of Fermi-Pasta-Ulam Chain
Q_a	Displacement of Mode a
Q_b	Displacement of Mode b
Q_c	Displacement of Mode c
ω_a	Resonant Frequency of Mode a
ω_b	Resonant Frequency of Mode b

ω_c	Resonant Frequency of Mode c
$\widetilde{\omega}_a$	Amplitude Dependent Resonant Frequency of Mode a
ω_m	A Self-Excited Frequency, close to ω_b, associated with Three-Mode Four-Wave Mixing
ω_n	A Self-Excited Frequency, close to ω_c, associated with Three-Mode Four-Wave Mixing
ζ_a	Damping Ratio of Mode a
ζ_b	Damping Ratio of Mode b
ζ_c	Damping Ratio of Mode c
$A_{i,j,k\in\{a,b,c\}}$	Coefficient of Quadratic Coupling between Modes j and k which affects the Motion of Mode i
P_D	Amplitude of Oscillatory Drive
ω_D	Frequency of Oscillatory Drive
$\Delta\omega$	Equidistant Frequency Spacing of Frequency Combs

Note: The additional symbols including A, B_1 and B_2 are also used in the text and are defined in situ.

List of Publications and Pre-prints

Pre-prints

[1] Adarsh Ganesan and Ashwin Seshia, “Tracking the Resonant Frequency of a Micromechanical Resonator using Phononic Frequency Combs,” arXiv:1710.07058, 2017.

[2] Adarsh Ganesan, Cuong Do and Ashwin Seshia, “Towards N-Mode Parametric Electromechanical Resonances,” arXiv:1708.01660, 2017.

[3] Adarsh Ganesan, Cuong Do and Ashwin Seshia, “Phononic Four-Wave Mixing,” arXiv:1610.08008, 2016.

Peer-Reviewed Journal Articles

[4] Adarsh Ganesan and Ashwin Seshia, "Coexistence of Multiple Multimode Nonlinear Mixing Regimes in a Microelectromechanical Device," *Applied Physics Letters*, vol. 112, no. 8, p. 084102, 2018.

[5] Adarsh Ganesan, Cuong Do and Ashwin Seshia, "Phononic Frequency Comb via Three-Mode Parametric Resonance," *Applied Physics Letters,* vol. 112, no. 2, p. 021906, 2018.

- Featured Article
- Featured in *AIP Scilight*

[6] Adarsh Ganesan, Cuong Do and Ashwin Seshia, “Excitation of Coupled Phononic Frequency Combs via Two-Mode Parametric Three-Wave Mixing,” *Physical Review B,* vol. 97, no. 1, p. 014302, 2018.

[7] Adarsh Ganesan, Cuong Do and Ashwin Seshia, "Excitation of Multiple 2-Mode Parametric Resonances by a Single Driven Mode," *Europhysics Letters,* vol. 119, no. 1, p. 10002, 2017.

[8] Adarsh Ganesan, Cuong Do and Ashwin Seshia, "Frequency Transitions in Phononic Four-Wave Mixing," *Applied Physics Letters,* vol. 111, no. 6, p. 064101, 2017.

[9] Adarsh Ganesan, Cuong Do and Ashwin Seshia, "Phononic Frequency Comb via Intrinsic Three-Wave Mixing," *Physical Review Letters,* vol. 118, no. 3, p. 033903, 2017.

- Editors' Suggestion
- Featured in *APS Physics*
- Awarded the *2017 John Winbolt Prize*, University of Cambridge

[10] Adarsh Ganesan, Cuong Do and Ashwin Seshia, "Observation of Three-Mode Parametric Instability in a Micromechanical Resonator," *Applied Physics Letters,* vol. 109, no. 19, p. 193501, 2016.

[11] Adarsh Ganesan, Gokulnath Rajendran, Ari Ercole and Ashwin Seshia, "Multifrequency Acoustics as a Probe of Mesoscopic Blood Coagulation Dynamics," *Applied Physics Letters*, vol. 109, no. 6, p. 063701, 2016.

Peer-Reviewed Conference Proceedings

[12] Adarsh Ganesan and Ashwin Seshia, "Experimental Mapping of the Operational Regimes of Phononic Frequency Combs," *IEEE International Frequency Control Symposium (*IFCS*)* (2018) (Accepted)

[13] Adarsh Ganesan and Ashwin Seshia, "A Proposal for Absolute Inertial Imaging using Two Mechanical Modes," *IEEE International Frequency Control Symposium* (IFCS) (2018) (Accepted)

[14] Adarsh Ganesan and Ashwin Seshia, "Hysteresis in Phononic Frequency Combs," *European Frequency and Time Forum (EFTF)*, 2017 (Accepted)

- Shortlisted for the Best Paper Award

[15] Adarsh Ganesan, Cuong Do and Ashwin Seshia, "Observation of Phononic Frequency Combs in a Micromechanical Resonator," *Joint Conference of the European Frequency and Time Forum & IEEE International Frequency Control Symposium (EFTF–IFCS),* p. 148-152, 2017.

- Shortlisted for the Best Paper Award

[16] Cuong Do, Adarsh Ganesan and Ashwin Seshia, "Low Power Sub-Milligram Resonant MEMS Load Sensor," *the 19th International Conference on Solid-State Sensors, Actuators and Microsystems – Transducers,* p. 974-977, 2017.

[17] Adarsh Ganesan, Cuong Do and Ashwin Seshia, "Observation of Intrinsic Mode Splitting in a Standalone Micromechanical Resonator," *IEEE International Frequency Control Symposium (IFCS)*, p. 1-4, 2016.

- Shortlisted for the Best Paper Award

Peer-Reviewed Conference Abstracts

[18] Adarsh Ganesan and Ashwin Seshia, "Phononic Frequency Combs," *2018 APS March Meeting,* Los Angeles, USA

- Shortlisted for the 2018 *APS GSNP Student Speaker Award*
- Awarded the *2018 IET Travel Award*

[19] Gokulnath Rajendran, Adarsh Ganesan, Jerome Charmet, Abhinav Prasad, Ashwin A. Seshia and Ari Ercole, "Detection of Fibrinolysis by Quartz Crystal Microbalance," *2016 Euroanaesthesia Congress,* London, UK

Chapter 1

Introduction

1.1. What are Frequency Combs?

Frequency combs refer to a collection of precisely positioned equidistant spectral lines (Figure 1.1).

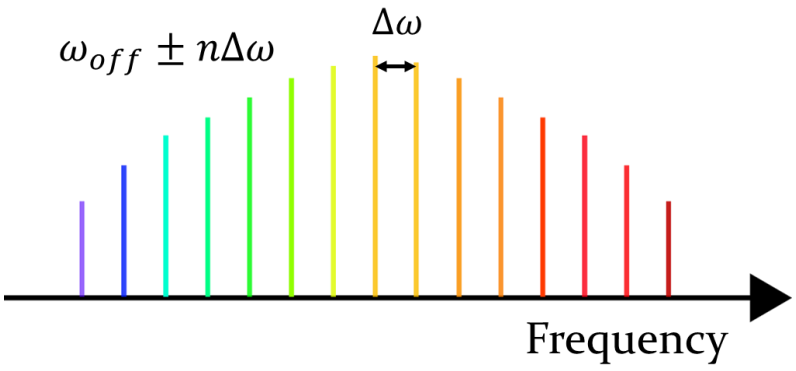

Figure 1.1: **Spectral Signature of Frequency Combs.** The precisely positioned spectral lines of equidistant spacing $\Delta\omega$.

The component tones of frequency combs are defined by one of the frequencies $\omega_{off} + n\Delta\omega; n \in Z$. Here, ω_{off} and $\Delta\omega$ are the offset frequency and frequency spacing associated with the frequency combs respectively.

In addition to the equidistant nature of spectral lines in a frequency comb, such lines are also phase-coherent i.e. have '0' phase difference. Hence, in the time domain, the frequency combs take the form of a 'pulse train'. This feature is pictorially demonstrated in Figure 1.2.

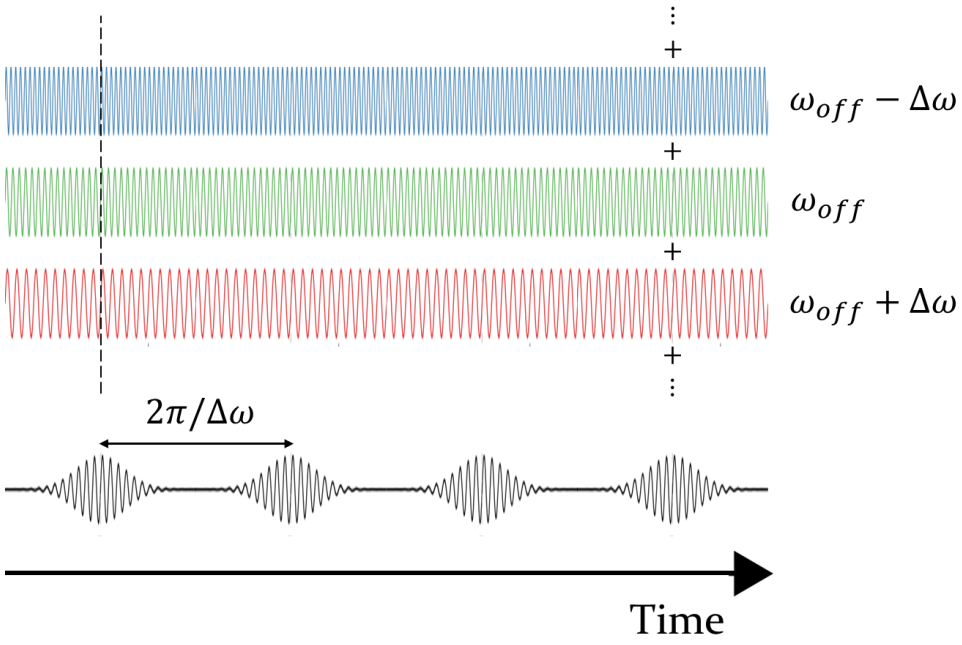

Figure 1.2: **Temporal Signature of Frequency Combs.** The train of pulses with period $2\pi/\Delta\omega$.

1.2. Why are Frequency Combs so Popular?

While existing electronic measurement techniques can address metrology at low frequencies (microwave regime and below), the applicability does not extend to probing fast oscillations for e.g. electromagnetic radiation with frequencies in the THz or above. As a result of this limitation, the precise estimation of high frequencies was limited. The optical frequency combs have thankfully addressed this by providing the equivalent of a ruler in the frequency domain [1-4].

In frequency comb based light metrology, a laser of known frequency is first stabilized. This stabilized laser then interacts with the target light in a nonlinear optical medium. Such interactions result in a frequency comb of spacing corresponding to the difference between the laser's known frequency ω_{known} and target light's unknown frequency $\omega_{unknown}$ (Figure 1.3). Hence, through the low frequency beat-note $\omega_{known} - \omega_{unknown}$ detection, the target light $\omega_{unknown}$ can be precisely probed and the precision of such a measurement will only be largely limited by the stability of probe laser (ω_{known}) [5-8].

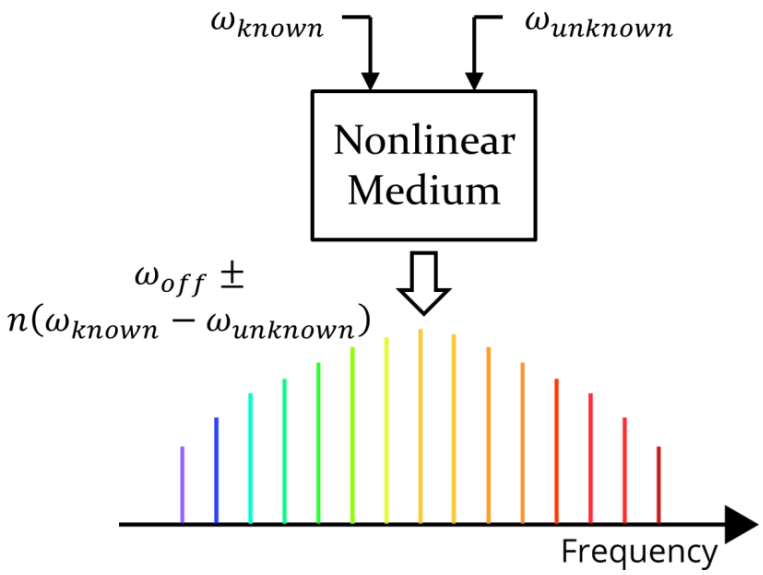

Figure 1.3: **Generation of Optical Frequency Combs.**

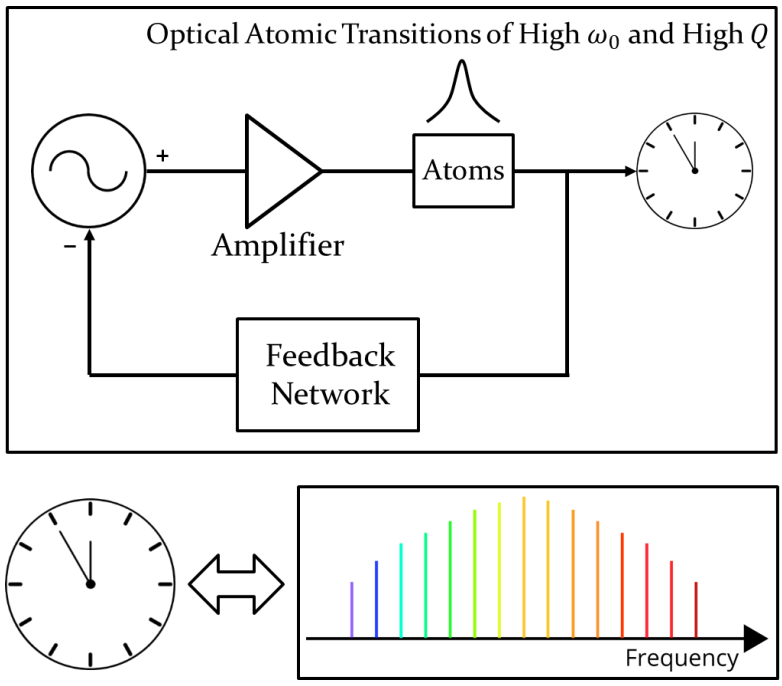

Figure 1.4: **Optical Frequency Combs as a Counter of Optical Atomic Transitions.**

Soon after the development of optical frequency comb metrology, several new fields that involve light measurement opened up. These include ultrafast optics [9] and laser astrophysics [10]. In addition, frequency comb metrology is fundamental to the development of optical atomic clock that oscillates at about 500,000 billion cycles per second and thus, also enabling

the smallest measure of time (Figure 1.4) [11]. Owing to the significance of optical frequency combs to the scientific and technological development, the inventors received the 2005 Nobel prize in physics [4,12].

1.3. Our Experimental Discovery of Phononic Frequency Combs

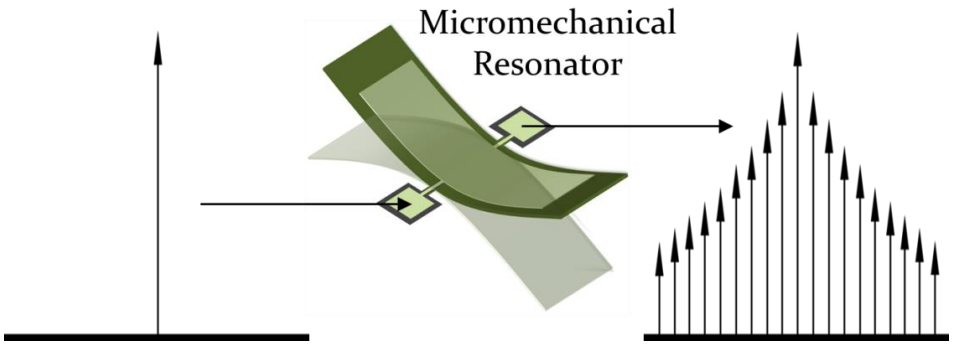

Figure 1.5: Emergence of Phononic Frequency Combs in a Micromechanical Resonator.

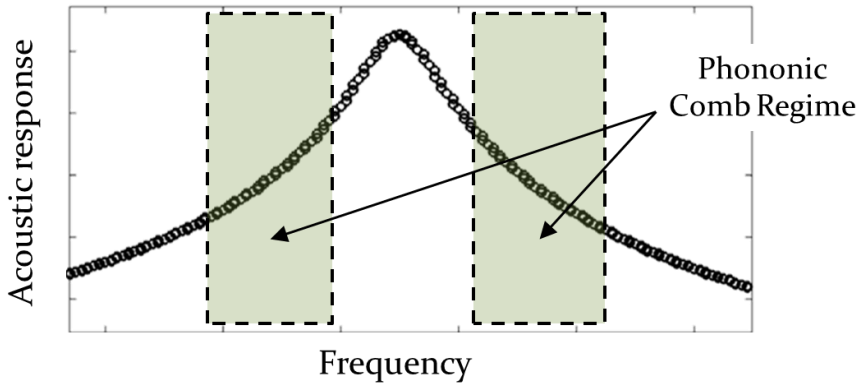

Figure 1.6: Regimes of Phononic Frequency Combs in a Micromechanical Resonator. The off-resonant drive of a phonon mode of micromechanical resonator results in phononic frequency combs.

This decades-old optical frequency comb, by its manifestation as a frequency ruler, has revolutionized optical frequency metrology. This thesis now presents the first experimental demonstration of the phononic analogue of such frequency combs [13]. These observations came about in a micromechanical resonator device, confirming predictions made by numerical simulations of a Fermi-Pasta-Ulam system [14]. While the spectral features are similar, the physics of phononic frequency comb generation is conceivably different from that

of its optical counterpart. An off-resonant drive of a phonon mode results in frequency combs through its intrinsic coupling with the other modes of micromechanical resonator (Figure 1.5).

The possible reasons for the absence of phononic frequency combs in the past are as follows: multiple modes should be strongly coupled and the device should withstand high excitation amplitudes; easy and informative characterisation is required for the clear demonstration of physical pathway related to the generation of phononic frequency comb. While the comb regimes are qualitatively known for simple experimental cases (Figure 1.6), the future studies on the deep understanding of emergent maps of phononic frequency comb are therefore necessary for its predictive engineering.

1.4. Possible Significance of Phononic Frequency Combs

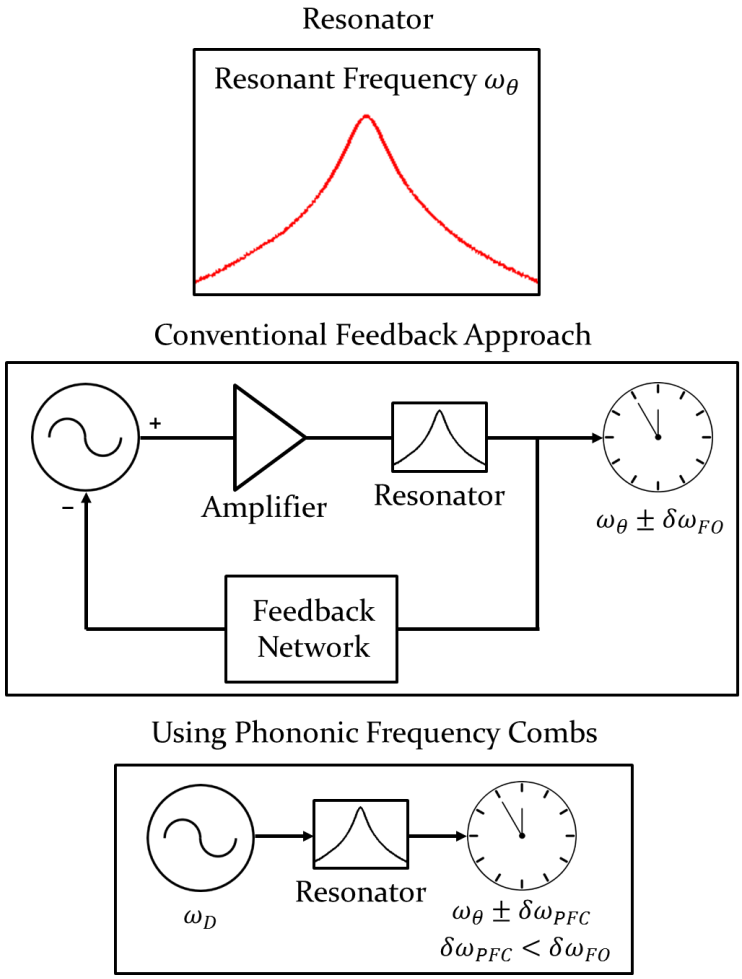

Figure 1.7: Phononic Frequency Combs based Resonant Frequency Excitation and Tracking. Comparison of the feedback oscillator vs. phononic frequency combs based oscillator.

While the optical frequency combs have revolutionized light metrology and hence, have served as 'gears' of ultra-fast optical atomic clocks [15], phononic frequency combs can possibly impact another class of precision measurements. It will be shown in this thesis that the physical pathway of phononic frequency combs is fundamental to the self-excitation of modal frequency ω_θ [13]. This unique capability can therefore present a new approach to track resonance. Such a phononic frequency combs based approach, through a much simpler topology, can provide a more precise estimate for resonant frequency ω_θ (Figure 1.7) as also suggested by the results provided in the future work section of this thesis.

1.5. Objectives and Plan of the Thesis

This thesis presents experimental observations of phononic frequency combs in micromechanical devices, and provides a conceptual basis to describe these observations. Chapter 2 presents the discussion on the established resonant pathways. In Chapter 3, a theoretical sketch of new phononic frequency combs is presented. After setting out the theoretical background, the experimental segment spans over Chapters 4-5. While the construction of experimental device is presented in Chapter 4, Chapter 5 presents multiple experimental observations of frequency combs and their links to the established theoretical framework. Finally, Chapter 6 summarizes the findings and Chapter 7 discusses future work and potential applications.

Chapter 2

Established Resonant Phenomena

This chapter recapitulates established resonant phenomena that typically arise in many physical systems, including vibratory structures. Particularly, we focus on three representative mechanisms of relevance to this thesis namely, linear resonance, Duffing phenomenon and parametric resonance.

2.1. Linear Resonance

2.1.1. Observations

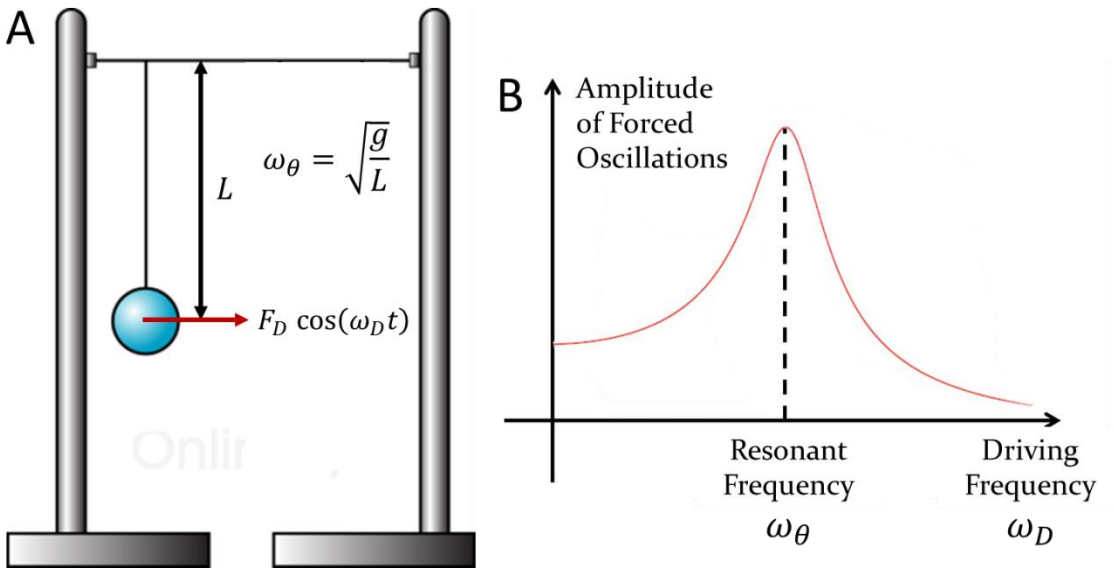

Figure 2.1: **Resonance of Pendulum (A pendulum is a mass suspended from a pivot).** A: An oscillatory force $F_D \cos(\omega_D t)$ is applied on the pendulum so that it oscillates; B: The pendulum oscillation amplitudes as a function of driving frequency ω_D.

Resonance or Linear Resonance (LR) is a phenomenon by which a physical system responds at greater amplitude when the frequency of oscillations ω_D gets closer to the system's natural frequency ω_θ (Figure 2.1).

2.1.1.1. Example of Swing

To understand this mechanism further, let us consider a familiar case of swing as shown below. If the swing is struck, the seat will move back and forth about the pivot (Figure 2.2).

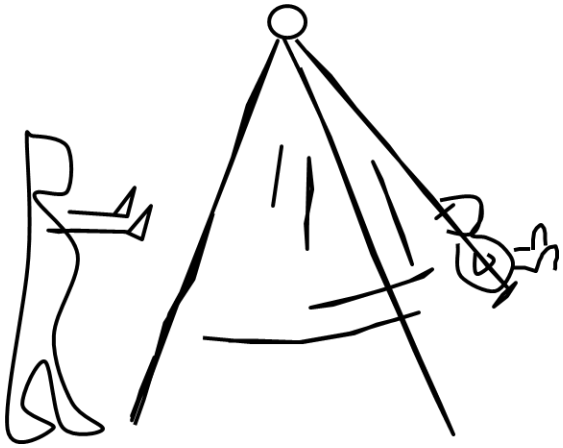

Figure 2.2: **Swing oscillations.** The swing oscillates at a specific frequency when struck.

The frequency of this oscillation depends on the length of rope (L) that connects the pivot and seat together. We term this frequency as the system's natural or resonant frequency (ω_θ). Particularly, for the swing system, ω_θ is given by

$$\omega_\theta = \sqrt{\frac{g}{L}} \tag{2.1}$$

where g is the acceleration due to gravity (about 9.8 m/s^2 near the surface of earth).

Now, instead of ping, we consider the case where the swing is periodically pushed. If the frequency of input drive (ω_D) equals ω_θ, the swing will oscillate at higher and higher amplitudes. However, when ω_D gets farther from ω_θ, the swing oscillations turn feeble. This happens because the energy absorbed by the swing is maximal for the swing's natural oscillations.

2.1.2. Theoretical Description

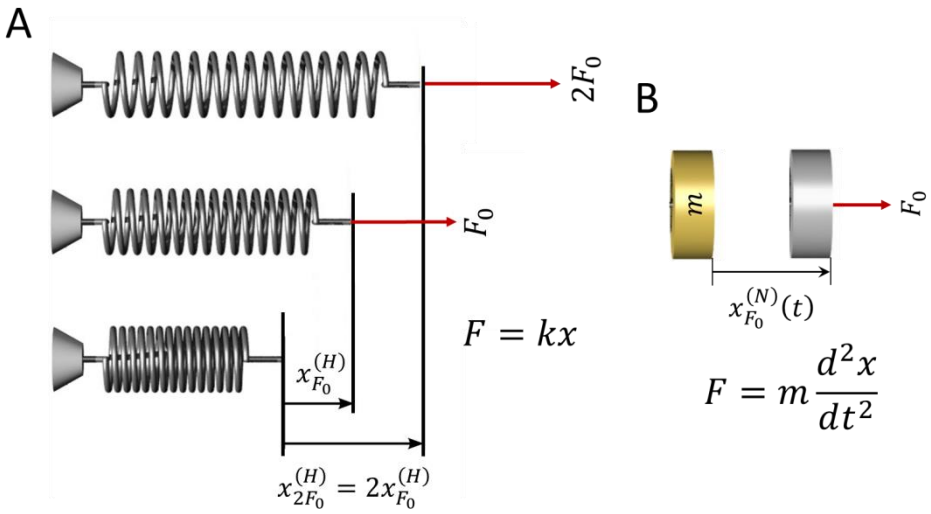

Figure 2.3: A: **Hooke's Law.** The extension of spring k is directly proportional to the net force F acting on the spring itself; B: **Newton's Second Law.** The acceleration of mass m is directly proportional to the net force acting on the mass itself.

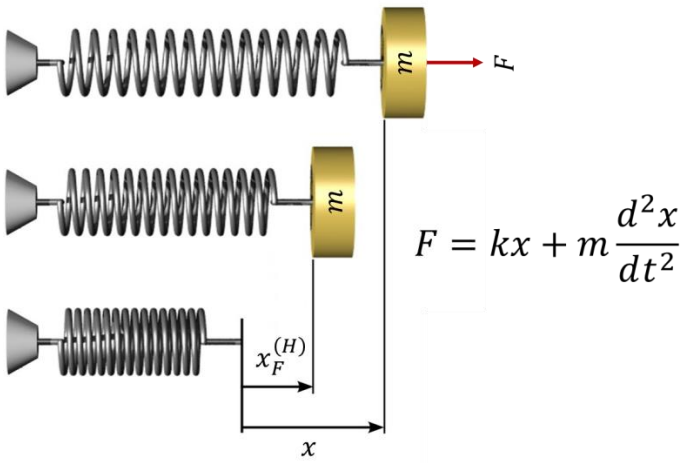

Figure 2.4: **Force Applied on a Mass-Spring System.** If force F is applied on the system consisting of mass m and spring k, then the net time-varying displacement (x) of system can be computed based on both Hooke's and Newton's laws.

The previous section has thus shown the features of LR. However, to quantitatively understand this mechanism, the equations of motion should be developed for the physical system undergoing resonance (for e.g. a swing). To this end, we begin with the fundamental

Hooke's law $F_{Hooke} = kx$ (Figure 2.3A) and Newton's second law $F_{Newton} = m\frac{\partial^2 x}{\partial t^2}$ (Figure 2.3B).

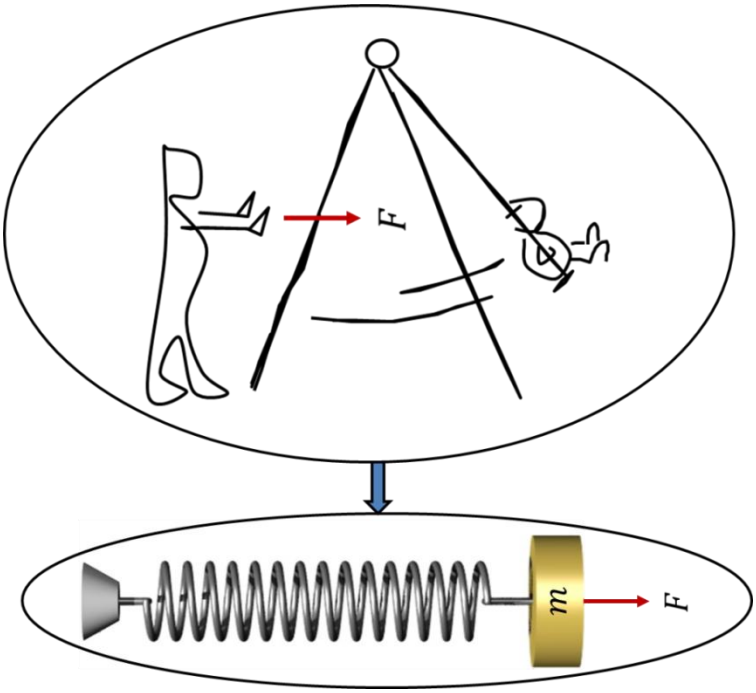

Figure 2.5: **Analogy of Mass-Spring System.** Any physical system can be represented by a coupled mass m – spring k framework. However, the virtual values of m and k are calculated based on the specific properties of physical system under consideration.

We can represent any physical system by a coupled mass m – spring k arrangement (Figure 2.5). The applied force F on such a system manifests as Hooke's force kx and Newton's force $m\frac{\partial^2 x}{\partial t^2}$ (Figure 2.4) i.e.

$$F = kx + m\frac{\partial^2 x}{\partial t^2} \tag{2.2}$$

Here, x is the time-varying displacement of mass-spring system. Now, to explore the phenomenon of LR, we consider an oscillatory force $F = F_D \cos(\omega_D t)$ i.e.

$$F_D \cos(\omega_D t) = kx + m\frac{\partial^2 x}{\partial t^2} \tag{2.3}$$

This oscillatory force is analogous to the periodic push on the swing (or a pendulum) (Section 2.1.1.1.). After time integration of equation 2.3, we now have

$$\int_0^t \int_0^t F_D \cos(\omega_D t)\ dt\ dt\ = \int_0^t \int_0^t kx\ dt\ dt\ + \int_0^t \int_0^t m\frac{\partial^2 x}{\partial t^2}\ dt\ dt$$
$$\left[-\frac{F_D \cos(\omega_D t)}{\omega_D^2} = k\int_0^t \int_0^t x\ dt\ dt + mx\right] \tag{2.4}$$

The displacement x, in response to $F_D \cos(\omega_D t)$, will also oscillate at the same frequency ω_D. Hence, we have

$$\left[-\frac{F_D \cos(\omega_D t)}{\omega_D^2} = k\int_0^t \int_0^t x\ dt\ dt + mx\right]; x = A\cos(\omega_D t)$$
$$\left[-\frac{F_D \cos(\omega_D t)}{\omega_D^2} = -\frac{Ak\cos(\omega_D t)}{\omega_D^2} + Am\cos(\omega_D t)\right] \tag{2.5}$$

By rearrangement of terms, the solution for x can be obtained as

$$x = \frac{F_D}{k - m\omega_D^2}\cos(\omega_D t) = \frac{F_D}{m\left(\frac{k}{m} - \omega_D^2\right)}\cos(\omega_D t) \tag{2.6}$$

Now, we investigate the relationship between ω_D and amplitude of oscillations $x_A = \frac{F_D}{m\left(\frac{k}{m} - \omega_D^2\right)}$.

As ω_D gets closer to $\sqrt{\frac{k}{m}}$, x_A tends to infinity.

In reality, even at resonance, the infinite oscillation amplitudes do not exist (Figures 2.1B and 2.6B). Hence, the equation 2.2 that is merely constructed by the basic Hooke's law and Newton's second law does not fully describe the experiments (Figure 2.6).

To account for this experimental variation, a correction term $\gamma\frac{\partial x}{\partial t}$ is then introduced into the original formulation (Equation 2.2) as,

$$F = kx + m\frac{\partial^2 x}{\partial t^2} + \gamma\frac{\partial x}{\partial t} \tag{2.7}$$

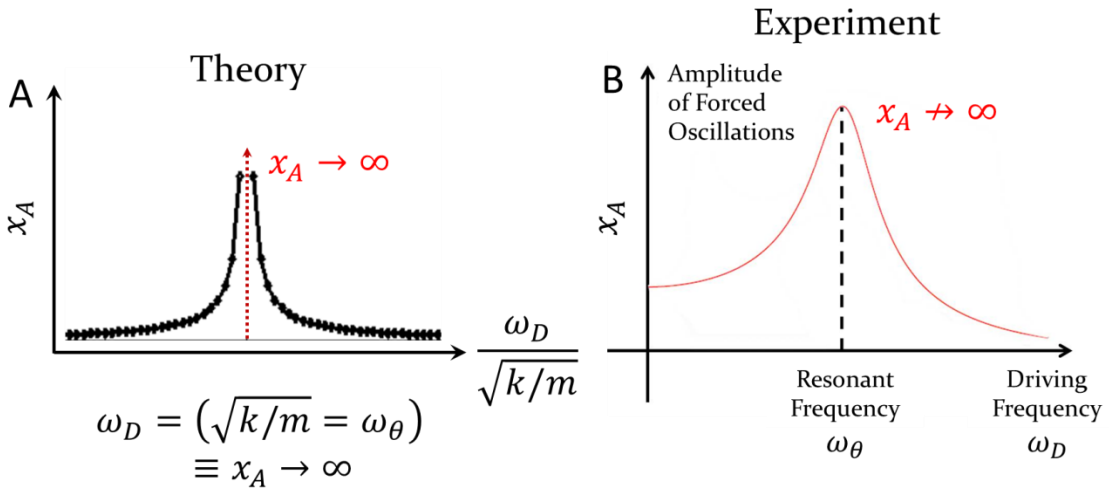

Figure 2.6: **Disagreement between Theory and Experiment.** A and B: The theoretical and experimental responses respectively.

Here again, $F = F_D \cos(\omega_D t)$ is applied and x is assumed to take the form $Ae^{j\omega_D t}$. $F_D \cos(\omega_D t)$ can also be written as $\frac{F_D e^{j\omega_D t}}{2} + \frac{F_D e^{-j\omega_D t}}{2}$. Hence, $F = kx + m\frac{\partial^2 x}{\partial t^2} + \gamma\frac{\partial x}{\partial t}$ becomes $\frac{F_D e^{j\omega_D t}}{2} + \frac{F_D e^{-j\omega_D t}}{2} = kAe^{j\omega_D t} - m\omega_D^2 Ae^{j\omega_D t} + j\gamma\omega_D Ae^{j\omega_D t}$.

By rearrangement, the solution for x can be obtained as

$$x = Ae^{j\omega_D t} = \frac{F_D}{k - m\omega_D^2 + j\gamma\omega_D}\frac{e^{j\omega_D t} + e^{-j\omega_D t}}{2}$$
$$x = \frac{F_D}{k - m\omega_D^2 + j\gamma\omega_D}\cos(\omega_D t) \qquad (2.8)$$

Hence, $x_A = \frac{F_D}{\sqrt{\left(k - m\omega_D^2\right)^2 + \gamma^2\omega_D^2}}$.

Figure 2.7 depicts frequency responses at varying levels of damping $\frac{\gamma}{m}$. As it can now be seen from Figure 2.8, the revised formalism $F = kx + m\frac{\partial^2 x}{\partial t^2} + \gamma\frac{\partial x}{\partial t}$ captures the experimental observations of LR (Figure 2.8A).

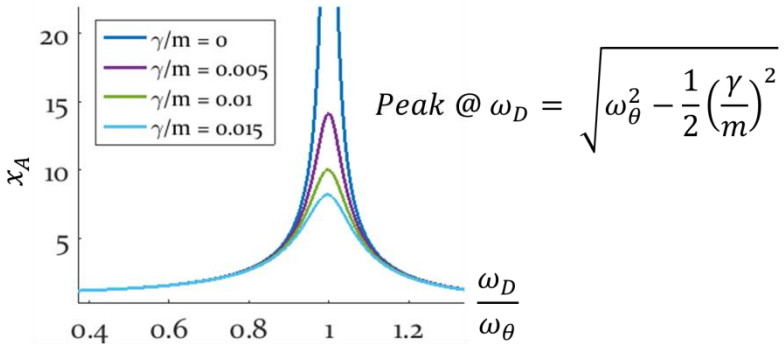

Figure 2.7: **Damped Frequency Responses.**

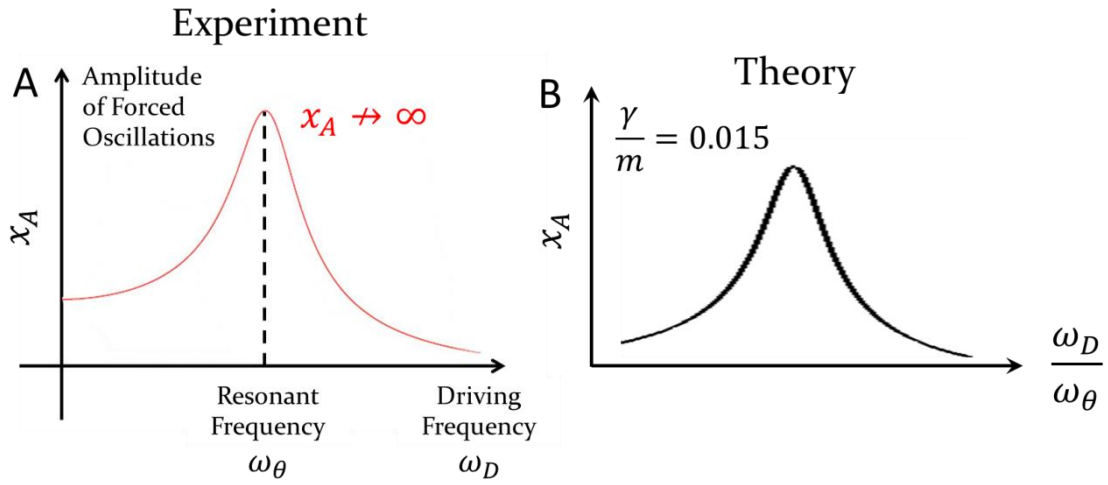

Figure 2.8: **Agreement between Theory and Experiment.** A and B: The theoretical and experimental responses associated with linear resonance respectively.

Let us now understand the physical meaning of $F = kx + m\frac{\partial^2 x}{\partial t^2} + \gamma\frac{\partial x}{\partial t}$. The driving force F gets manifested not only as spring and inertial forces but also as lossy damping force. Similar to the linear dependence with displacement x in the Hooke's law and the linear dependence with acceleration $\frac{\partial^2 x}{\partial t^2}$ in the Newton's second law, the linear dependence with velocity $\frac{\partial x}{\partial t}$ is typical of damping force.

The equation $F = kx + m\frac{\partial^2 x}{\partial t^2} + \gamma\frac{\partial x}{\partial t}$, with $F = F_D\cos(\omega_D t)$, describes resonance of a physical system abstracted by a coupled mass m - spring k model. This resonance equation can also be re-arranged as

$$
\begin{aligned}
F_D \cos(\omega_D t) &= kx + m\frac{\partial^2 x}{\partial t^2} + \gamma\frac{\partial x}{\partial t} \\
\frac{F_D}{m}\cos(\omega_D t) &= \frac{k}{m}x + \frac{\partial^2 x}{\partial t^2} + \frac{\gamma}{m}\frac{\partial x}{\partial t} \\
P_D \cos(\omega_D t) &= \frac{\partial^2 x}{\partial t^2} + 2\zeta_\theta \frac{\partial x}{\partial t} + \omega_\theta^2 x
\end{aligned}
\tag{2.9}
$$

where $\omega_\theta \left(= \sqrt{\frac{k}{m}}\right)$ and $\zeta_\theta \left(= \frac{\gamma}{2m}\right)$ are the resonant frequency and damping ratios of the physical system; P_D and ω_D are the drive level and frequency.

Hence, the mathematical description $\frac{\partial^2 x}{\partial t^2} + 2\zeta_\theta \frac{\partial x}{\partial t} + \omega_\theta^2 x = P_D \cos(\omega_D t)$ models LR of a resonant system with damping ratio ζ_θ and natural frequency ω_θ. Such resonators assume specific forms viz. mechanical or acoustic resonator [16-18], electrical resonator [19], optical resonator [20-22], orbital resonator [23] and atomic, particle, and molecular resonators [24-25].

2.2. Duffing Phenomenon

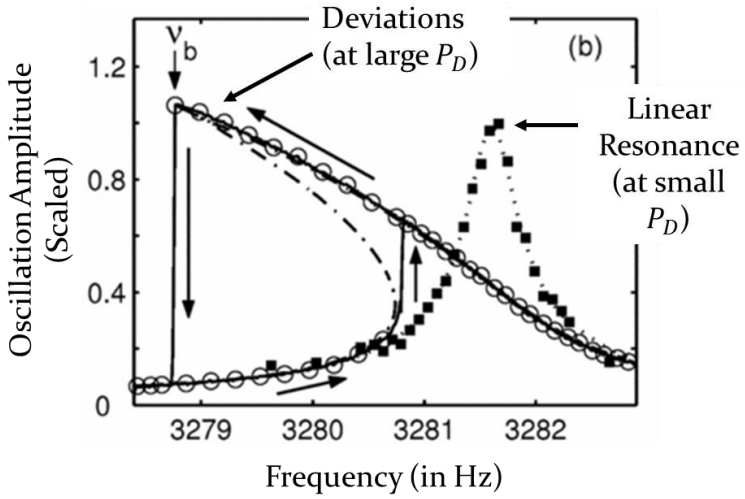

Figure 2.9: **Duffing Phenomenon.** The frequency responses get skewed at large drive levels of P_D. Reprinted figure with permission from [C. Stambaugh and H. B. Chan, *Physical Review B,* vol. 73, p. 172302, 2006.] Copyright (2006) by the American Physical Society.

While the formulation $\frac{\partial^2 x}{\partial t^2} + 2\zeta_\theta \frac{\partial x}{\partial t} + \omega_\theta^2 x = P_D \cos[(\omega_D \cong \omega_\theta)t]$ presents an excellent description for resonance at low values of P_D, the deviations from the standard resonant response are typically observed at larger P_D. The starting point to describe deviation from linear theory is often the Duffing phenomenon (DP) [26] which is presented in more detail below.

The mere original formulation $\frac{\partial^2 x}{\partial t^2} + 2\zeta_\theta \frac{\partial x}{\partial t} + \omega_\theta^2 x = P_D \cos[(\omega_D \cong \omega_\theta)t]$ however cannot explain this mechanism. To this end, an additional correction term: βx^3 is thus included to describe the first higher order nonlinear term in a system describing symmetrical nonlinear response about the rest position. This term is proportional to the cube of displacement x. While the term βx^3 is added to specifically address DP, the inclusion of terms with different powers of displacements i.e. $x^2, x^4, x^5, \ldots$ may possibly address other variants of resonant response [27].

Now, we can solve the corrected formalism

$$\frac{\partial^2 x}{\partial t^2} + 2\zeta_\theta \frac{\partial x}{\partial t} + \omega_\theta^2 x + \beta x^3 = P_D \cos[(\omega_D \cong \omega_\theta)t] \tag{2.10}$$

Let us first assume that x takes the form $\frac{1}{2}\left(Ae^{j\omega_D t} + A^* e^{-j\omega_D t}\right)$ where A is a complex number and A^* is its conjugate. By mathematical identity, $\cos(\omega_D t)$ can be written as $\frac{e^{j\omega_D t}}{2} + \frac{e^{-j\omega_D t}}{2}$. After substituting x and $\cos(\omega_D t)$ by the respective analogues, we have

$$\begin{aligned} -\frac{\omega_D^2 A}{2} e^{j\omega_D t} - \frac{\omega_D^2 A^*}{2} e^{-j\omega_D t} + j\zeta_\theta A\omega_D e^{j\omega_D t} - j\zeta_\theta A^*\omega_D e^{-j\omega_D t} + \frac{\omega_\theta^2 A}{2} e^{j\omega_D t} \\ + \frac{\omega_\theta^2 A}{2} e^{-j\omega_D t} \\ + \frac{\beta}{8}\left[A^3 e^{3j\omega_D t} + A^{*3} e^{-3j\omega_D t} + 3|A|^2 A e^{j\omega_D t} + 3|A|^2 A^* e^{-j\omega_D t}\right] \\ = \frac{P_D e^{j\omega_D t}}{2} + \frac{P_D e^{-j\omega_D t}}{2} \end{aligned} \tag{2.11}$$

In this lengthy expression 2.11, we can drop-off terms of order $e^{\pm 3j\omega_D t}$ assuming that the primary term of interest is fundamental. Now, by comparing the terms of order $e^{\pm j\omega_D t}$, we get

$$A = \frac{P_D}{\omega_\theta^2 - \omega_D^2 + \frac{3\beta}{4}|A|^2 + 2j\zeta_\theta\omega_D} \tag{2.12}$$

Hence, x is given by

$$x = A\cos(\omega_D t) = \frac{P_D}{\omega_\theta^2 - \omega_D^2 + \frac{3\beta}{4}|A|^2 + 2j\zeta_\theta\omega_D}\cos(\omega_D t) \tag{2.13}$$

Now, by solving the following equation 2.14, we can thus obtain the solutions for the displacement amplitude x_A.

$$\begin{aligned} x_A = |A| = & \frac{P_D}{\sqrt{\left(\omega_\theta^2 - \omega_D^2 + \frac{3\beta}{4}|A|^2\right)^2 + 4\zeta_\theta^2\omega_D^2}} \\ & \Rightarrow \left\{\left[\frac{9}{16}\beta^2\right]x_A^6 + \left[\frac{3}{2}\beta\left(\omega_\theta^2 - \omega_D^2\right)\right]x_A^4 + \left[\left(\omega_\theta^2 - \omega_D^2\right)^2 + 4\zeta_\theta^2\omega_D^2\right]x_A^2 - P_D^2 \right. \\ & \left. = 0\right\} \end{aligned} \tag{2.14}$$

As it can now be seen from Figure 2.10, the revised formalism $\frac{\partial^2 x}{\partial t^2} + 2\zeta_\theta\frac{\partial x}{\partial t} + \omega_\theta^2 x + \beta x^3 = P_D\cos(\omega_D t)$ can thus capture the experimental observations of DP (Figure 2.9).

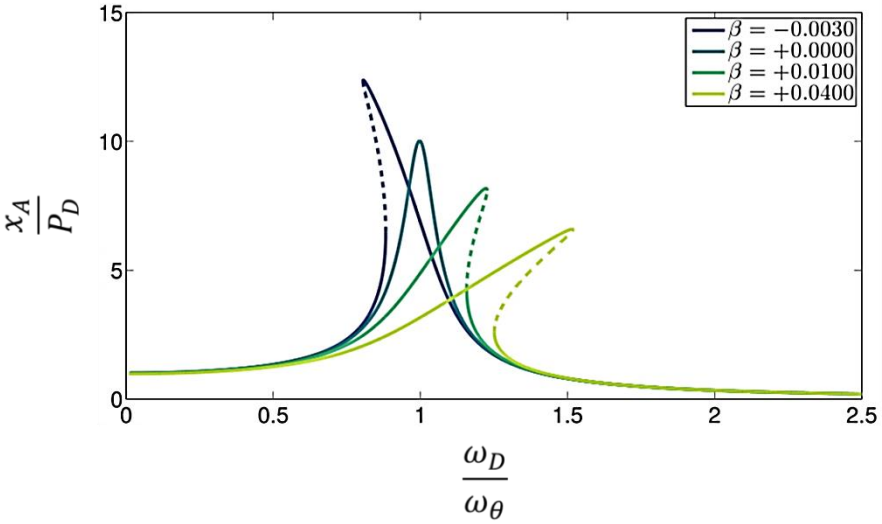

Figure 2.10: **Duffing Phenomenon.** The frequency responses for $\omega_\theta = 1; \zeta_\theta = 0.05; P_D = 1$ and varying levels of β.

Let us now turn to the physical meaning of $\frac{\partial^2 x}{\partial t^2} + 2\zeta_\theta \frac{\partial x}{\partial t} + \omega_\theta^2 x + \beta x^3 = P_D \cos(\omega_D t)$. While the fundamental Hooke's or spring force has a linear dependence with displacement x, the term βx^3 describes nonlinear spring action. Fundamentally, this term corrects the Hooke's law which ultimately leads to an interesting variation of resonant response inherent to DP.

2.3. Parametric Resonance

In Section 2.1, we had discussed the nominal case of LR. While such a phenomenon of LR can only be seen at low enough drive levels P_D, there is however an onset of DP at large magnitudes of P_D (Figure 2.9). Section 2.2 had presented a mathematical framework to explain DP (Figure 2.10). While DP represents one possible nonlinear pathway, different operative pathways may also evidence at large enough values of P_D. One such case is parametric resonance (PR) (Figure 2.11) [28]. Here, when P_D goes above a threshold value, a secondary mode y also gets excited in addition to the nominal driven mode x.

To understand this observation, we first consider two independent resonant modes x and y. The equations of motion corresponding to each mode can then be written as

$$\frac{\partial^2 x}{\partial t^2} + 2\zeta_x \frac{\partial x}{\partial t} + \omega_x^2 x = P_D \cos(\omega_D t) \tag{2.15}$$

$$\frac{\partial^2 y}{\partial t^2} + 2\zeta_y \frac{\partial y}{\partial t} + \omega_y^2 y = P_D \cos(\omega_D t) \tag{2.16}$$

Based on the analysis presented in Section 2.1, we know that the modes x and y are excited at amplitudes $\frac{P_D}{\sqrt{\left(\omega_x^2 - \omega_D^2\right)^2 + 4\zeta_x{}^2 \omega_D^2}}$ and $\frac{P_D}{\sqrt{\left(\omega_y^2 - \omega_D^2\right)^2 + 4\zeta_y{}^2 \omega_D^2}}$ respectively. However, if the drive frequency $(\omega_D \cong \omega_x) \gg \omega_y$, then the amplitude of mode y is negligibly small. Hence, only the mode x is significantly excited. Therefore, the coupled equations 2.15 and 2.16 can be approximated as,

$$\frac{\partial^2 x}{\partial t^2} + 2\zeta_x \frac{\partial x}{\partial t} + \omega_x^2 x = P_D \cos(\omega_D t) \tag{2.17}$$

$$\frac{\partial^2 y}{\partial t^2} + 2\zeta_y \frac{\partial y}{\partial t} + \omega_y^2 y = 0 \tag{2.18}$$

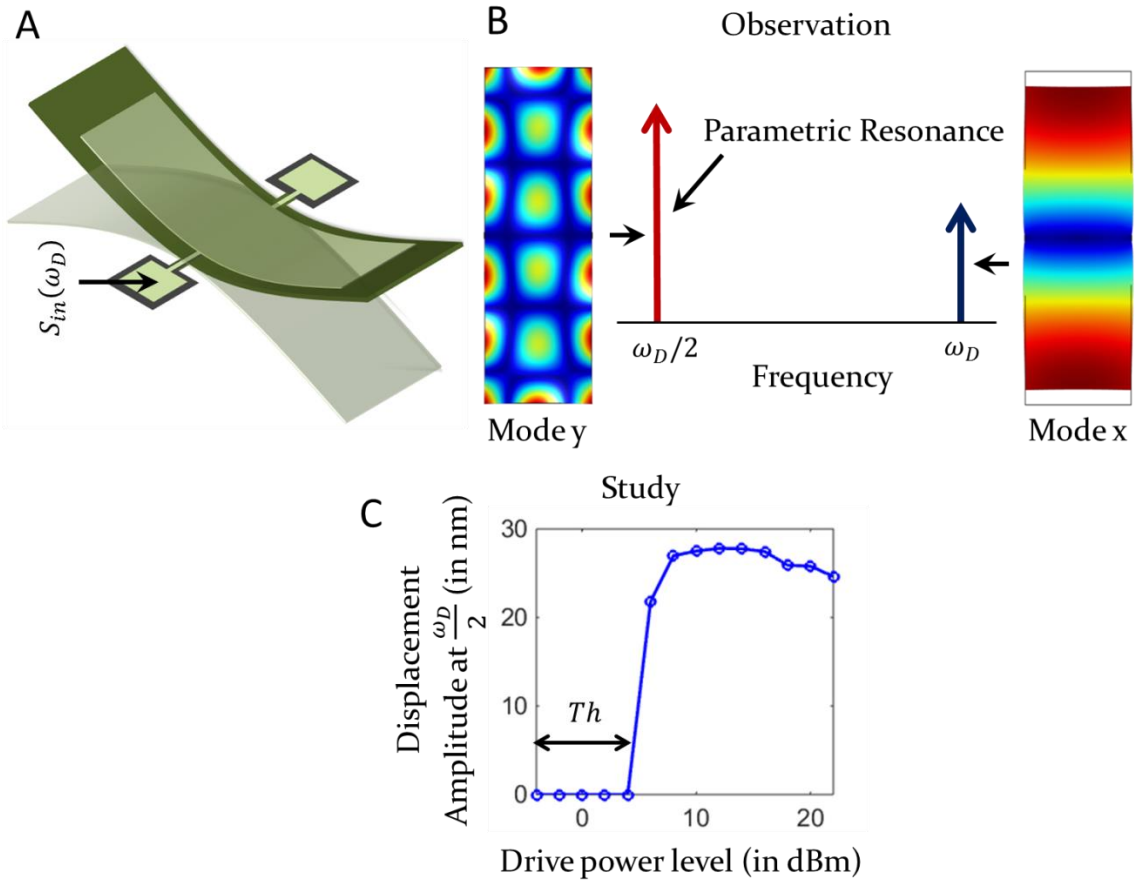

Figure 2.11: **Parametric Resonance.** A: An electrical signal $S_{in}(\omega_D)$ is injected into a micromechanical resonator; B: The corresponding output response of resonator; C: The displacement amplitude at $\frac{\omega_D}{2}$ as a function of drive power level. When the drive power level is increased above a threshold value Th, the displacement amplitude is increased from 'o' to a large value of approximately 30 nm.

Now, when x is large-enough and the condition $(\omega_D \cong \omega_x) \approx 2\omega_y$ is also satisfied, the experimental results have however indicated (including Figure 2.11) that a mode y gets excited as well. This excitation of a different mode y (which is not directly driven) through the driven mode x is referred to as PR.

However, the equations 2.17 and 2.18 in the present form cannot directly explain the peculiar observations of PR (Figure 2.11). To now formulate the dynamics for this, the nonlinear terms

$\alpha_{yy}y^2$ and $\alpha_{yx}yx$ are added in the equations 2.17 and 2.18 respectively so that the modes x and y are nonlinearly coupled. Henceforth, we have

$$\frac{\partial^2 x}{\partial t^2} + 2\zeta_x \frac{\partial x}{\partial t} + \omega_x^2 x + \alpha_{yy}y^2 = P_D \cos(\omega_D t) \tag{2.19}$$

$$\frac{\partial^2 y}{\partial t^2} + 2\zeta_y \frac{\partial y}{\partial t} + \omega_y^2 y + \alpha_{yx}yx = 0 \tag{2.20}$$

The solution of first differential equation 2.19 is assumed to yield displacement x in the form $A(t)\cos(\omega_D t)$. Now, we substitute this expression of x in the second differential equation 2.20. Henceforth, we have

$$\frac{\partial^2 y}{\partial t^2} + 2\zeta_y \frac{\partial y}{\partial t} + \omega_y^2 y + \alpha_{yx}yA(t)\cos(\omega_D t) = 0 \tag{2.21}$$

Motivated by the observations presented in Figure 2.11, we set $\omega_D = 2\omega_y + \epsilon$ (Here, ϵ is the detuning for the parametric resonance of mode y). Now, we search for the displacement y in the form

$$y = p\cos\left[\left(\omega_y + \frac{\epsilon}{2}\right)t\right] + q\sin\left[\left(\omega_y + \frac{\epsilon}{2}\right)t\right] \tag{2.22}$$

The time derivatives $\dot{y} = \frac{\partial y}{\partial t}$ and $\ddot{y} = \frac{\partial^2 y}{\partial t^2}$ will then be

$$\begin{aligned}\dot{y} = \dot{p}\cos\left[\left(\omega_y + \frac{\epsilon}{2}\right)t\right] + \dot{q}\sin\left[\left(\omega_y + \frac{\epsilon}{2}\right)t\right] - p\left(\omega_y + \frac{\epsilon}{2}\right)\sin\left[\left(\omega_y + \frac{\epsilon}{2}\right)t\right] \\ + q\left(\omega_y + \frac{\epsilon}{2}\right)\cos\left[\left(\omega_y + \frac{\epsilon}{2}\right)t\right]\end{aligned} \tag{2.23}$$

$$\begin{aligned}\ddot{y} = \ddot{p}\cos\left[\left(\omega_y + \frac{\epsilon}{2}\right)t\right] + \ddot{q}\sin\left[\left(\omega_y + \frac{\epsilon}{2}\right)t\right] - 2\dot{p}\left(\omega_y + \frac{\epsilon}{2}\right)\sin\left[\left(\omega_y + \frac{\epsilon}{2}\right)t\right] \\ + 2\dot{q}\left(\omega_y + \frac{\epsilon}{2}\right)\cos\left[\left(\omega_y + \frac{\epsilon}{2}\right)t\right] - p\left(\omega_y + \frac{\epsilon}{2}\right)^2\cos\left[\left(\omega_y + \frac{\epsilon}{2}\right)t\right] \\ - q\left(\omega_y + \frac{\epsilon}{2}\right)^2\sin\left[\left(\omega_y + \frac{\epsilon}{2}\right)t\right]\end{aligned} \tag{2.24}$$

We can further assume that the functions p and q are slow-varying. Hence, $\ddot{p}$ and $\ddot{q}$ can be set to zero.

$$\dot{y} = \dot{p}\cos\left[\left(\omega_y + \frac{\epsilon}{2}\right)t\right] + \dot{q}\sin\left[\left(\omega_y + \frac{\epsilon}{2}\right)t\right] - p\left(\omega_y + \frac{\epsilon}{2}\right)\sin\left[\left(\omega_y + \frac{\epsilon}{2}\right)t\right] + q\left(\omega_y + \frac{\epsilon}{2}\right)\cos\left[\left(\omega_y + \frac{\epsilon}{2}\right)t\right] \tag{2.25}$$

$$\ddot{y} \cong -2\dot{p}\left(\omega_y + \frac{\epsilon}{2}\right)\sin\left[\left(\omega_y + \frac{\epsilon}{2}\right)t\right] + 2\dot{q}\left(\omega_y + \frac{\epsilon}{2}\right)\cos\left[\left(\omega_y + \frac{\epsilon}{2}\right)t\right] - p\left(\omega_y + \frac{\epsilon}{2}\right)^2\cos\left[\left(\omega_y + \frac{\epsilon}{2}\right)t\right] - q\left(\omega_y + \frac{\epsilon}{2}\right)^2\sin\left[\left(\omega_y + \frac{\epsilon}{2}\right)t\right] \tag{2.26}$$

Also, for small ϵ, $\left(\omega_y + \frac{\epsilon}{2}\right)^2 \cong \omega_y^2 + \omega_y\epsilon$ and $\omega_y + \frac{\epsilon}{2} \cong \omega_y$. Hence, we get

$$\dot{y} = \dot{p}\cos\left[\left(\omega_y + \frac{\epsilon}{2}\right)t\right] + \dot{q}\sin\left[\left(\omega_y + \frac{\epsilon}{2}\right)t\right] - p\omega_y\sin\left[\left(\omega_y + \frac{\epsilon}{2}\right)t\right] + q\omega_y\cos\left[\left(\omega_y + \frac{\epsilon}{2}\right)t\right] \tag{2.27}$$

$$\ddot{y} \cong -\omega_y^2 y - \omega_y\epsilon y - 2\dot{p}\omega_y\sin\left[\left(\omega_y + \frac{\epsilon}{2}\right)t\right] + 2\dot{q}\omega_y\cos\left[\left(\omega_y + \frac{\epsilon}{2}\right)t\right] \tag{2.28}$$

Let us now turn to the equation 2.21.

$$\begin{gathered}\left[\ddot{y} + 2\zeta_y\dot{y} + \omega_y^2 y + \alpha_{yx}yA(t)\cos(\omega_D t) = 0\right] \\ \Rightarrow \left[\ddot{y} + 2\zeta_y\dot{y} + \omega_y^2 y + \left(\alpha_{yx}A\right)y\cos\left[\left(2\omega_y + \epsilon\right)t\right] = 0\right]\end{gathered} \tag{2.29}$$

Also, the term $\left(\alpha_{yx}A\right)y\cos\left[\left(2\omega_y + \epsilon\right)t\right]$ can be re-arranged as

$$\begin{gathered}\left(\alpha_{yx}A\right)y\cos\left[\left(2\omega_y + \epsilon\right)t\right] \\ \Rightarrow \left\{\left(\alpha_{yx}A\right)\left[p\cos\left[\left(\omega_y + \frac{\epsilon}{2}\right)t\right] + q\sin\left[\left(\omega_y + \frac{\epsilon}{2}\right)t\right]\right]\cos\left[\left(2\omega_y + \epsilon\right)t\right]\right\} \\ \Rightarrow \left\{\left(\alpha_{yx}A\right)\left[p\left[\frac{1}{2}\cos\left[\left(\omega_y + \frac{\epsilon}{2}\right)t\right] + \frac{1}{2}\cos\left[3\left(\omega_y + \frac{\epsilon}{2}\right)t\right]\right] + q\left[-\frac{1}{2}\sin\left[\left(\omega_y + \frac{\epsilon}{2}\right)t\right] + \frac{1}{2}\sin\left[3\left(\omega_y + \frac{\epsilon}{2}\right)t\right]\right]\right]\right\}\end{gathered} \tag{2.30}$$

Here, we can drop-off terms with functions $\cos\left[3\left(\omega_y + \frac{\epsilon}{2}\right)t\right]$ and $\sin\left[3\left(\omega_y + \frac{\epsilon}{2}\right)t\right]$ as these will be damped out. Hence,

$$\left(\alpha_{yx}A\right)y\cos\left[\left(2\omega_y + \epsilon\right)t\right] \cong \left[\left(\alpha_{yx}A\right)\left[\frac{p}{2}\cos\left[\left(\omega_y + \frac{\epsilon}{2}\right)t\right] - \frac{q}{2}\sin\left[\left(\omega_y + \frac{\epsilon}{2}\right)t\right]\right]\right] \tag{2.31}$$

Now, we substitute the expressions of $\ddot{y}$ (Equation 2.28), $\dot{y}$ (Equation 2.27), y (Equation 2.22) and $(\alpha_{yx}A)\, y\cos[(2\omega_y+\epsilon)t]$ (Equation 2.31) in equation 2.22. Hence, we get

$$\begin{aligned}
&[\ddot{y}+2\zeta_y\dot{y}+\omega_y^2 y+(\alpha_{yx}A)\, y\cos[(2\omega_y+\epsilon)t]=0]\Rightarrow\\
&\Big\{-\omega_y\epsilon\Big[p\cos\Big[\Big(\omega_y+\frac{\epsilon}{2}\Big)t\Big]+q\sin\Big[\Big(\omega_y+\frac{\epsilon}{2}\Big)t\Big]\Big]-2\dot{p}\omega_y\sin\Big[\Big(\omega_y+\frac{\epsilon}{2}\Big)t\Big]\\
&\quad+2\dot{q}\omega_y\cos\Big[\Big(\omega_y+\frac{\epsilon}{2}\Big)t\Big]+2\zeta_y\dot{p}\cos\Big[\Big(\omega_y+\frac{\epsilon}{2}\Big)t\Big]+2\zeta_y\dot{q}\sin\Big[\Big(\omega_y+\frac{\epsilon}{2}\Big)t\Big]\\
&\quad-2\zeta_y p\omega_y\sin\Big[\Big(\omega_y+\frac{\epsilon}{2}\Big)t\Big]+2\zeta_y q\omega_y\cos\Big[\Big(\omega_y+\frac{\epsilon}{2}\Big)t\Big]\\
&\quad+(\alpha_{yx}A)\,\Big[\frac{p}{2}\cos\Big[\Big(\omega_y+\frac{\epsilon}{2}\Big)t\Big]-\frac{q}{2}\sin\Big[\Big(\omega_y+\frac{\epsilon}{2}\Big)t\Big]\Big]=0\Big\}
\end{aligned}\tag{2.32}$$

Now, we group all of the cos and sin functions together.

$$\begin{aligned}
&\Big[-\omega_y\epsilon p+2\dot{q}\omega_y+2\zeta_y\dot{p}+2\zeta_y q\omega_y+\frac{\alpha_{yx}A}{2}p\Big]\cos\Big[\Big(\omega_y+\frac{\epsilon}{2}\Big)t\Big]\\
&\quad+\Big[-\omega_y\epsilon q-2\dot{p}\omega_y+2\zeta_y\dot{q}-2\zeta_y p\omega_y-\frac{\alpha_{yx}A}{2}q\Big]\sin\Big[\Big(\omega_y+\frac{\epsilon}{2}\Big)t\Big]=0
\end{aligned}\tag{2.33}$$

Now, the equation 2.33 is only fulfilled if the coefficients of cos and sin functions are zero. Hence,

$$-\omega_y\epsilon p+2\omega_y\dot{q}+2\zeta_y\dot{p}+2\zeta_y\omega_y q+\frac{\alpha_{yx}A}{2}p=0 \tag{2.34}$$

$$-\omega_y\epsilon q-2\omega_y\dot{p}+2\zeta_y\dot{q}-2\zeta_y\omega_y p-\frac{\alpha_{yx}A}{2}q=0 \tag{2.35}$$

We now search for the solution of this system of equations in the form

$$p=p_0e^{\mu t};\ q=q_0e^{\mu t} \tag{2.36}$$

After substituting these into the equations 2.34 and 2.35, we get

$$-\omega_y\epsilon p_0+2\omega_y\mu q_0+2\zeta_y\mu p_0+2\zeta_y\omega_y q_0+\frac{\alpha_{yx}A}{2}p_0=0 \tag{2.37}$$

$$-\omega_y\epsilon q_0-2\omega_y\mu p_0+2\zeta_y\mu q_0-2\zeta_y\omega_y p_0-\frac{\alpha_{yx}A}{2}q_0=0 \tag{2.38}$$

Let us now group the terms as

$$\left[2\omega_y\mu + 2\zeta_y\omega_y\right]q_0 + \left[\frac{\alpha_{yx}A}{2} - \omega_y\epsilon + 2\zeta_y\mu\right]p_0 = 0 \tag{2.39}$$

$$\left[\frac{\alpha_{yx}A}{2} + \omega_y\epsilon - 2\zeta_y\mu\right]q_0 + \left[2\omega_y\mu + 2\zeta_y\omega_y\right]p_0 = 0 \tag{2.40}$$

Now, we can solve these simultaneous equations as

$$\begin{vmatrix} 2\omega_y\mu + 2\zeta_y\omega_y & \frac{\alpha_{yx}A}{2} - \omega_y\epsilon + 2\zeta_y\mu \\ \frac{\alpha_{yx}A}{2} + \omega_y\epsilon - 2\zeta_y\mu & 2\omega_y\mu + 2\zeta_y\omega_y \end{vmatrix} = 0$$

$$\Rightarrow \left[\left(2\omega_y\mu + 2\zeta_y\omega_y\right)^2 - \left(\frac{\alpha_{yx}A}{2} - \left(\omega_y\epsilon - 2\zeta_y\mu\right)\right)\left(\frac{\alpha_{yx}A}{2} + \left(\omega_y\epsilon - 2\zeta_y\mu\right)\right) = 0\right]$$

$$\Rightarrow \left[\left(2\omega_y\mu + 2\zeta_y\omega_y\right)^2 - \left(\left(\frac{\alpha_{yx}A}{2}\right)^2 - \left(\omega_y\epsilon - 2\zeta_y\mu\right)^2\right) = 0\right] \tag{2.41}$$

$$\Rightarrow \left[\left(4\omega_y^2\mu^2 + 4\zeta_y^2\omega_y^2 + 8\omega_y^2\zeta_y\mu\right) - \left(\frac{\alpha_{yx}^2A^2}{4} - \left(\omega_y^2\epsilon^2 + 4\zeta_y^2\mu^2 - 4\omega_y\epsilon\zeta_y\mu\right)\right) = 0\right]$$

$$\Rightarrow \left[\left(4\omega_y^2 + 4\zeta_y^2\right)\mu^2 + \left(8\omega_y^2\zeta_y - 4\omega_y\epsilon\zeta_y\right)\mu + \left(4\zeta_y^2\omega_y^2 + \omega_y^2\epsilon^2 - \frac{\alpha_{yx}^2A^2}{4}\right) = 0\right]$$

Now, after solving the quadratic on μ, we get

$$\mu = \frac{-\left(2\omega_y^2\zeta_y - \omega_y\epsilon\zeta_y\right) \pm \sqrt{\left(2\omega_y^2\zeta_y - \omega_y\epsilon\zeta_y\right)^2 - \left(\omega_y^2 + \zeta_y^2\right)\left(4\zeta_y^2\omega_y^2 + \omega_y^2\epsilon^2 - \frac{\alpha_{yx}^2A^2}{4}\right)}}{2\omega_y^2 + 2\zeta_y^2} \tag{2.42}$$

Here, for small damping and ϵ, $\omega_y^2 \gg \zeta_y^2$, $2\zeta_y \gg \epsilon\zeta_y$. Hence,

$$\mu = \frac{-2\omega_y^2\zeta_y \pm \sqrt{\left(2\omega_y^2\zeta_y\right)^2 - \left(4\zeta_y^2\omega_y^4 + \omega_y^4\epsilon^2 - \frac{\omega_y^2\alpha_{yx}^2A^2}{4}\right)}}{2\omega_y^2}$$

$$\mu = \frac{-2\omega_y^2\zeta_y \pm \sqrt{-\left(\omega_y^4\epsilon^2 - \frac{\omega_y^2\alpha_{yx}^2A^2}{4}\right)}}{2\omega_y^2} \tag{2.43}$$

$$\mu = -\zeta_y \pm \frac{1}{2}\sqrt{\frac{\alpha_{yx}^2 A^2}{4\omega_y^2} - \epsilon^2}$$

Thus, y can be computed as

$$\begin{aligned} y &= p_0 e^{\left(-\zeta_y \pm \frac{1}{2}\sqrt{\frac{\alpha_{yx}^2 A^2}{4\omega_y^2} - \epsilon^2}\right)t} \cos\left[\left(\omega_y + \frac{\epsilon}{2}\right)t\right] + q_0 e^{\left(-\zeta_y \pm \frac{1}{2}\sqrt{\frac{\alpha_{yx}^2 A^2}{4\omega_y^2} - \epsilon^2}\right)t} \sin\left[\left(\omega_y + \frac{\epsilon}{2}\right)t\right] \\ y &= p_0 e^{\left(-\zeta_y \pm \frac{1}{2}\sqrt{\frac{\alpha_{yx}^2 A^2}{4\omega_y^2} - \epsilon^2}\right)t} \cos\left(\frac{\omega_D}{2}t\right) + q_0 e^{\left(-\zeta_y \pm \frac{1}{2}\sqrt{\frac{\alpha_{yx}^2 A^2}{4\omega_y^2} - \epsilon^2}\right)t} \sin\left(\frac{\omega_D}{2}t\right) \end{aligned} \tag{2.44}$$

For the displacement y to build up, the exponential growth factor μ can only be positive. In other words, only the positive real values of μ results in the excitation of mode y. Hence, the condition for PR can be extracted as

$$\begin{aligned} &\left[\mu = -\zeta_y \pm \frac{1}{2}\sqrt{\frac{\alpha_{yx}^2 A^2}{4\omega_y^2} - \epsilon^2}\right] > 0 \\ &(x_A = |A|) > \frac{2\omega_y}{\alpha_{yx}}\left|\sqrt{4\zeta_y^2 + \epsilon^2}\right| \end{aligned} \tag{2.45}$$

This expression thus defines the threshold for PR. Such a threshold effect corresponding to PR was also captured in Figure 2.11C. The PR of mode y with frequency $\omega_y \cong \frac{\omega_D}{2}$ occurs only if x_A of mode x with frequency $\omega_x \cong \omega_D$ is set above a characteristic value which is determined by ϵ, ζ_y and α_{yx}. Particularly, for smaller PR thresholds, the detuning levels ϵ and damping ratio ζ_y should be kept smaller and the modal coupling coefficients α_{yx} should be larger.

2.4. Summary

This chapter has hence presented three characteristic resonant phenomena viz. LR, DP and PR.

Chapter 3

Fermi-Pasta-Ulam Chains and Phononic Frequency Combs

In Chapter 2, we had discussed multiple interesting resonant phenomena including LR, DP and PR. While these discussions present an understanding of their independent implications, a collective viewpoint connecting these discrete cases was however absent in Chapter 2. And, such broad vision of resonance phenomena is equally important to establish wide experimental analogies. To this end, in this chapter, we introduce the Fermi-Pasta-Ulam (FPU) problem [29] to start with. We then present the existence of previously considered mechanisms viz. LR, DP and PR. In this manner, we establish the relevance of FPU to even the traditional cases of resonance. Following this discussion, utilizing the very same FPU framework, we show the emergence of a completely new class of nonlinear phenomena which results in phononic frequency combs (PFC).

3.1. Fermi-Pasta-Ulam Problem

The formulation of FPU problem was originally developed by the scientists Enrico Fermi, John Pasta, Stanislaw Ulam and Mary Tsingou in 1954–1955 to examine the mechanism by which a crystal advances towards thermal equilibrium [29]. For this study, they took a virtual chain of particles of mass m that are coupled by springs of constant k (Figure 3.1).

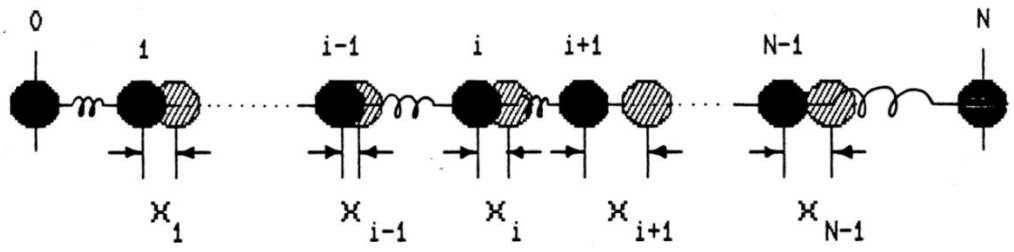

Figure 3.1: **Fermi-Pasta-Ulam Chain.**

The equations of motion for such springs can be written as

$$\begin{aligned}&[m\ddot{x}_n + k[(x_{n+1} - x_n) - (x_n - x_{n-1})] = 0]\\ &\Rightarrow [m\ddot{x}_n + k[x_{n+1} - 2x_n + x_{n-1}] = 0]\end{aligned} \tag{3.1}$$

Here, x_n denotes the displacement of n^{th} particle from its original position.

This model of a coupled system does not change the energy distribution between normal modes from a pre-defined initial condition in contravention with the equipartition theorem. To address this discrepancy, the researchers made the springs nonlinear such that the quadratic and cubic interaction terms are also included.

$$\begin{aligned}m\ddot{x}_n + k[x_{n+1} - 2x_n + x_{n-1}] + \alpha_{FPU}[(x_{n+1} - x_n)^2 - (x_n - x_{n-1})^2]\\ + \beta_{FPU}[(x_{n+1} - x_n)^3 - (x_n - x_{n-1})^3] = 0\end{aligned} \tag{3.2}$$

Here, α_{FPU} and β_{FPU} represent the strengths of quadratic and cubic interactions between particles.

In the normal mode representation, the equations of motion of a N-site FPU chain takes the form

$$\ddot{Q}_q + \omega_q^2 Q_q + \alpha_{FPU} \sum_{i,j=1}^{N} A_{q,i,j} Q_i Q_j + \beta_{FPU} \sum_{i,j,k=1}^{N} B_{q,i,j,k} Q_i Q_j Q_k = 0; q = 1,2, \dots, N \tag{3.3}$$

Here, Q_q is the displacement of mode q, $\omega_q = 2 \sin\left[\frac{\pi q}{2N}\right]$ are the normal mode frequencies and $A_{q,i,j}$ & $B_{q,i,j,k}$ are the coupling coefficients.

The initial thinking was that the nonlinearities $\alpha_{FPU} \sum_{i,j=1}^{N} A_{q,i,j} Q_i Q_j$ and $\beta_{FPU} \sum_{i,j,k=1}^{N} B_{q,i,j,k} Q_i Q_j Q_k$ would lead to energy leaking from a specific mode to the other modes until full thermalization is reached and hence, the equipartition theorem could be satisfied. However, their numerical results indicated that the energy was only shared by a few normal modes instead of all. Furthermore, after a long time, the initial state gets completely recovered. Hence, it turned out that the nonlinearity by itself is not sufficient to guarantee

equipartition of energy. While these initial numerical results of FPU did not reveal the signatures of equipartition, a recent theoretical work, supported by extensive numerical results [30], has now predicted the long thermalization timescales for the FPU chains.

3.2. Generalizing Nonlinear Phenomena

FPU chains have been used as a theoretical framework to interpret many nonlinear phenomena [14, 31-40]. For instance, one may numerically integrate FPU chains and may henceforth theorize the description and operational regimes for a new FPU phenomenon [41-42] for instance, PFC [14]. Those theories may then be adapted by the experimentalists to interpret their observations.

3.3. Linear Resonance, Duffing Phenomenon and Parametric Resonance in Fermi-Pasta-Ulam Chain

Before delving into the numerical results of PFC, we present the relevance of FPU chains to the well-established LR, DP and PR. To this end, we first consider the equations of motion.

$$\ddot{Q}_q + \omega_q^2 Q_q + \alpha_{FPU} \sum_{i,j=1}^{N} A_{q,i,j} Q_i Q_j + \beta_{FPU} \sum_{i,j,k=1}^{N} B_{q,i,j,k} Q_i Q_j Q_k = 0 \; ; q = 1,2, \dots, N \tag{3.4}$$

In this equation 3.4, the terms $2\zeta_q \dot{Q}_q$ and drive $P_D \cos(\omega_D t)$ are also included.

$$\ddot{Q}_q + \omega_q^2 Q_q + 2\zeta_q \dot{Q}_q + \alpha_{FPU} \sum_{i,j=1}^{N} A_{q,i,j} Q_i Q_j + \beta_{FPU} \sum_{i,j,k=1}^{N} B_{q,i,j,k} Q_i Q_j Q_k = P_D \cos(\omega_D t); q = 1,2, \dots, N \tag{3.5}$$

We term this revised equation 3.5 as driven-damped FPU chain. Let us consider specific cases of this condensed dynamics.

Case 1: $\alpha_{FPU} = \beta_{FPU} = 0$

$$\ddot{Q}_q + \omega_q^2 Q_q + 2\zeta_q \dot{Q}_q = P_D \cos(\omega_D t); q = 1,2, \dots, N \tag{3.6}$$

This reduced dynamics is now similar to the equation 2.9. As derived in Section 2.1, the equation 3.6 will lead to the following solutions of Q_q which model the behaviour of LR.

$$Q_q = \frac{P_0}{\omega_q^2 - \omega_D^2 + 2j\zeta_q\omega_D}\cos(\omega_D t) \tag{3.7}$$

Case 2: $\alpha_{FPU} = 0$ & $\beta_{FPU}\sum_{i,j,k=1}^{N} B_{q,i,j,k}Q_iQ_jQ_k = \beta_{qqqq}Q_q^3$

$$\ddot{Q}_q + \omega_q^2 Q_q + 2\zeta_q\dot{Q}_q + \beta_{qqqq}Q_q^3 = P_D\cos(\omega_D t); q = 1,2,\dots,N \tag{3.8}$$

This now corresponds to the 'Duffing oscillator' (Equation 2.10). Again, as derived in Section 2.2, the solutions for Q_q can be obtained as

$$Q_q = \frac{P_D}{\omega_q^2 - \omega_D^2 + \frac{3\beta_{qqqq}}{4}\varphi^2 + 2j\zeta_q\omega_D}\cos(\omega_D t) \tag{3.9}$$

where φ corresponds to the solution of cubic equation: $\left[\frac{9}{16}{\beta_{qqqq}}^2\right]\varphi^6 + \left[\frac{3}{2}\beta_{qqqq}\left(\omega_q^2 - \omega_D^2\right)\right]\varphi^4 + \left[\left(\omega_q^2 - \omega_D^2\right)^2 + 4\zeta_q^2\omega_D^2\right]\varphi^2 - P_D^2 = 0$.

Case 3: Parametric Resonance

$$\ddot{Q}_1 + \omega_1^2 Q_1 + 2\zeta_1\dot{Q}_1 + \alpha_{122}Q_2^2 = P_D\cos(\omega_D t) \tag{3.10}$$

$$\ddot{Q}_2 + \omega_2^2 Q_2 + 2\zeta_2\dot{Q}_2 + \alpha_{221}Q_1Q_2 = P_D\cos(\omega_D t) \tag{3.11}$$

The equations 3.10 and 3.11 will collectively lead to (Section 2.3)

$$\begin{aligned} Q_1 &= A\cos(\omega_D t) \\ Q_2 &= B_1\cos\left(\frac{\omega_D}{2}t\right) + B_2\sin\left(\frac{\omega_D}{2}t\right) \end{aligned} \tag{3.12}$$

where $A = \frac{P_D}{\omega_1^2 - \omega_D^2 + 2j\zeta_1\omega_D}$ and B_1 & B_2 correspond to the amplitudes associated with the in-phase and quadrature components of oscillations with frequency $\frac{\omega_D}{2}$ (Equation 2.44).

Hence, the unified FPU framework can address LR, DP and PR.

3.4. Emergence of Phononic Frequency Combs

While we had shown the existence of three well-established resonances in the previous section, the FPU chains can also emanate a wide variety of rich physical phenomena [14, 31-42]. Here, in this section, we present the theoretical discovery of one such nonlinear phenomenon: PFC.

3.4.1. Numerical Observation of Frequency Combs

To observe PFC, a 10-site FPU-α chain (Equation 3.13) was numerically simulated [14].

$$\ddot{Q}_q + \omega_q^2 Q_q + 2\zeta_q \dot{Q}_q = -\alpha_{FPU} \sum_{i,j=1}^{10} A_{q,i,j} Q_i Q_j + P_D \cos(\omega_D t); q = 1,2,\dots,N \tag{3.13}$$

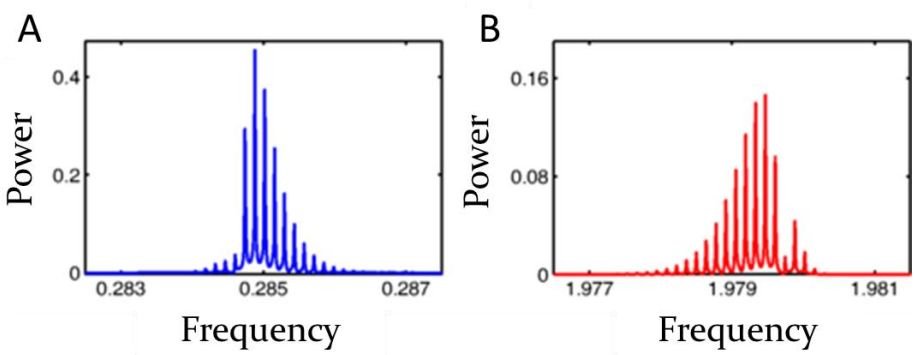

Figure 3.2: **Spectral Signature of Frequency Combs.** A-B: The frequency spectra corresponding to phonon modes Q_1 and Q_{10} respectively. Here, $(P_D, \alpha_{FPU}, \omega_D) = (0.1,0.1,2.264)$. Reprinted figure with permission from [L. S. Cao, D. X. Qi, R. W. Peng, M. Wang, and P. Schmelcher, *Physical review letters,* vol. 112, p. 075505, 2014.] Copyright (2014) by the American Physical Society.

The reported numerical simulations are based on the complete dynamics (Equation 3.13) without any truncation [14]. The drive $P_D \cos(\omega_D t)$ was suitably adjusted to a specific set of values to let the modes: Q_1 and Q_{10} in nonlinear resonance. Further, to avoid significant linear

excitation of other phonon modes $Q_{2,\ldots,9}$, ω_D was also spaced farther away from their resonant frequencies $\omega_{2,\ldots,9}$. Now, to quantify the response, the oscillations of effective phonon number N_{eff} corresponding to all phonon modes $Q_{1,\ldots,10}$ were examined.

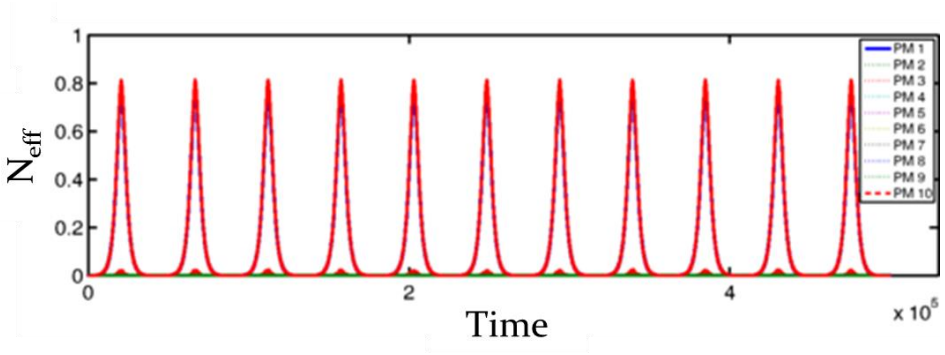

Figure 3.3: **Temporal Signature of Frequency Combs.** The N_{eff} oscillations corresponding to all phonon modes $Q_{1,\ldots,10}$. Here, $(P_D, \alpha_{FPU}, \omega_D) = (0.1, 0.1, 2.264)$. Reprinted figure with permission from [L. S. Cao, D. X. Qi, R. W. Peng, M. Wang, and P. Schmelcher, *Physical review letters,* vol. 112, p. 075505, 2014.] Copyright (2014) by the American Physical Society.

The spectral fingerprints of N_{eff} oscillations indicate that the observed nonlinear resonance relates to the emergence of an array of frequencies which are precisely separated by $\Delta\omega$ and such combs of frequencies were formed near the resonant frequency of modes Q_1 and Q_{10} i.e. 0.285 and 1.979 respectively (Figure 3.2). Furthermore, as shown in Figure 3.3, the temporal evolution of these frequency combs gets manifested as a train of pulses with period $T = \frac{2\pi}{\Delta\omega}$. This thus, as demonstrated in Figure 1.2, proves the phase coherent nature of PFC.

The numerical simulations have thus proved the existence of PFC in a 10-site FPU chain. Now, for further exploration of the PFC process, the simulations were also carried out under different drive conditions (ω_D, P). Figures 3.4A and 3.4B show the evolution of frequency combs with varying ω_D and P. Since the dynamical characteristics of combs near $\omega = 0.285$ & 1.979 are identical, only the combs near $\omega = 0.285$ were analysed. When ω_D is reduced below the frequency threshold 2.65, the tones at $\tilde{\omega}_1$ and $\omega_D - \tilde{\omega}_{10}$ get excited. By decreasing ω_D further, the number of lines associated with the frequency combs gets increased. This indicates that the strength of nonlinear resonance is greater for those low values of ω_D. In addition to the increase in the number of spectral lines, all the frequencies in

the comb including $\tilde{\omega}_1$ get varied with ω_D. This ω_D dependence of PFC results from the nonlinear foldover effect which can qualitatively be modelled by the following equation [14].

$$\tilde{\omega}_{1(10)}^2 - \omega_{1(10)}^2 = -\frac{F_k \tilde{\omega}_{10(1)}^2}{2\omega_{10(1)}^2 \left[\tilde{\omega}_{10(1)}^2 - \left(\omega_D - \tilde{\omega}_{1(10)}\right)^2\right]} \tag{3.14}$$

Here, $\omega_{1(10)}$ and $\tilde{\omega}_{1(10)}$ are the nominal and amplitude dependent resonant frequencies of normal modes 1(10) respectively; $F_k (\propto P_D)$ is the amplitude of a third mode k which mediates the interactions between modes 1 and 2 [14]. This expression indicates that $\tilde{\omega}_{1(10)}$ gets farther away from $\omega_{1(10)}$ as ω_D approaches $\tilde{\omega}_1 + \tilde{\omega}_{10}$. To independently validate this renormalization effect, the dependence with P_D can also be examined. Figure 3.4B clearly indicates the direct dependence of frequency comb spacing with P and the equation 3.14 also captures such a trend.

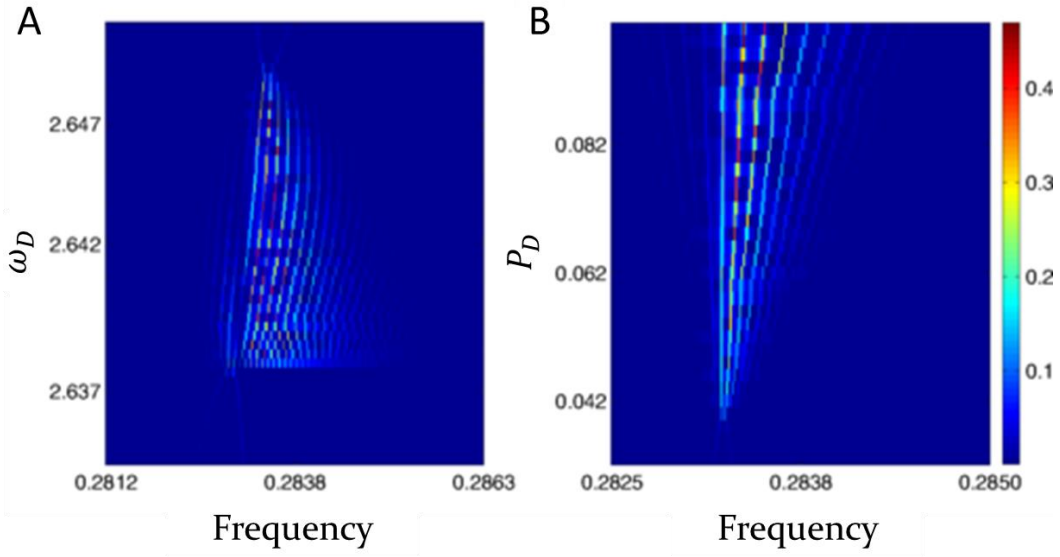

Figure 3.4: $\boldsymbol{\omega_D - P_D}$ **Dependence.** A-B: The frequency spectra of Q_1 for different values of ω_D and P_D respectively. Here, $\alpha = 0.1$. Reprinted figure with permission from [L. S. Cao, D. X. Qi, R. W. Peng, M. Wang, and P. Schmelcher, *Physical review letters,* vol. 112, p. 075505, 2014.] Copyright (2014) by the American Physical Society.

Chapter 4

Micromechanical Resonator – An Experimental Analogue of Fermi-Pasta-Ulam Chains

In Chapter 3, the general formalism of FPU chain was introduced. The theoretical prediction of PFC associated with a 10-site FPU-α chain was then presented. While the numerical analyses of FPU chains can bring in interesting new insights similar to PFC, the typical timescales associated with the concomitant computations may be long enough to demand exorbitant resources. While such numerical attempts cannot be avoided owing to their own importance for model identification, the complementary experimental analogues of FPU chains can instantaneously compute the solutions of relevant FPU phenomena, for instance, PFC. Also, such experimental signatures are required for the practical utilization of FPU mechanisms. To this end, this chapter presents an experimental analogue of FPU chains.

4.1. Why Micromechanical Resonators?

Various FPU phenomena for instance, PR [28, 43-64] are observed in disparate physical systems including elementary particles [43-44], astrophysics [45], fluid mechanics [28, 46-48], magnetism [49], electronics [50], optical lasers [51-52], mechanics [53-62] and biophysics [63-64]. Hence, based on dynamic similarity, it is possible to analogize a virtual FPU chain to all of these physical systems. In other words, such physical systems can form experimental analogues of FPU chains. However, "micromechanical resonators" present unique attributes for studying FPU physics as outlined below.

- Multiple Normal Modes: To explore rich FPU phenomena, it is important for the physical system to possess multiple normal modes. Interestingly, even the simplest topology of micromechanical resonators can be set in multiple modes of vibration (Figure 4.4).

- Strong Normal Mode Coupling: In addition to the presence of multiple normal modes, the coupling between such modes should be strong enough to produce rich dynamics.

However, for this purpose, large unrealistic drive power levels are usually necessary. Fortunately, the miniaturized mechanical resonators, owing to smaller drive power level handling capability, can exhibit strong modal coupling even at nominal drive power levels.

- Ease of Experimental Control: To systematically study and model FPU phenomena, the experimental system should be easily controllable with a high degree of precision. As the silicon-based micro-/nanofabrication technology (Appendix A) is well-established, it is possible to control geometry and material properties for such resonators with high precision.

- Informative Experimental Characterization: To extract meaningful information about FPU phenomena, the experimental system should be properly characterized and the resulting characteristics should be independently validated. The micromechanical resonators can be characterized through multiple techniques including electrical (Section 4.5.1) and optical (Section 4.5.2). Hence, by correlating experimental results measured by 2 or more separate techniques, any artefacts associated with any particular experimental technique can be eliminated.

4.2. Piezoelectric Micromechanical Resonators

Micromechanical resonators can be interfaced through various means. A popular approach is using 'electrostatic methods' [65-68]. Here, as the name suggests, the micromechanical resonator is driven by the electrostatic forces. In this device topology, the electrodes are defined in close proximity of micromechanical resonator to form a parallel-plate [67-68] or comb drive [65-66] arrangement. When an oscillating electrical signal is applied to this electrode, mechanical vibrations are set up in the micromechanical resonator. A polarization voltage is commonly employed to linearize the transducer response and allow for a linear voltage-to-force, and current-to-velocity motional response. However, due to weak electromechanical coupling, the amplitude of such excitations is typically low and the method is usually only effective for interfacing a very specific mode of interest, such that the electrodes are defined specifically to interrogate a particular mode. However, a piezoelectric micromechanical resonator [69-72], in contrast to the aforementioned configurations, can be an ideal candidate for the FPU experimental analogue due to strong electromechanical

coupling offered by its implementation. The topology of a representative piezoelectric micromechanical resonator is depicted in Figure 4.1.

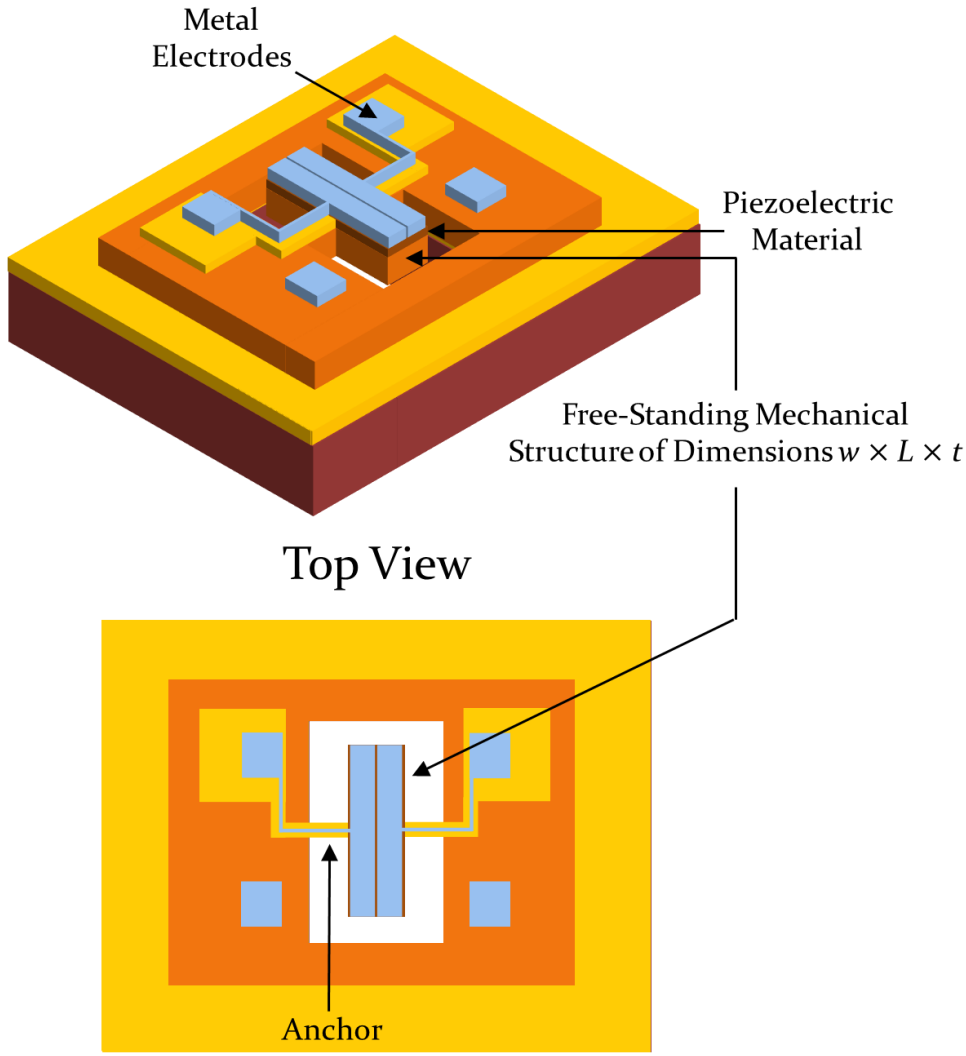

Figure 4.1: **Piezoelectric Micromechanical Resonator.** A piezoelectric material coated free-standing mechanical structure of dimensions $w \times L \times t$. The electrical signals are applied and extracted from the Input/Output (I/O) metal pads. The electrical field is set up across the piezoelectric material through the adjoining metal electrodes.

A piezoelectric thin film coating forms the functional component of piezoelectric micromechanical resonator. When an electrical field is applied across this thin film, the mechanical deformation of film and underlying device layer occurs. Conversely, the mechanical deformation will also result in the generation of charge across the electrode plates. In this device topology, a thin layer of piezoelectric material is attached to a conducting or

semiconducting micromechanical resonator. In addition, on top of the piezoelectric film, a conducting (for instance, metal) layer is also added. Now, when an oscillating electrical signal is applied on this metal electrode with respect to the micromechanical resonator, the piezoelectric transduction of a phonon mode of eigenfrequency closer to the drive frequency takes place. Relative to the electrostatic counterpart, owing to higher electromechanical coupling, the amplitude of excitations is often larger for the same drive levels, particularly for high frequency modes.

4.3. Design of Piezoelectric Micromechanical Resonators

For the design of piezoelectric micromechanical resonator, the built-in 'piezoelectric devices' module of COMSOL® Multiphysics 4.3a [73] is utilized. Through this sophisticated software tool, the piezoelectric micromechanical structure of interest can be 3-D modelled and the characteristics of its phonon modes including the eigenfrequencies and spatial displacement profiles can be predicted.

4.3.1. 3D Simulation of Piezoelectric Micromechanical Resonator

The simulation is based on Finite Element Method (FEM). Here, the bounded continuous domain is decomposed into a finite number of elements for which an approximate solution is produced (Figure 4.2). The simulation steps are listed below:

1. Definition of Physical Geometry

Here, the variables corresponding to the geometry of piezoelectric micromechanical resonator are defined.

2. Definition of Material Parameters

For all of the component layers including piezoelectric, metal and silicon, the mechanical parameters including density ρ, Young's modulus matrix $[E]$, Poisson's ratio σ and shear modulus $[G]$ are defined. Particularly, for the piezoelectric material, the relative electrical permittivity matrix $[\epsilon_r]$ and piezoelectric coupling matrix $[e]$ are also defined. Further, for

capturing information about the material related quality factor, the damping ratio ζ can also be defined.

3. Definition of Physical Problem and Boundary Conditions

In the simulation of piezoelectric micromechanical resonator, the amount of electrical charge which is generated in the piezoelectric film for an applied electrical potential is computed at first. This electrical charge is then converted to mechanical strains based on the associated piezo-electromechanical coupling relationship. The corresponding stresses are then used to estimate the 3D displacement distribution of structure. While the electrical charge distribution quantifies the electrical behaviour, the displacement profile describes the mode shapes. In this definition of physical problem, the electrical and mechanical boundary conditions should also be provided appropriately as: the interface between the top electrode and piezoelectric layers is at $+V/2$; the interface between the bottom electrode and piezoelectric layers is at $-V/2$; the displacements are set to 'o' at the locations of mechanical anchors.

4. Discretization of Structure

Prior to the simulation, the structure is discretized into a number of elements (Figure 4.2) that can produce reasonably good convergence to the desired solution. The mesh structure i.e., tetrahedral, hexahedral or a combination of these has to be appropriately chosen so as to have minimal numerical errors.

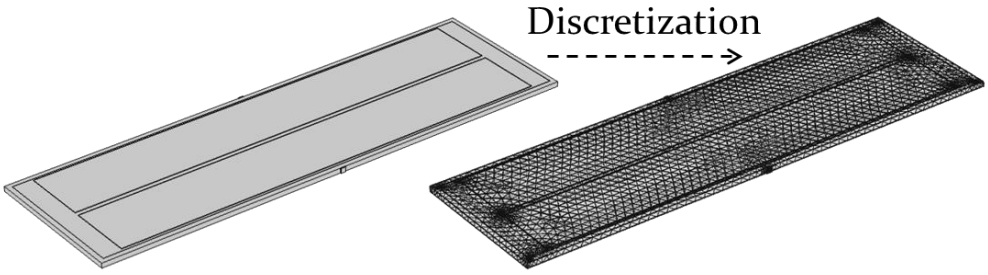

Figure 4.2: **Discretization of Structure.**

5. Simulation of the Structure

For the simulation, the eigenfrequency study is considered. The eigenfrequency analysis is carried out to obtain the eigenfrequencies and spatial vibration patterns of phonon modes associated with the structure.

4.3.2. Simulation Results

We consider a piezoelectric micromechanical structure of free-free beam topology. The schematic of this device is presented in Figure 4.3.

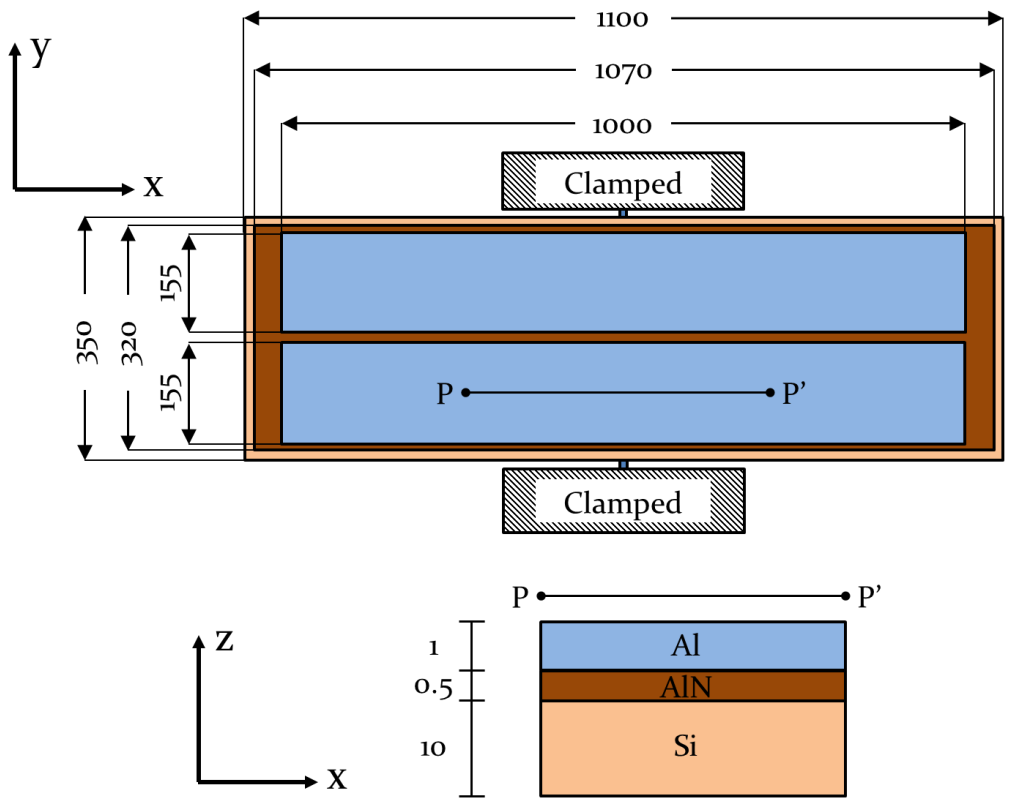

Figure 4.3: **Schematic of Piezoelectric Micromechanical Free-Free Beam Structure.** An Aluminium Nitride (AlN) and Aluminium (Al) coated Silicon (Si) structure of dimensions $1100 \times 350 \times 10$ supported by anchors of dimensions $2 \times 20 \times 10$. Here, the dimensions are in μm units.

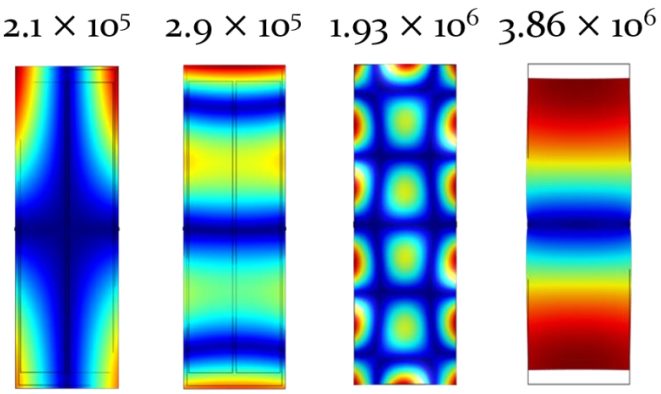

Figure 4.4: **Multiple Eigenmodes of Piezoelectric Micromechanical Free-Free Beam Structure.** The eigenfrequencies (in Hz) corresponding to each eigenmode of piezoelectric micromechanical resonator.

Now, based on the background presented in Section 4.3.1, a micromechanical free-free beam is simulated using COMSOL Multiphysics 4.3a. Figure 4.4 showcases multiple eigenmodes and corresponding eigenfrequencies associated with this micromechanical resonator. The mode of frequency 3.86 *MHz* is a length extensional mode where the beam expands and squeezes along its length. While the choice of micromechanical resonator is justified in the section 4.1, there is no specific rationale behind the choice of exact microscale dimensions. However, a length-extensional mode of micromechanical resonator has been chosen as the driven mode. Hence, a free-free beam topology which naturally involves length extensional modes has been considered. Alternatively, a cantilever topology may also be considered. The reasons for the choice of length-extensional mode are as follows: 1. the length extensional mode of free-free micromechanical beam has higher frequency and many modes are usually associated at frequencies lower than the frequency of extensional mode. Owing to this high modal density, the frequency matching conditions for the excitation of phononic frequency combs can be easily achieved. 2. The length extensional mode has greater strain energy. Hence, the drive level thresholds for the excitation of phononic frequency combs can be lower.

4.4. Fabrication of Piezoelectric Micromechanical Resonator

To fabricate piezoelectric micromechanical resonators, a MEMSCAP foundry process named PiezoMUMPs is consulted [74-75]. Appendix A presents the PiezoMUMPs process flow in the context of building a micromechanical free-free beam architecture which is simulated in

Section 4.3.2. Figure 4.5 shows the schematic of microfabricated piezoelectric micromechanical resonator.

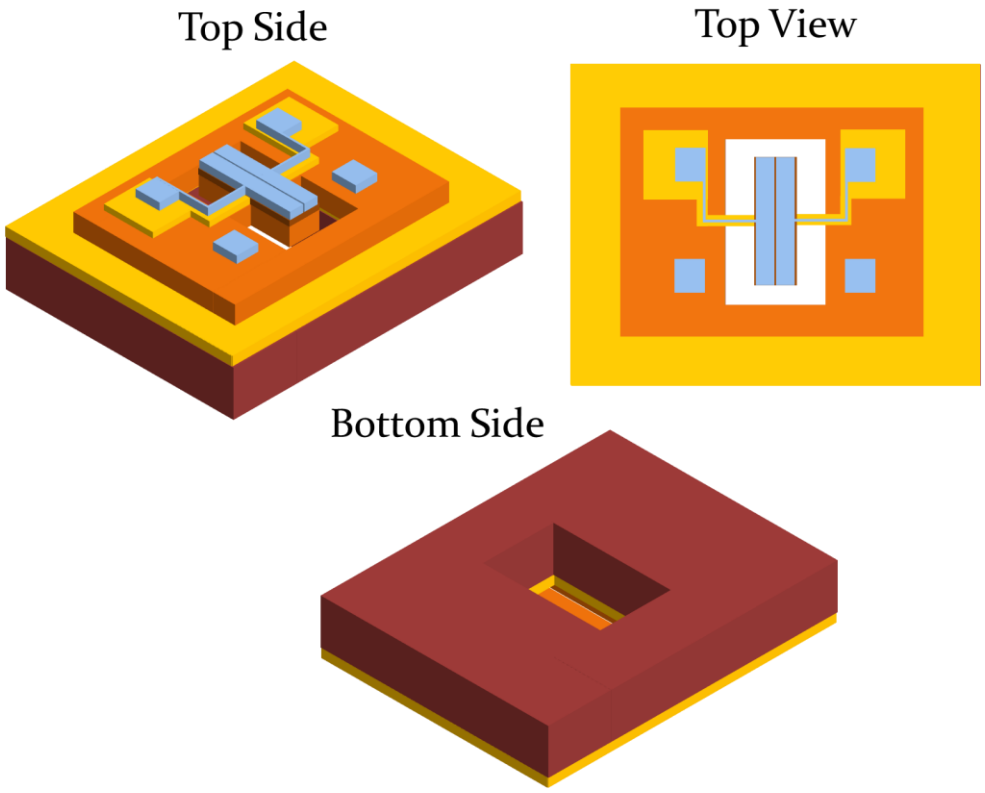

Figure 4.5: **Microfabricated Piezoelectric Free-Free Beam Resonator.**

To fabricate piezoelectric micromechanical resonators, a MEMSCAP foundry process named PiezoMUMPs is consulted [74-75]. Appendix A presents the PiezoMUMPs process flow in the context of building a micromechanical free-free beam architecture which is simulated in Section 4.3.2. Figure 4.5 shows the schematic of microfabricated piezoelectric micromechanical resonator.

4.5. Characterization of Piezoelectric Micromechanical Resonator

The fabricated Si chip (11 mm x 11 mm) is glued onto a ceramic leadless chip carrier (LCC44 Spectrum Semiconductors) (Figure 4.6). The electrical connections from the chip to the carrier are made through wire bonding using a wedge wire bonder (Kulike & Soffa 4523 Digital Wedge Bonder). The LCC package is then placed on a LCC burn-in socket (P2044S-A-AU,

Plastronics) which is in turn soldered to a customized plastic circuit board and the electrical connections in to and out from the board are through the RF-SMA ports (Figure 4.6).

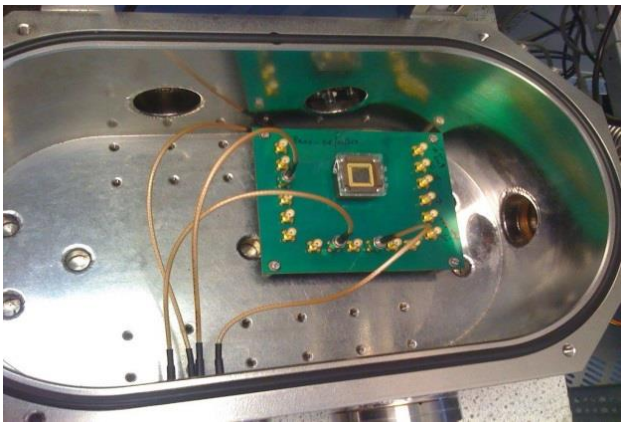

Figure 4.6: Circuit board, with the Si-chip glued onto the leadless chip carrier, is placed in the vacuum chamber

4.5.1. Electrical Characterization

The piezoelectric resonator is driven and sensed in two-port configuration (Figure 4.7). Here, the top Si layer of SOI wafer is grounded. The drive and sense are through the split Al patterns which are adjoined to the AlN film.

4.5.1.1. Drive and Sense: Network Analyser

Here, we characterize the frequency response of piezoelectric micromechanical resonance utilizing Agilent Network Analyser 4391B. The input and output ports of network analyser are connected to the drive and sense electrodes of device respectively. The transmission parameter S21 is displayed on the screen of Agilent Network Analyser 4391B as the frequency of source is swept (Figure 4.8).

4.5.1.2. Drive: Waveform Generator and Sense: Oscilloscope

The electrical outputs derived from a waveform generator (Agilent 33220A and/or 335ARB1U) are connected to the drive electrode of device and the electrical signal which is transduced by

the sense electrode of device is probed using an oscilloscope (Agilent Infiniium 54830B DSO) (Figure 4.9).

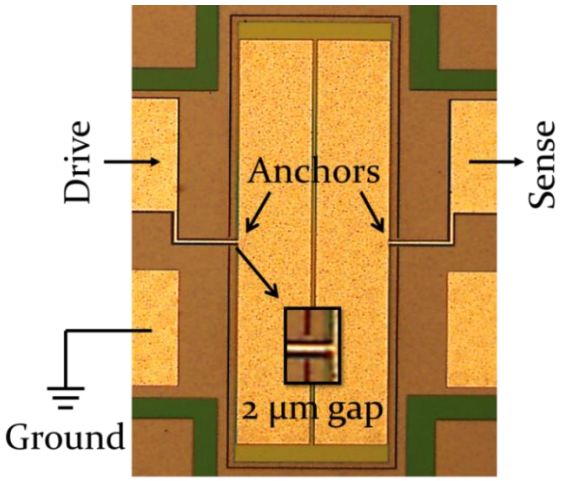

Figure 4.7: **Two-Port Configuration.**

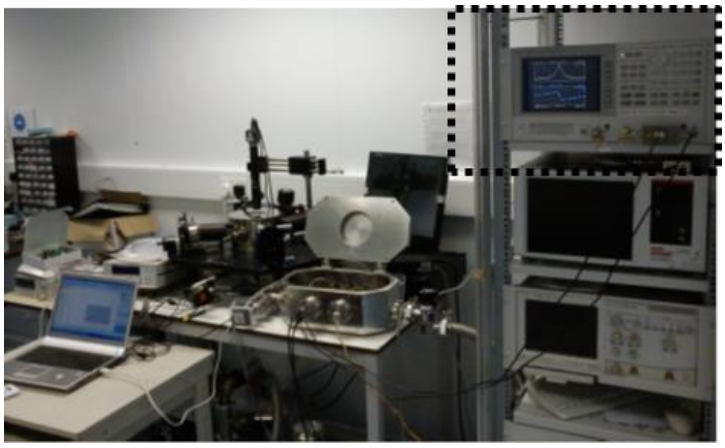

Figure 4.8: **Electrical Characterization using Network Analyser (dotted box).**

4.5.2. Optical Characterization

The piezoelectric resonator is driven in two-port configuration (Figure 4.7). Here, the top Si layer of SOI wafer is grounded. The electrical output derived from a waveform generator (Agilent 335ARB1U) is connected to the drive electrode of device and the resulting mechanical vibrations of device are probed using a laser Doppler vibrometer (LDV) (Polytec MSA-400 Micro System Analyzer) (Figure 4.10).

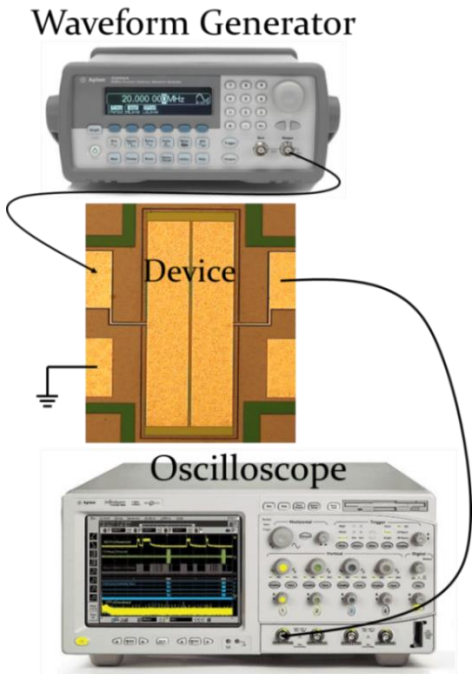

Figure 4.9: **Electrical Characterization using Oscilloscope.**

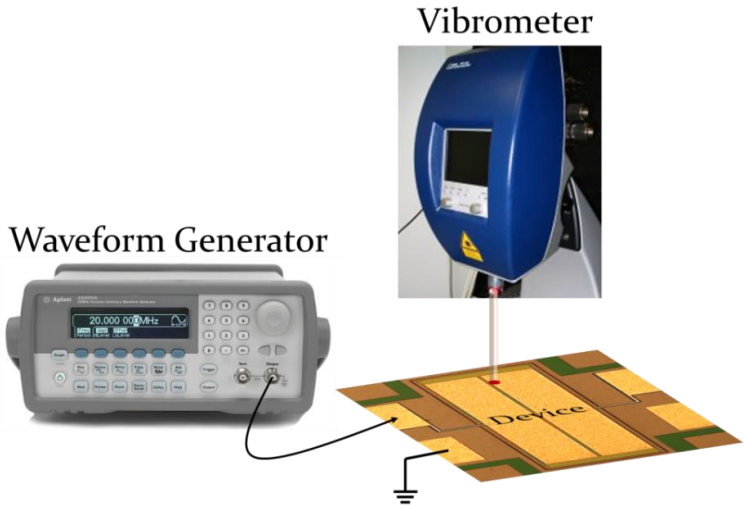

Figure 4.10: **Optical Characterization using Laser Doppler Vibrometer.**

4.6. Summary

In Sections 4.1 and 4.2, we have discussed the rationale behind the choice of piezoelectric micromechanical resonators as an experimental FPU analogue. In Sections 4.3, 4.4 and 4.5, we

have discussed both general and specific device-oriented aspects concerning the design, fabrication and characterization of piezoelectric micromechanical resonators.

Chapter 5

Observation of Phononic Frequency Combs in a Micromechanical Resonator

The theoretical basis for PFC in a FPU chain and design of a micromechanical resonator based FPU analogue were discussed in the previous chapters. Now, this chapter presents experimental results demonstrating the generation of PFC in the FPU analogue of piezoelectric micromechanical resonator.

5.1. Definition of Dynamics

To recapitulate, the equations of motion for a multimode micromechanical resonator (abstracted by α-FPU dynamics) are given by

$$\ddot{Q}_q + \omega_q^2 Q_q + 2\zeta_q \dot{Q}_q = -\alpha_{FPU} \sum_{i,j=1}^{N} A_{q,i,j} Q_i Q_j + P; q = 1,2, \dots, N \tag{5.1}$$

Here, Q_q is the displacement of mode q, ω_q and ζ_q are the natural frequencies and damping ratios of mechanical modes of micromechanical resonator respectively. The coefficients $A_{q,i,j}$ of nonlinear terms associated with the mode Q_q quantify the degree of coupling between the modes Q_i and Q_j.

These equations of motion of a multimode micromechanical resonator are dynamically similar to those of a N-site FPU-α chain (Chapter 3). However, the difference lies at the interpretation of domain-specific results. While the numerical results presented in Section 3.4 captured the motion of each phonon mode of N-site FPU chain, the trends associated with the displacement amplitudes of each mode of micromechanical resonator are reported in this chapter.

5.2. Observation of Phononic Frequency Combs via Two-Mode Three-Wave Mixing

To experimentally observe PFC via intrinsic three-wave mixing [13], the electrical drive $S_{in}(\omega_D) \propto (P = P_D \cos(\omega_D t))$ which is applied to the micromechanical resonator is suitably adjusted. At $S_{in}\left(\frac{\omega_D}{2\pi} = 3.862\ MHz\right) = 5\ dBm$, the LDV (Section 4.5.2) detected the presence of phase-coherent PFC.

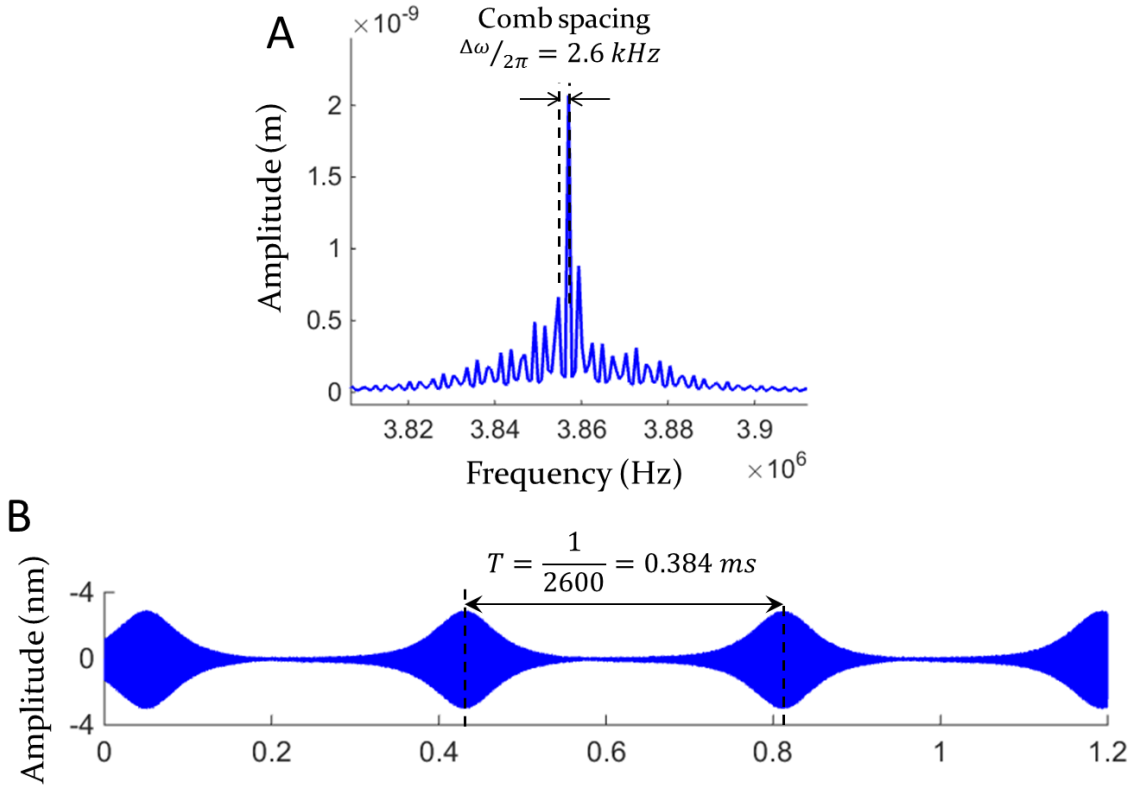

Figure 5.1: A & B: **Spectral and Temporal Signatures of Frequency Combs.** Here, the electrical drive $S_{in}\left(\frac{\omega_D}{2\pi} = 3.862\ MHz\right) = 5\ dBm$.

Figure 5.1A shows the spectral signature of PFC i.e. the precisely positioned frequencies of equidistant spacing $\frac{\Delta\omega}{2\pi} = 2.6\ kHz$ and Figure 5.1B shows the corresponding temporal manifestation which is the train of pulses of period $\frac{2\pi}{\Delta\omega} = 0.384\ ms$.

To explore the generation process underpinning this intriguing PFC, the experiments were systematically carried out at different drive conditions and the resulting spectra are electrically probed (Section 4.5.1.2). To start with, the S_{in} dependence of PFC for $\frac{\omega_D}{2\pi} = 3.862\ MHz$ is examined. When $S_{in} < 3.5\ dBm$, only the tone corresponding to $\frac{\omega_D}{2\pi}$ is observed (Figure 5.2A). However, once S_{in} crosses this threshold value, the PFC process onsets. As S_{in} is increased, the number of spectral lines of such PFC enlarges. However, this only happens at discrete steps due to the cascade of inherent thresholds associated with every other high order nonlinear interaction. While the PFC generation threshold for $\frac{\omega_D}{2\pi} = 3.862\ MHz$ is $3.5\ dBm$, the ω_D dependence of such a threshold is now studied. When $\frac{\omega_D}{2\pi}$ is between $3.86\ MHz$ and $3.8608\ MHz$, PFC is not formed even at extreme values of S_{in} (Figure 5.2B). However, above $\frac{\omega_D}{2\pi} = 3.8608\ MHz$, the emergence of PFC is evidenced and the associated generation threshold decreases with increase in $\frac{\omega_D}{2\pi}$ (Figure 5.2B).

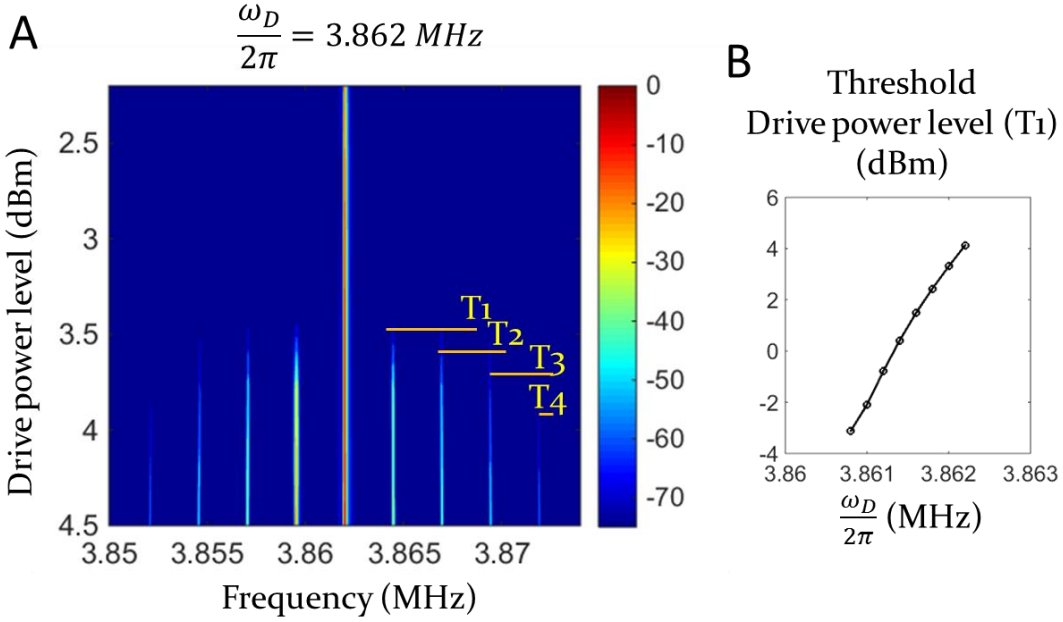

Figure 5.2: **Thresholds for Frequency Comb Excitations.** Dependence with A: electrical drive power level (S_{in}) and B: drive frequency ($\frac{\omega_D}{2\pi}$).

At $S_{in} > 5$ dBm, we also evidence the onset of another attribute in PFC (Figure 5.3). Here, the spacing $\Delta\omega$ of PFC broadens as S_{in} is increased. While the nominal regime of PFC is termed as 'Direct Nonlinear Resonance (DNR)' (equivalent to Figure 5.2A), we refer to this PFC broadening regime as 'DNR+Duffing'. In DNR, the increase in S_{in} merely results in the

increase in the number of spectral lines associated with PFC while the corresponding $\Delta\omega$ stays constant. As contrasted with DNR, in Duffing-DNR, $\Delta\omega$ increases with S_{in}. While the contrasting S_{in} dependences of PFC in the DNR and DNR-Duffing regimes are clear, we now seek ω_D dependence of PFC in each of these two regimes.

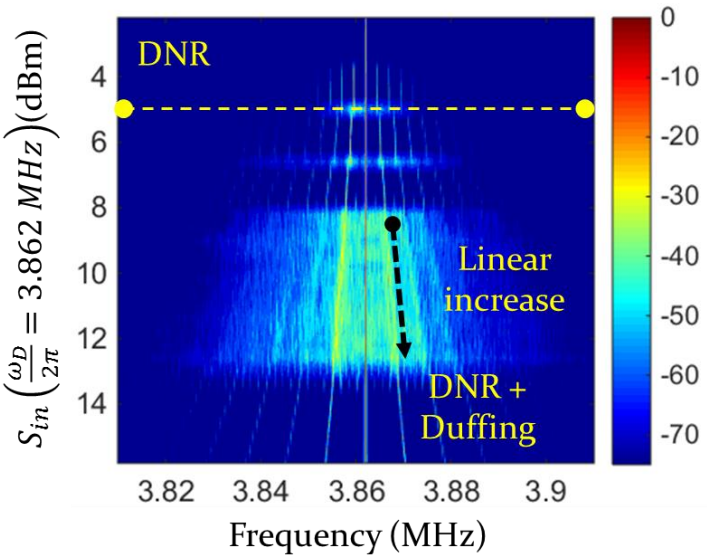

Figure 5.3: **Onset of Duffing Phenomenon (By Varying the Drive Power Level S_{in}).**

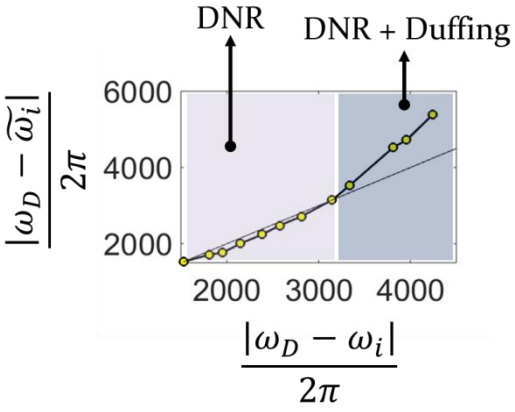

Figure 5.4: **Onset of Duffing Phenomenon (By Varying the Drive Frequency $\frac{\omega_D}{2\pi}$).**

To this end, $\frac{\omega_D}{2\pi}$ is first detuned and the corresponding S_{in} is adjusted such that the number of frequency comb lines stays constant at 5. When $\frac{\omega_D}{2\pi}$ is between 3.86 MHz and 3.8622 MHz, $\Delta\omega = |\omega_D - \widetilde{\omega}_i|$ matches up with $|\omega_D - \omega_i|$ (Figure 5.4). (Here, ω_i and $\widetilde{\omega}_i$ are the nominal and amplitude dependent resonant frequencies of the driven mode respectively.) In other words,

$\tilde{\omega}_i$ is S_{in} independent and is constant at its nominal value ω_i. However, when $\frac{\omega_D}{2\pi}$ is increased above 3.8622 MHz, $\Delta\omega$ deviates from $|\omega_D - \omega_i|$ (Figure 5.4). And, such a deviation is due the emergence of DNR-Duffing regime. While the PFC (of 5 spectral lines) corresponding to the $\frac{\omega_D}{2\pi}$ range of $3.86 - 3.8622$ MHz fall under DNR regime, the transition to DNR+Duffing regime occurs when $\frac{\omega_D}{2\pi}$ is increased above 3.8622 MHz. This, in other words, means that the number of spectral lines associated with PFC, at the point of transition from the DNR to DNR-Duffing regime, need not be the same for the entire range of ω_D,.

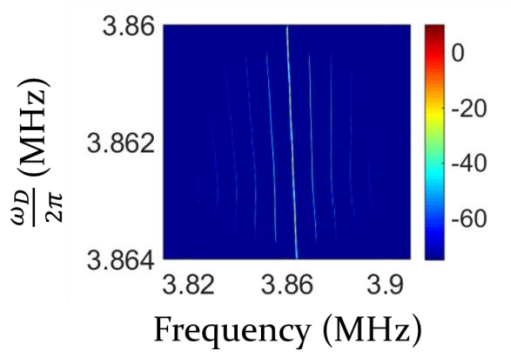

Figure 5.5: **Drive Frequency Dependence of Frequency Combs under 'DNR+Duffing' Regime.**

In the DNR regime, $\Delta\omega$ can only be controlled by $\frac{\omega_D}{2\pi}$ but not S_{in} (Figures 5.2 and 5.4). However, in the DNR+Duffing regime, this may not be the case. Hence, to study this trend, we detune $\frac{\omega_D}{2\pi}$ while also keeping S_{in} constant at a high enough value of 23 dBm such that PFC is in DNR+Duffing regime. Figure 5.5 shows that $\Delta\omega$ does not vary with $\frac{\omega_D}{2\pi}$. Instead, the entire PFC collectively shifts with $\frac{\omega_D}{2\pi}$. This arises due to the direct dependence of $\tilde{\omega}_i$ with $\frac{\omega_D}{2\pi}$ such that $\Delta\omega = |\omega_D - \tilde{\omega}_i|$ is constant. Hence, in the DNR+Duffing regime, $\Delta\omega$ can only be controlled by S_{in} but not $\frac{\omega_D}{2\pi}$ (Figures 5.3 and 5.5).

Hence, we have now studied two distinct DNR and DNR+Duffing regimes of two-mode three-wave mixing based PFC. We will now discuss the correspondence of PFC to the typical Lorentzian resonant response of the driven phonon mode. The PFC is formed only when $\frac{\omega_D}{2\pi}$ is detuned above a specific threshold value of δ_{PFC} (Figure 5.6). The span of $\omega_D = (\omega_i \pm \delta_{PFC})$ which does not constitute PFC is termed as 'Dispersion band' and the PFC regime falls right

outside this band. We also know that the PFC is generated only when S_{in} crosses a concomitant threshold value (Figure 5.2) and such a threshold is directly proportional to δ_{PFC}. Hence, the span of PFC regime is set by S_{in}. While the dispersion band sets a constant interior bound of PFC regime, its exterior bound can however be tuned by S_{in} (Figure 5.6).

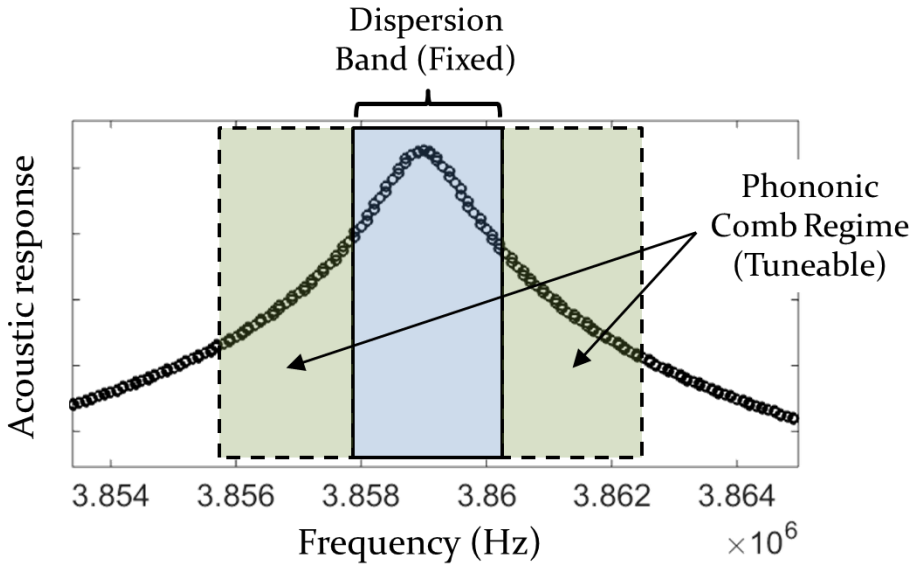

Figure 5.6: **Experimentally Observed Operational Regime of Phononic Frequency Combs.**

5.3. Observation of Phononic Frequency Combs via Two-Mode Pumped Three-Wave Mixing

5.3.1. Nominal Observations of Frequency Combs

To experimentally observe PFC via pumped three-wave mixing [76], we apply two drive tones to the micromechanical resonator. That is, the drive P of equation 5.1 is equal to $P_D \cos(\omega_D t) + P_P \cos(\omega_P t)$. Here, one of the drive tones is also referred to as 'pump'. The amplitudes and frequencies of this pump are P_P and ω_P respectively. Also, the electrical drives $S_{in}(\omega_D) \propto (P_D \cos(\omega_D t)); S_{in}(\omega_P) \propto (P_P \cos(\omega_P t))$. Now, when the drive condition is tuned to $S_{in}\left(\frac{\omega_D}{2\pi} = 3.855\ MHz\right) = 4\ dBm; S_{in}\left(\frac{\omega_P}{2\pi} = 3.86\ MHz\right) = 12\ dBm$, the motion corresponding to a series of spectral lines with equidistant spacing of $\frac{|\omega_D - \omega_P|}{2\pi} = 5\ kHz$ is launched in the micromechanical resonator (Figure 5.7).

Now, to understand the mechanism of PFC generation, the drive conditions are systematically controlled and the resulting vibrations are probed using LDV. For this experimental study, we have four control parameters: $\frac{\omega_D}{2\pi}$, $S_{in}\left(\frac{\omega_D}{2\pi}\right)$, $\frac{\omega_P}{2\pi}$ and $S_{in}\left(\frac{\omega_P}{2\pi}\right)$.

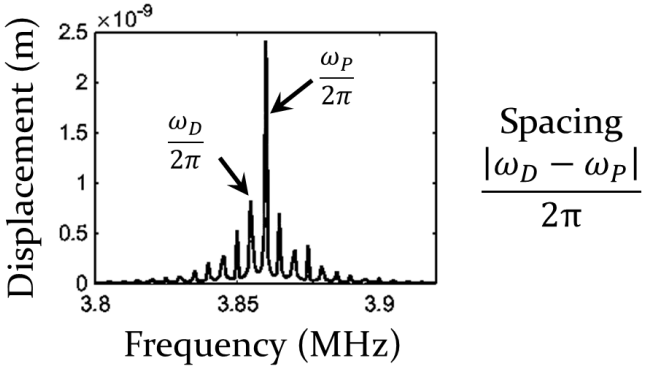

Figure 5.7: **Observation of Frequency Combs via Two-Mode Pumped Three-Wave Mixing.** Here, $S_{in}\left(\frac{\omega_D}{2\pi} = 3.855\ MHz\right) = 4\ dBm; S_{in}\left(\frac{\omega_P}{2\pi} = 3.86\ MHz\right) = 12\ dBm.$

To start with, we keep $\frac{\omega_D}{2\pi}$ and $\frac{\omega_P}{2\pi}$ constant at 3.855 MHz and 3.86 MHz respectively and vary $S_{in}\left(\frac{\omega_D}{2\pi}\right)$ and $S_{in}\left(\frac{\omega_P}{2\pi}\right)$ from 0 dBm to 20 dBm. During this control, we evidence PFC only for a specific set of drive conditions. Figure 5.8 charts out the well-bounded regions of PFC in the $S_{in}\left(\frac{\omega_D}{2\pi}\right) - S_{in}\left(\frac{\omega_P}{2\pi}\right)$ map. In the absence of PFC process, only the frequencies corresponding to the drive tones i.e. $\frac{\omega_D}{2\pi}$ and $\frac{\omega_P}{2\pi}$ are existent in the spectral response. On the other hand, the PFC process results in a series of equidistant spectral lines at $\omega_P + n(\omega_P - \omega_D); n \in Z$.

To observe the spectral line growth of PFC, one of the drive levels $S_{in}\left(\frac{\omega_D}{2\pi} = 3.855\ MHz\right)$ is increased from 0 dBm to 22 dBm by keeping $S_{in}\left(\frac{\omega_P}{2\pi} = 3.86\ MHz\right)$ constant at 14 dBm. At low enough values of $S_{in}\left(\frac{\omega_D}{2\pi} = 3.855\ MHz\right)$ i.e. $< 8\ dBm$, PFC is not formed (Figure 5.9). However, above this threshold, an additional spectral line is generated at the frequency $2\omega_P - \omega_D = \omega_P + (\omega_P - \omega_D)$. With further increase in $S_{in}\left(\frac{\omega_D}{2\pi} = 3.855\ MHz\right)$, a series of spectral lines at $\omega_P + n(\omega_P - \omega_D); n \in Z$ are produced. Thus, the spectral bandwidth of PFC can be controlled by S_{in}. Figure 5.9 also shows the presence of steps during the spectral line growth. These steps

indicate the relevant thresholds for the high-order expansions associated with the PFC process.

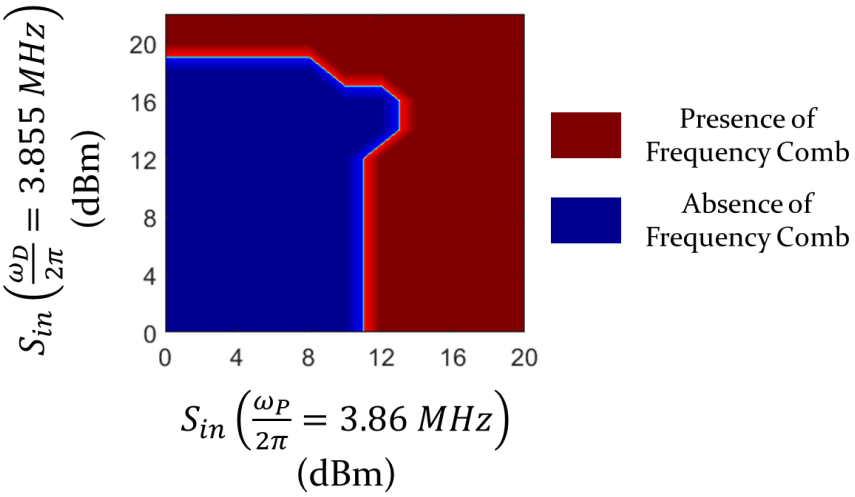

Figure 5.8: $\boldsymbol{S_{in}\left(\frac{\omega_D}{2\pi}\right) - S_{in}\left(\frac{\omega_P}{2\pi}\right)}$ **Map of Frequency Combs.**

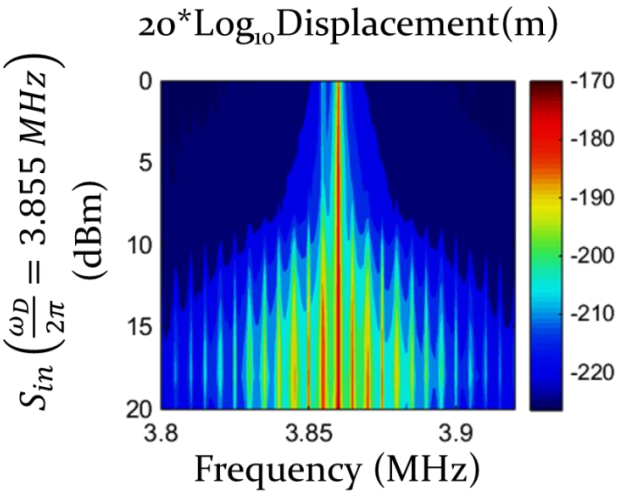

Figure 5.9: **Drive Power Level Dependence.** Here, $S_{in}\left(\frac{\omega_D}{2\pi} = 3.855\ MHz\right) = 4\ dBm; S_{in}\left(\frac{\omega_P}{2\pi} = 3.86\ MHz\right) = 12\ dBm$. Here, $S_{in}\left(\frac{\omega_D}{2\pi} = 3.855\ MHz\right) = 0 - 22\ dBm;\ S_{in}\left(\frac{\omega_P}{2\pi} = 3.86\ MHz\right) = 14\ dBm.$

We thus understood the relevance of S_{in} in PFC via pumped three-wave mixing. In this specific PFC process, the comb spacing $\Delta\omega$ is set by $\frac{\omega_D}{2\pi}$ and $\frac{\omega_P}{2\pi}$ i.e. $\Delta\omega = |\omega_D - \omega_P|$. Hence, if

$\frac{\omega_D}{2\pi}$ and $\frac{\omega_P}{2\pi}$ are altered, $\Delta\omega$ of PFC gets changed as well. To experimentally test this characteristic, $\frac{\omega_D}{2\pi}$ is varied from 3.85 MHz to 3.87 MHz by keeping $\frac{\omega_P}{2\pi}$ constant at 3.86 MHz such that both $\frac{\omega_D}{2\pi}$ and $\frac{\omega_P}{2\pi}$ are still within the resonance bandwidth of the driven phonon mode.

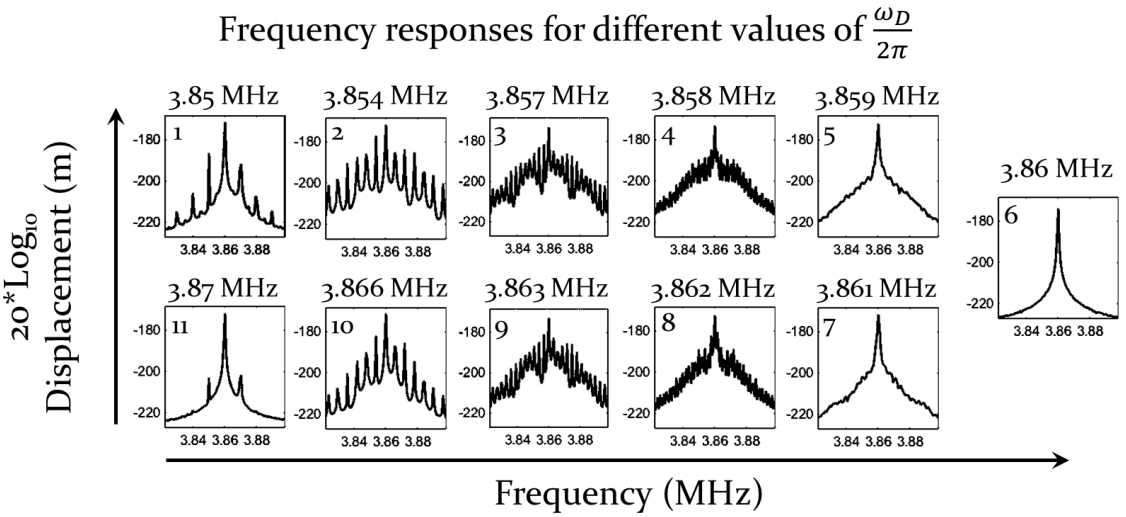

Figure 5.10: **Drive Frequency Dependence.** The frequency responses corresponding to different drive frequencies $\frac{\omega_D}{2\pi} = 3.85, 3.854, 3.857\ 3.858, 3.859, 3.86, 3.861, 3.862, 3.863, 3.866$ and 3.87 MHz (1-11); $S_{in}\left(\frac{\omega_D}{2\pi}\right) = 4\ dBm$; $S_{in}\left(\frac{\omega_P}{2\pi} = 3.86\ MHz\right) = 14\ dBm$.

Figure 5.10 shows the spectral responses for each $\frac{\omega_D}{2\pi} - \frac{\omega_P}{2\pi}$ combination. It can be noted from these figures that $\Delta\omega$ of PFC varies as $\frac{|\omega_D - \omega_P|}{2\pi}$. However, at close-enough separation between $\frac{\omega_D}{2\pi}$ and $\frac{\omega_P}{2\pi}$, the spectral lines become less defined and hence, a clear form of PFC is not produced. This characteristic sets the lower limit on $\Delta\omega$ of PFC utilizing pumped three-wave mixing.

5.3.2. Transitional Characteristics

The previous section (Section 5.3.1.) offered insights into the pumped three-wave mixing based PFC process through the examination of PFC truncated to frequencies $\cong \frac{\omega_D}{2\pi} \cong \frac{\omega_P}{2\pi}$. While the nature and operational regimes of PFC were extracted, some additional details about the PFC process were probably missed owing to the truncation. Hence, we now also analyse the spectra of motion about half the drive frequency.

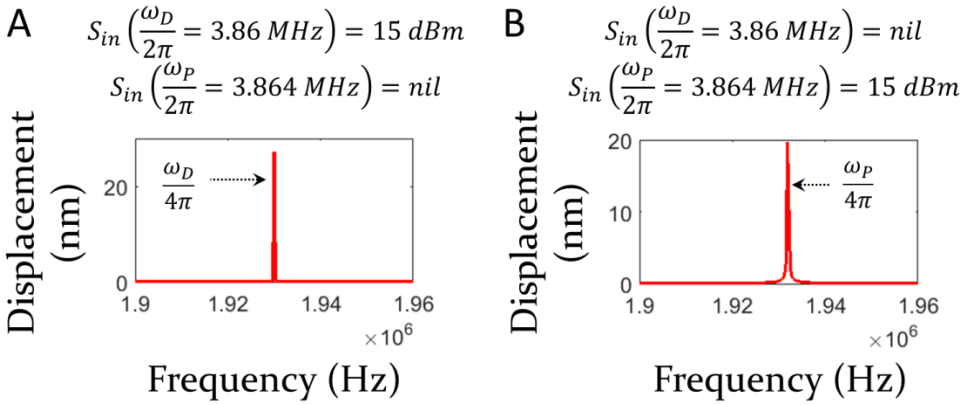

Figure 5.11: **Subharmonic Excitations.** A: $S_{in}\left(\frac{\omega_D}{2\pi} = 3.86\ MHz\right) = 15\ dBm$; B: $S_{in}\left(\frac{\omega_P}{2\pi} = 3.864\ MHz\right) = 15\ dBm$.

At first, only $S_{in}\left(\frac{\omega_D}{2\pi} = 3.86\ MHz\right) = 15\ dBm$ is applied. The frequency spectra detected by LDV revealed the presence of a tone of frequency $\frac{\omega_D}{4\pi} = 1.93\ MHz$ in addition to the drive tone $\frac{\omega_D}{2\pi} = 3.86\ MHz$ (Figure 5.11A). Similarly, when $S_{in}\left(\frac{\omega_P}{2\pi} = 3.864\ MHz\right) = 15\ dBm$ is applied, the tones $\frac{\omega_P}{2\pi} = 3.864\ MHz$ and $\frac{\omega_P}{4\pi} = 1.932\ MHz$ are produced (Figure 5.11B).

Now, when both $S_{in}\left(\frac{\omega_D}{2\pi} = 3.86\ MHz\right)$ and $S_{in}\left(\frac{\omega_P}{2\pi} = 3.864\ MHz\right)$ are introduced, we observed the excitation of PFC consisting of spectral lines at $\omega_P + n(\omega_P - \omega_D); \frac{\omega_P}{2} + n(\omega_P - \omega_D);\ n \in Z$ (Figure 5.12).

When only $S_{in}\left(\frac{\omega_D}{2\pi} = 3.86\ MHz\right)$ was applied, the tone of $\frac{\omega_D}{4\pi} = 1.93\ MHz$ was generated. However, when $S_{in}\left(\frac{\omega_D}{2\pi} = 3.86\ MHz\right)$ is applied together with $S_{in}\left(\frac{\omega_P}{2\pi} = 3.864\ MHz\right)$, the tone of $\frac{\omega_D}{4\pi}\left(\notin \frac{1}{2\pi}\left(\frac{\omega_P}{2} + n(\omega_P - \omega_D)\right);\ n \in Z\right)$ is not produced (Figure 5.12). This result thus points to a potentially complex characteristic. Now, to seek clarity on this specific aspect, the drive conditions are systematically varied and the frequency spectra about $1.9 - 1.96\ MHz$ are examined.

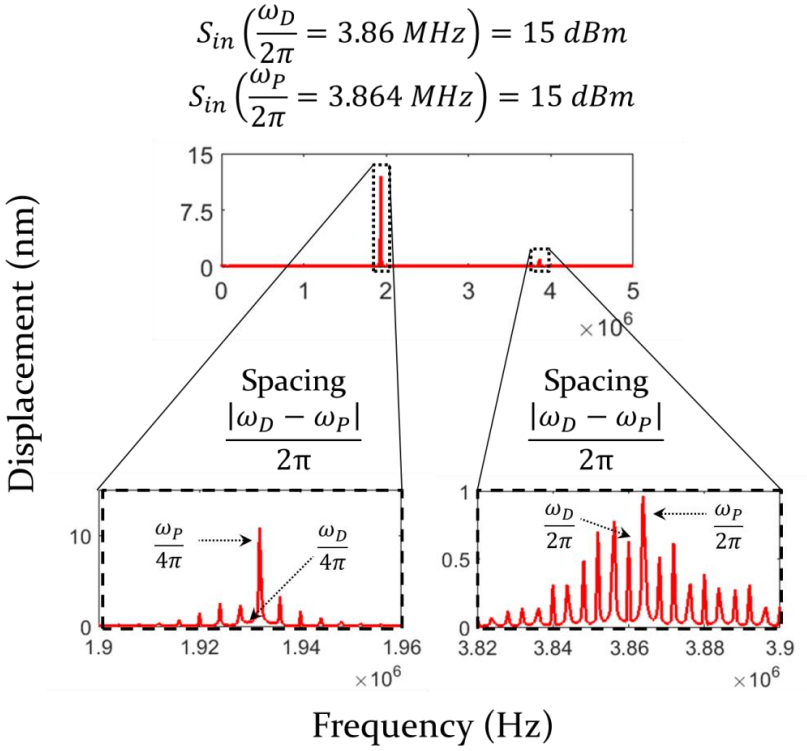

Figure 5.12: **Observations of Frequency Combs.** Here, $S_{in}\left(\frac{\omega_D}{2\pi} = 3.86\ MHz\right) = 15\ dBm$; $S_{in}\left(\frac{\omega_P}{2\pi} = 3.864\ MHz\right) = 15\ dBm$.

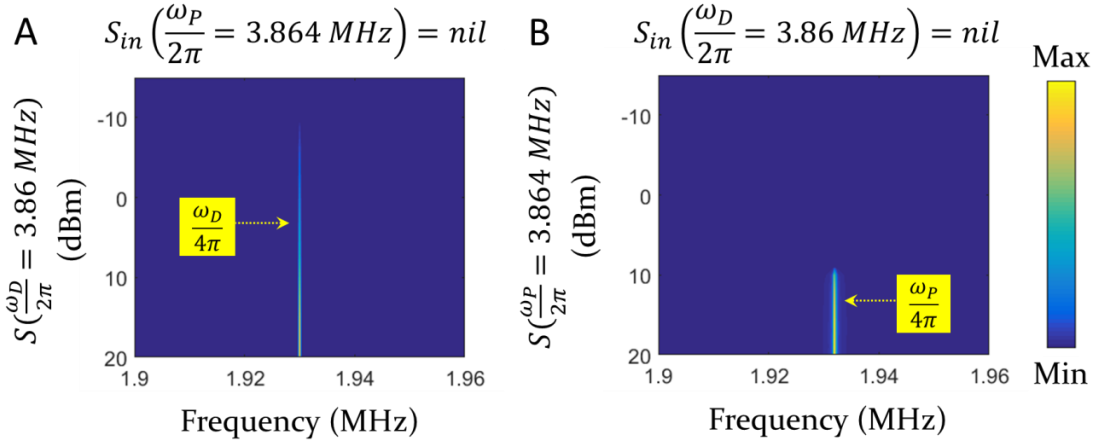

Figure 5.13: **Thresholds for Subharmonic Excitations [77].** The displacement contours: A: $S_{in}\left(\frac{\omega_D}{2\pi} = 3.86\ MHz\right) = -15 - 20\ dBm$; B: $S_{in}\left(\frac{\omega_P}{2\pi} = 3.864\ MHz\right) = -15 - 20\ dBm$.

For the controls, $\frac{\omega_D}{2\pi}$ and $\frac{\omega_P}{2\pi}$ are first individually applied at varying values of S_{in}. Figures 5.13A and 5.13B depict the S_{in} thresholds for the excitation of $\frac{\omega_D}{4\pi}$ and $\frac{\omega_P}{4\pi}$ respectively and the thresholds are $-10\ dBm$ and $10\ dBm$ respectively.

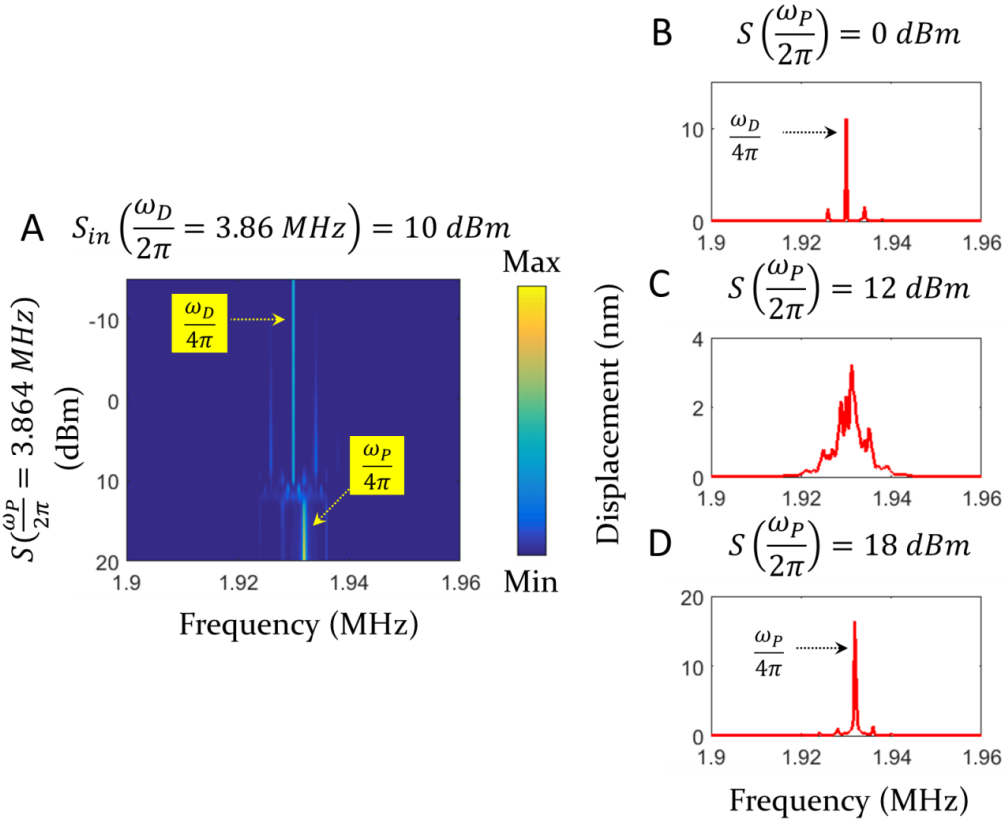

Figure 5.14: **Transitional Characteristics of Frequency Combs.** A: The displacement contour: $S_{in}\left(\frac{\omega_D}{2\pi} = 3.86\ MHz\right) = 10\ dBm$; $S_{in}\left(\frac{\omega_P}{2\pi} = 3.864\ MHz\right) = -15 - 20\ dBm$; B-C: The frequency spectra for $S_{in}\left(\frac{\omega_D}{2\pi} = 3.86\ MHz\right) = 10\ dBm$; $S_{in}\left(\frac{\omega_P}{2\pi} = 3.864\ MHz\right) = 0\ dBm$, $S_{in}\left(\frac{\omega_D}{2\pi} = 3.86\ MHz\right) = 10\ dBm$; $S_{in}\left(\frac{\omega_P}{2\pi} = 3.864\ MHz\right) = 12\ dBm$ and $S_{in}\left(\frac{\omega_D}{2\pi} = 3.86\ MHz\right) = 10\ dBm$; $S_{in}\left(\frac{\omega_P}{2\pi} = 3.864\ MHz\right) = 18\ dBm$ respectively.

Now, we feed $\frac{\omega_D}{2\pi}$ and $\frac{\omega_P}{2\pi}$ together and $S_{in}\left(\frac{\omega_P}{2\pi} = 3.864\ MHz\right)$ is varied by keeping $S_{in}\left(\frac{\omega_D}{2\pi} = 3.86\ MHz\right)$ constant at $10\ dBm$.

As shown in Figure 5.14A, the PFC of $\frac{\omega_D}{2} + n(\omega_P - \omega_D);\ n \in Z$ is observed for low values of S_{in}. However, for $S_{in} > 10\ dBm$, the PFC of $\frac{\omega_D}{2} + n(\omega_P - \omega_D);\ n \in Z$ (Figure 5.14B) transitions into

$\frac{\omega_P}{2} + n(\omega_P - \omega_D)$; $n \in Z$ (Figure 5.14D). Here, such a cross-over occurs despite the largeness of $S_{in}\left(\frac{\omega_D}{2\pi} = 3.86\ MHz\right)$ $(= 10\ dBm)$. Also, in between the two characteristic PFC $(\frac{\omega_D}{2} + n(\omega_P - \omega_D)$; $n \in Z$ and $\frac{\omega_P}{2} + n(\omega_P - \omega_D)$; $n \in Z)$, there also exists a transition regime where the PFC is ill-defined (Figure 5.14C).

5.4. Observation of Phononic Frequency Combs via Three-Mode Four-Wave Mixing

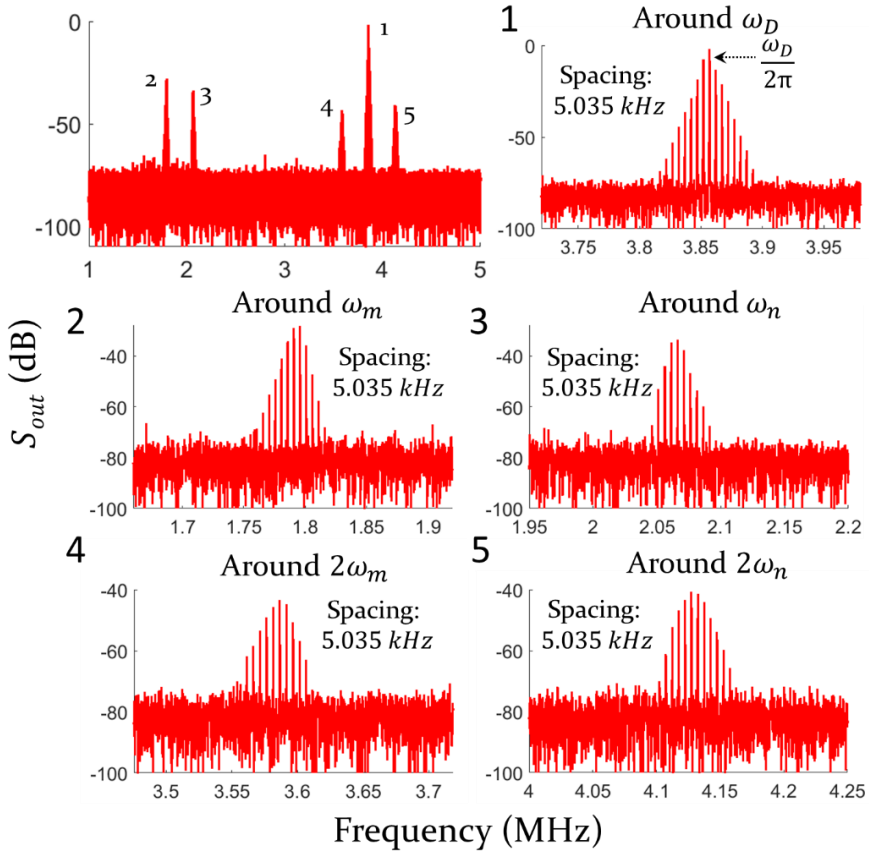

Figure 5.15: **Phononic Frequency Combs via Three-Mode Four-Wave Mixing.** The frequency spectrum of output electrical signal S_{out} for $S_{in}\left(\frac{\omega_D}{2\pi} = 3.857\ MHz\right) = 15\ dBm$; 1-5: The zoomed views of spectral features 1-5 respectively.

The PFC pathways presented in Sections 5.2 and 5.3 are associated with a system of two coupled phonon modes. In contrast, we now present the experimental observations of four-

wave mixing based PFC in a system of three coupled modes [78]. When tuned to a specific drive condition: $S_{in}\left(\frac{\omega_D}{2\pi} = 3.857\ MHz\right) = 15\ dBm$, the micromechanical resonator has been observed to exhibit PFC via three-mode four-wave mixing. Figure 5.15 shows the frequency spectrum of output electrical signal at this drive condition. As seen in this figure, there are five thick features in the spectral response. The feature 1 is closer to $\frac{\omega_D}{2\pi}$. The features 2 and 3 are however about some arbitrary frequencies ω_m and ω_n. Despite the arbitrariness, their sum $\omega_m + \omega_n$ is closer to ω_D. The frequency locations corresponding to the last two features 4 and 5 are closer to $2\omega_m$ and $2\omega_n$ respectively.

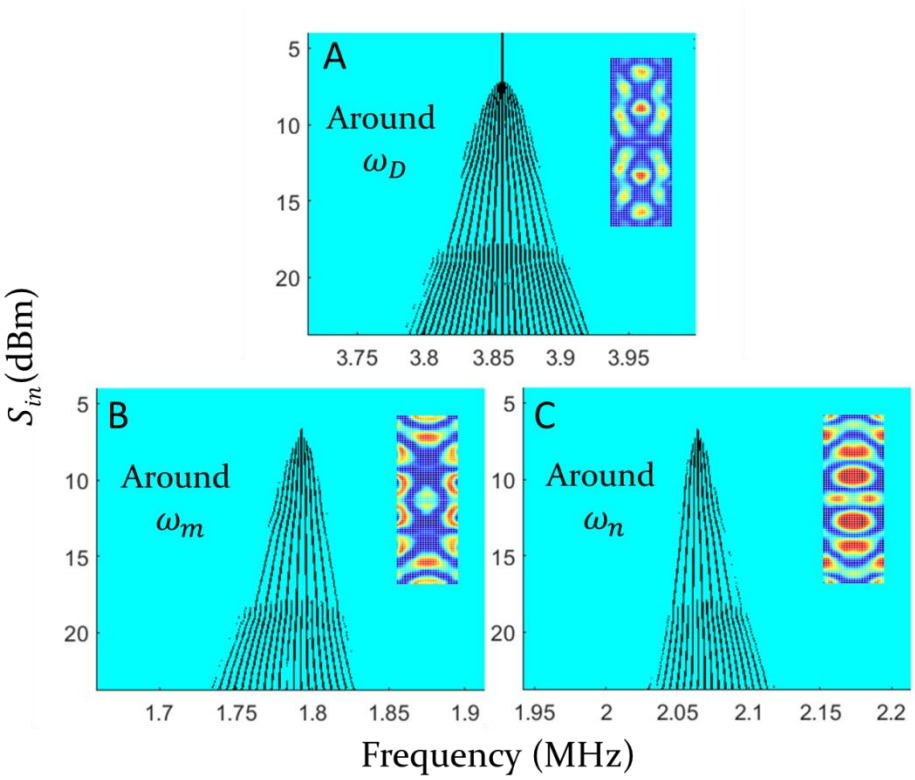

Figure 5.16: **Drive Level Dependence of Frequency Combs.** The S_{out} contours of frequency combs formed around A: ω_D; B: ω_m; C: ω_n respectively for $S_{in}\left(\frac{\omega_D}{2\pi} = 3.857\ MHz\right) = 4 - 23.8\ dBm$. The inset figures show the vibration mode shapes corresponding to the respective frequency combs and the colours red and blue in these figures correspond to maximum and minimum displacements.

To closely visualize these features 1-5, their zoomed-in views are presented in Figures 5.15-(1-5). These views indicate that all of the features 1-5 correspond to PFC of spacing $\Delta\omega =$

5.035 kHz. However, such individual PFC are located closer to 3.857 $MHz = \frac{\omega_D}{2\pi}$, 1.791 $MHz \cong \frac{\omega_m}{2\pi}$, 2.066 $MHz \cong \frac{\omega_n}{2\pi}$, 3.582 $MHz \cong \frac{\omega_m}{\pi}$ and 4.132 $MHz \cong \frac{\omega_n}{\pi}$ respectively. While the spectral line at $\frac{\omega_D}{2\pi}$ corresponds to the drive tone, every other spectral lines are generated through the intrinsic PFC process.

To understand the mechanism underpinning this specific PFC process, we systematically carry out experiments at different values of S_{in} and analyse the PFC located about ω_D, ω_m and ω_n. The inset figures 5.16 A-C indicate that each of the PFC about ω_D, ω_m and ω_n has different characteristic spatial vibration patterns. This suggests that each of those PFC correspond to different phonon modes. In Figure 5.16A, the vertical line corresponds to the constant $\frac{\omega_D}{2\pi}$. While the additional lines about $\frac{\omega_D}{2\pi}$ are equally spaced away at any particular value of S_{in}, $\Delta\omega$ however gets increased with S_{in}. When $S_{in} > 18\ dBm$, we further evidence secondary inter-leaved spectral lines i.e. the spectral lines are formed between the nominal comb lines. Such features were also previously observed in the experimental results of two-mode three-wave mixing (Cyan regions of Figure 5.3).

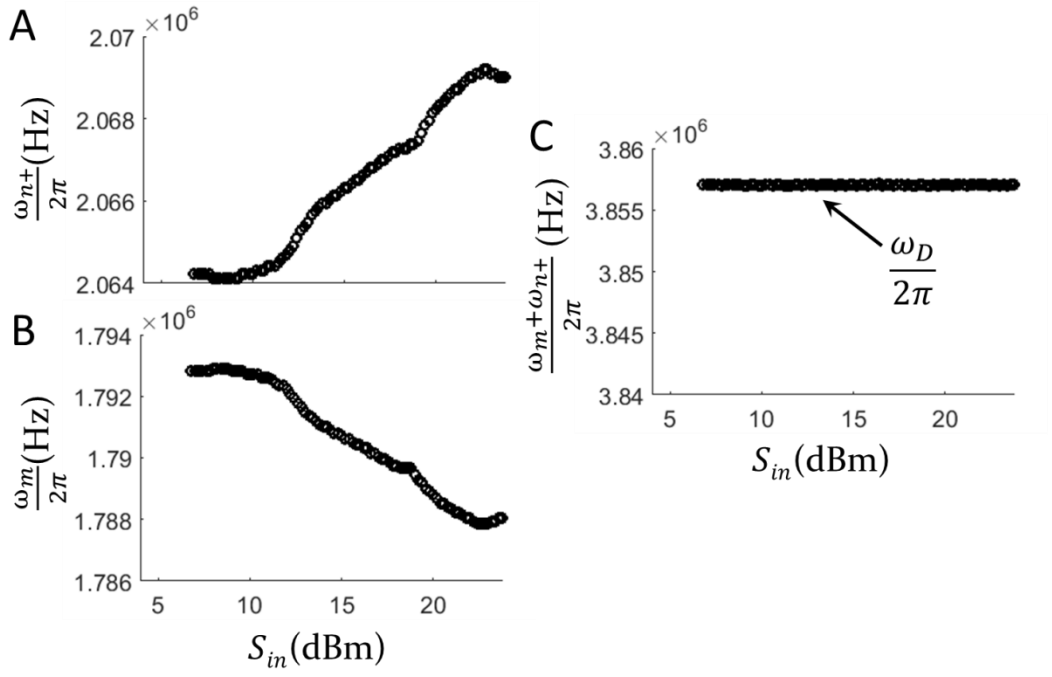

Figure 5.17: **Drive Level Dependence of Frequency Combs (Contd.).** A-C: The drive level S_{in} dependence of $\frac{\omega_{n+}}{2\pi}$, $\frac{\omega_m}{2\pi}$, $\frac{\omega_m+\omega_{n+}}{2\pi}$ respectively. Here again, $S_{in}\left(\frac{\omega_D}{2\pi} = 3.857\ MHz\right) = 4 - 23.8\ dBm$.

In contrast to Figure 5.16A, Figures 5.16B and 5.16C does not feature even a single vertical line. This is due to the S_{in} dependence of both $\omega_{m(n)}$ and $\Delta\omega = |\omega_D - \widetilde{\omega}_i|$. Now, to understand these dependencies further, the trends associated with ω_m and ω_n are examined. Figures 5.17A and 5.17B plot out $\frac{\omega_m}{2\pi}$ and $\frac{\widetilde{\omega}_{n+}}{2\pi} = \frac{1}{2\pi}(\omega_n + \omega_D - \widetilde{\omega}_i)$ for varying S_{in} and these show that ω_m and ω_n are related to S_{in} by peculiar nonlinear functions. Despite such intriguing dependences, $\omega_m + \omega_{n+}$ is always ω_D for any value of S_{in} (Figure 5.17C). Unlike the interesting S_{in} dependency of $\omega_{m(n+)}$, $\Delta\omega$ has a linear relationship with S_{in} (Figure 5.18). This linear dependence of $\Delta\omega$ was also observed in PFC via two-mode three-wave mixing (Figure 5.3). Further, $\Delta\omega$ at any value of S_{in} is same for all of the component combs (Figure 5.18).

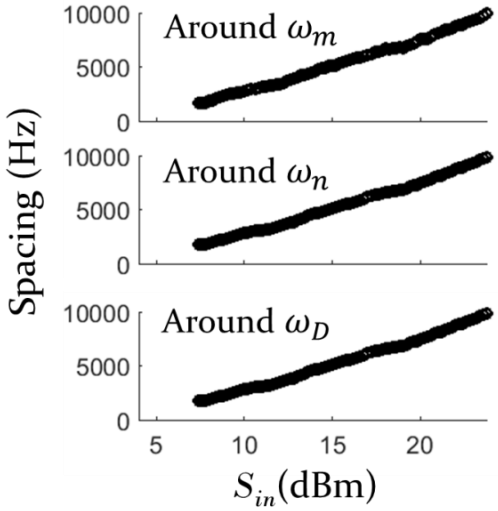

Figure 5.18: **Frequency Comb Spacing.** The spacing of frequency combs formed around ω_m, ω_n and ω_D respectively. Here again, $S_{in}\left(\frac{\omega_D}{2\pi} = 3.857\ MHz\right) = 4 - 23.8\ dBm$.

While the S_{in} dependence is clear, the relevance of $\frac{\omega_D}{2\pi}$ to PFC is now studied. The dotted line in Figure 5.19 shows the S_{in} threshold for the intrinsic excitation of additional phonon modes with frequencies $\frac{\omega_m}{2\pi}$ and $\frac{\omega_{n+}}{2\pi}$. While such an intrinsic process is necessary, it is not sufficient to guarantee PFC formation. In our experiments, the PFC is only formed when $\frac{\omega_D}{2\pi}$ is also set above 3.857 MHz. In other words, to observe PFC, both S_{in} and ω_D should be set to a specific range of values. Further, similar to the two-mode three-wave mixing (Figure 5.5), $\Delta\omega$ further stays constant with $\frac{\omega_D}{2\pi}$ for any particular value of S_{in} which also indicates that the operative PFC is in the 'DNR-Duffing' regime.

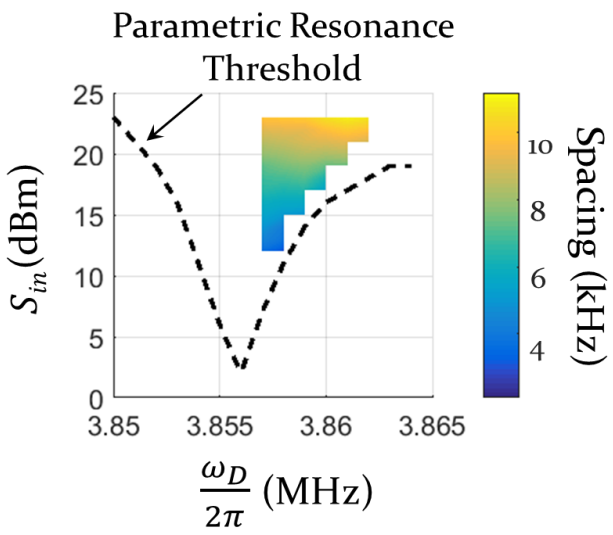

Figure 5.19: **Frequency Comb Spacing (Contd.).** The spacing of frequency combs for $S_{in}\left(\frac{\omega_D}{2\pi} = (3.85\ MHz - 3.865\ MHz)\right) = 4 - 23.8\ dBm$. The absence of colour or white-colour indicates the absence of frequency comb for that drive condition. The dotted black line indicates the parametric resonance threshold. The drive level S_{in} above this threshold line leads to the excitation of $\frac{\omega_m}{2\pi}$ and $\frac{\omega_{n+}}{2\pi}$.

In the penultimate paragraph, we had discussed the nonlinear functional relationship between $\omega_{m(n+)}$ and S_{in}. Further, we had also shown that the PFC is not formed if $\frac{\omega_D}{2\pi} < 3.857\ MHz$. While PFC is absent, at high-enough values of S_{in}, the tones of frequencies ω_m and ω_{n+} continue to get excited even for $\frac{\omega_D}{2\pi} < 3.857\ MHz$. Hence, the comparison between S_{in} dependences of $\omega_{m(n+)}$ corresponding to PFC and non-PFC stages (i.e. $\frac{\omega_D}{2\pi} > 3.857\ MHz$ and $\frac{\omega_D}{2\pi} < 3.857\ MHz$ respectively) can sketch out the correlation of PFC process and nonlinear S_{in} dependency of $\omega_{m(n+)}$ (Figures 5.17A and 5.17B). To this end, we plot ω_m and ω_{n+} for different values of S_{in} and ω_D. Figures 5.20A-C indicate that the simultaneous nonlinear downshifts and upshifts of ω_m and ω_{n+} only occur during the operation of PFC process. Despite such shifts, the condition $\omega_m + \omega_{n+} = \omega_D$ is always satisfied. Yet, $\omega_m - \omega_{n+}$ is ω_D dependent.

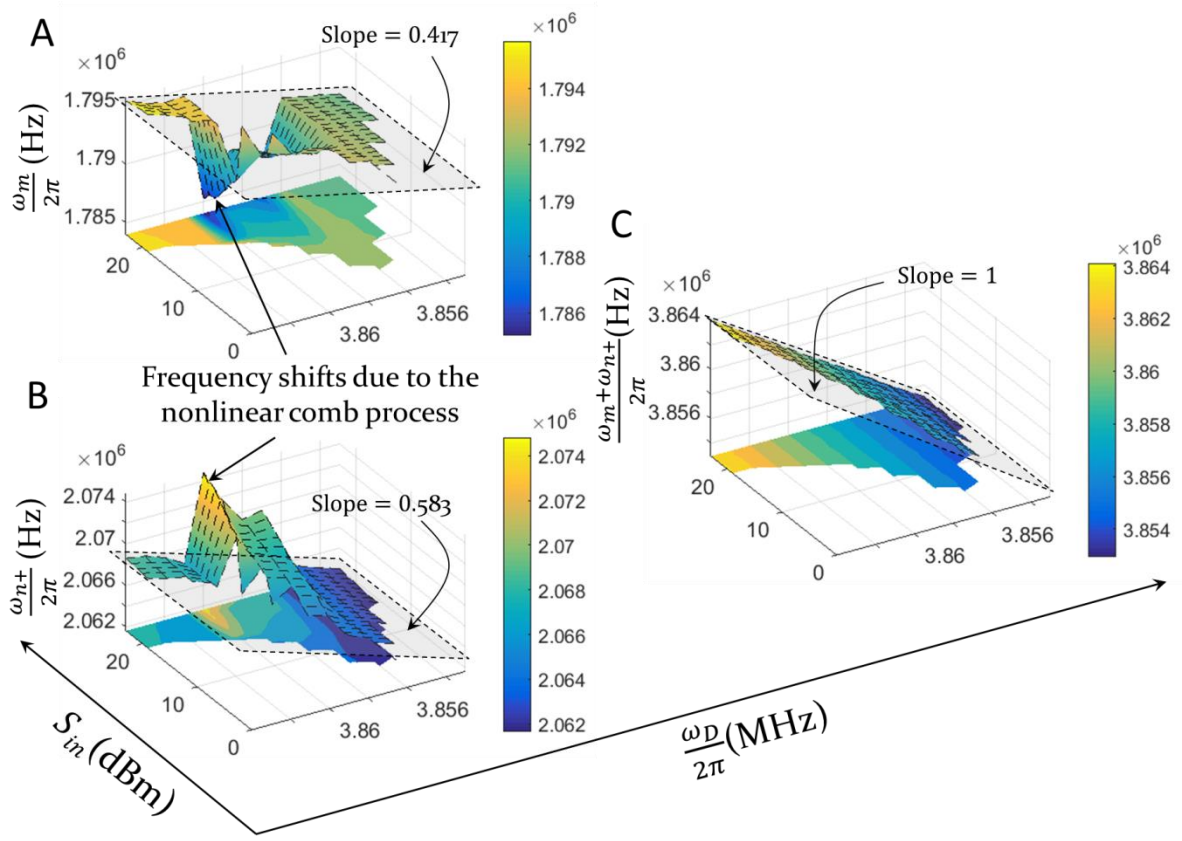

Figure 5.20: **Comb vs. Non-Comb Processes.** A-C: The value of $\frac{\omega_m}{2\pi}$, $\frac{\omega_{n+}}{2\pi}$ and $\frac{\omega_m+\omega_{n+}}{2\pi}$ for different drive frequencies $\frac{\omega_D}{2\pi}$ and drive levels S_{in} respectively. The colour-maps indicate the values of these frequencies. The absence of colour or white-colour indicates the absence of frequency comb for that drive condition. The sketched planes correspond to the nominal $\frac{\omega_D}{2\pi}$ dependence of $\frac{\omega_m}{2\pi}$, $\frac{\omega_{n+}}{2\pi}$ and $\frac{\omega_m+\omega_{n+}}{2\pi}$ i.e. in the absence of three mode four-wave mixing. Note: The projections of 3-D plots on the $S_{in} - \frac{\omega_D}{2\pi}$ plane are also shown for clarity.

5.5. Analytical Formulation of Phononic Frequency Combs

Appendices B-D present the analytical formulation of PFC via two-mode three-wave mixing, two-mode pumped three-wave mixing and three-mode four-wave mixing processes respectively. Here, the Poincare-Lindstedt (PL) method is adapted.

5.6. Steps Ahead for New Explorations

5.6.1. Recap

Until now, in this chapter, we had discussed the experimental observations related to three characteristic PFC pathways.

1. The two-mode three-wave mixing results in PFC that spans two phonon modes. Here, the drive frequency is set within a specific window of the resonant band associated with one phonon mode. Now, if the amplitude associated with this drive is increased above a threshold value, one another phonon mode also gets excited. And, with further increase in the drive amplitude, the PFC is then formed through high-order interactions. The spacing associated with PFC is defined by the separation between the drive frequency and resonant frequency of the driven phonon mode.

2. The two-mode pumped three-wave mixing also produces PFC that spans two phonon modes. However, unlike three-wave mixing, two drive frequencies are involved. These frequencies are set anywhere within the resonant band of one phonon mode. After a characteristic drive level threshold, the PFC is formed through the intrinsic excitation of another phonon mode. The spacing associated with PFC corresponds to the separation between two drive frequencies.

3. The three-mode four-wave mixing, in contrast to the first two cases, results in PFC that span three phonon modes. Here again, similar to two-mode three-wave mixing, the drive frequency is set within a specific window of the resonant band corresponding to one phonon mode. However, when the drive level is increased above the characteristic threshold, two additional phonon modes get excited which in turn results in PFC.

These cases thus show the feasibility of PFC in the realm of micromechanical resonators.

5.6.2. Hypothetical Phononic Frequency Comb Pathways

Despite the existence proofs, the demonstrated PFC pathways merely represent discrete snapshots of a complicated yet unified problem set. However, before getting into the generalization of PFC, we hypothesize a few other PFC pathways.

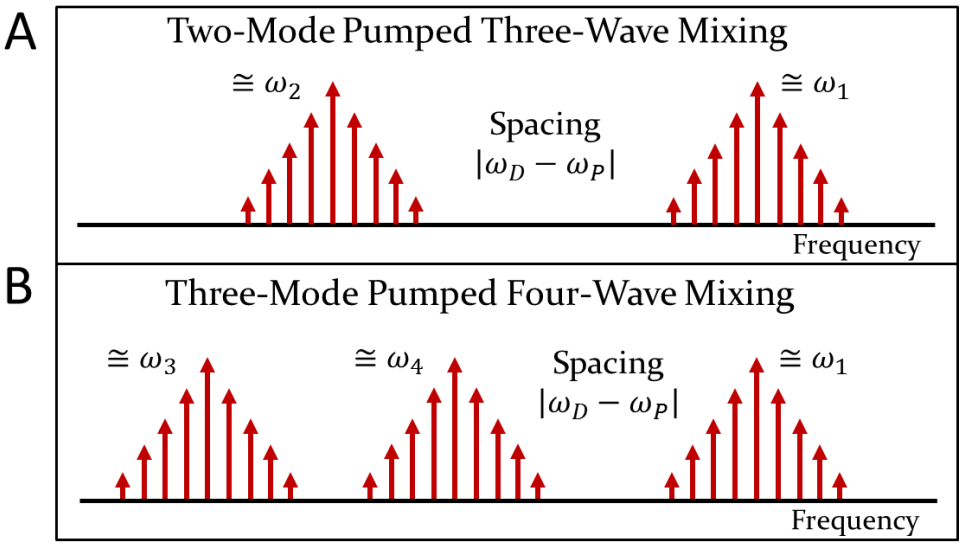

Figure 5.21: A-B: Phononic frequency combs via two-mode pumped three-wave mixing and three-mode pumped four-wave mixing respectively.

- Three-Mode Pumped Four-Wave Mixing: Similar to a threshold dependent two-mode pumped three-wave mixing pathway (Figure 5.21A) in a two phonon mode system, an analogous mechanism may also exist in a three-mode system (Figure 5.21B). Through such a possibility, PFC can emerge about three phonon mode frequencies. Here again, the spacing associated with PFC may also be set by the separation between two drive frequencies.

- $(N+1)$-Wave Mixing and Pumped $(N+1)$-Wave Mixing – Coexistence or Transition: In '$(N+1)$-wave mixing' pathway, a single drive frequency develops into a series of frequencies with an equidistant spacing. On the other hand, in pumped $(N+1)$-wave mixing, two frequencies (corresponding to the drive and pump) develop into a series of frequencies with an equidistant spacing (Figure 5.22B). Now, let us consider the case where one or both of the drive frequencies can independently develop into PFC via

$(N+1)$-wave mixing (Figure 5.22A). In this scenario, there can be two possible routes. 1. The independent $(N+1)$-wave mixing pathways corresponding to each of the drive frequencies and the pumped $(N+1)$-wave mixing pathway between the two drive frequencies may always co-exist (Figure 5.22C). Due to this co-existence, the nature of each component pathways may or may not be altered. 2. There may be distinct bounded regimes associated with each of these pathways with the transitions occuring at the characteristic boundaries.

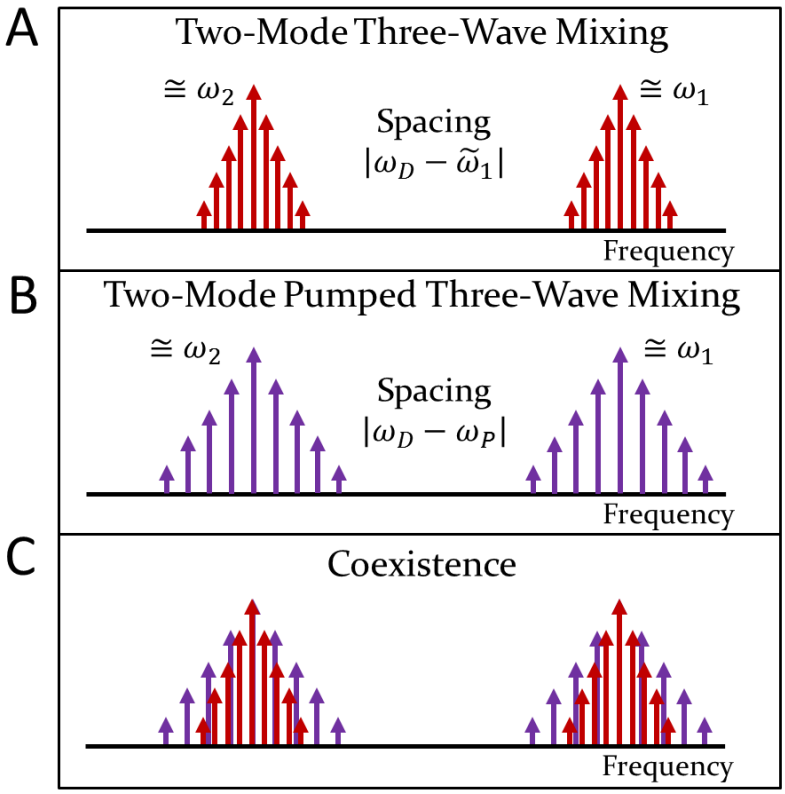

Figure 5.22: A-B: Phononic frequency combs via two-mode three-wave mixing and two-mode pumped three-wave mixing respectively; C: Coexistence of A and B.

- Two-Mode Three-Wave Mixing and Three-Mode Four-Wave Mixing – Coexistence or Transition: In 'two-mode three-wave mixing' pathway, a strongly driven phonon mode intrinsic couples to another phonon mode to produce PFC. On the other hand, in 'three-mode four-wave mixing' pathway, a strongly driven phonon mode intrinsic couples to two additional phonon modes to produce PFC. Let us now consider the case where the driven phonon mode can couple to one another phonon mode through two-mode three-wave

mixing (Figure 5.23A) and can also couple to two different phonon modes through three-mode four-wave mixing (Figure 5.23B). In this situation, there can be two possibilities. 1. Both two-mode three-wave mixing and three-mode four-wave mixing pathways may co-exist (Figure 5.23C). Due to this co-existence, the nature of each component pathways may or may not be altered. 2. There may exist bounded regimes corresponding to two-mode and three-mode four-wave mixing pathways and the transitions may therefore occur at the characteristic boundaries.

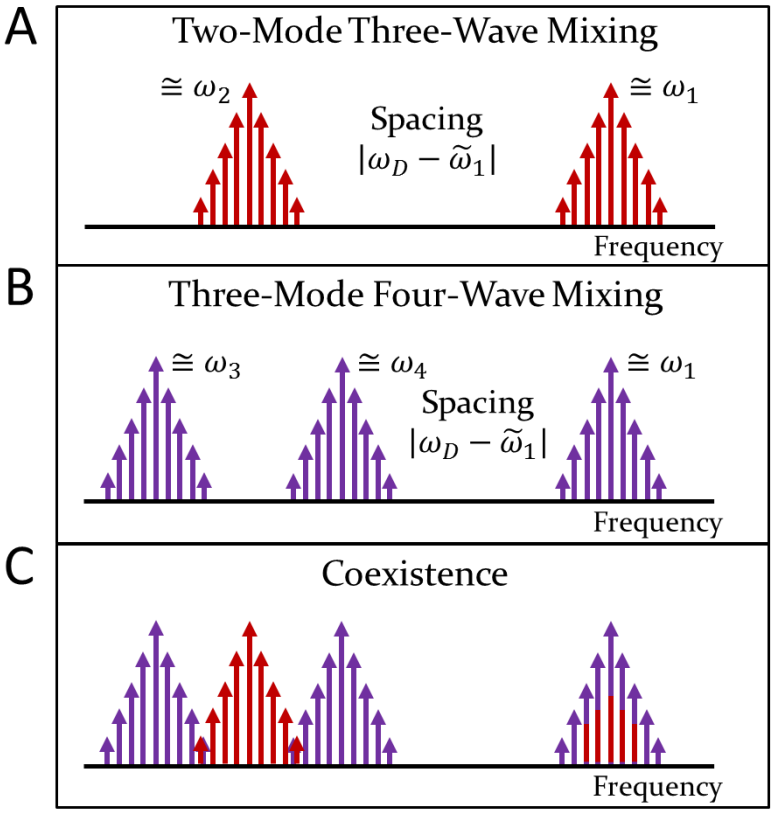

Figure 5.23: A-B: Phononic frequency combs via two-mode three-wave mixing and three-mode four-wave mixing respectively; C: Coexistence of A and B.

- PFC and Other Nonlinear Resonances – Coexistence or Transition: We now know that the PFC can be generated through either $(N+1)$-wave mixing or pumped $(N+1)$-wave mixing pathways in a system of N coupled modes. While the PFC forms one specific nonlinear problem, there exist a wide variety of other nonlinear resonances for instance, PR. Let us now consider a hypothetical situation where there is an equal enough probability for one of the PFC pathways (Figure 5.24B) and a different nonlinear pathway

(Figure 5.24A). Here again, similar to the arguments presented in the previous points, there may be co-existence of each of the possible pathways (Figure 5.24C) or there may be characteristic zones for each of the possible pathways.

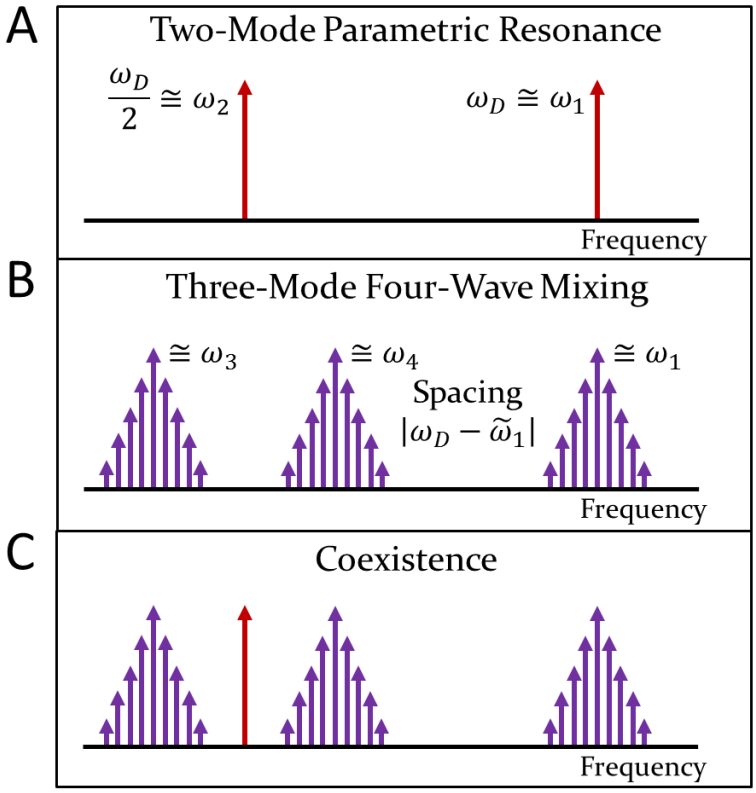

Figure 5.24: A: Two-mode parametric resonance; B: Phononic frequency combs via three-mode four-wave mixing; C: Coexistence of A and B.

- Three-Tone Excitation: In our experiments, we had at most applied two drive frequencies and this specific case of two drive frequencies had revealed the existence of 'two-mode pumped three-wave mixing' pathway. Now, we extend our discussion to a case of 'three-tone excitation' where three drive frequencies are applied. Here, the following pathways are possible. 1. The three independent two-mode three-wave mixing pathways associated with each drive frequency; 2. The three two-mode pumped three-wave mixing pathways associated with each binary permutation of drive frequencies. Now, these six processes may co-exist or these may exist only in their characteristic regimes.

5.6.3. Generalization

In Section 5.6.1, we had listed the experimental observed PFC pathways. Based on these, we had broadly classified PFC into two categories: 1. '$(N+1)$-wave mixing' and 2. 'pumped $(N+1)$-wave mixing'.

Following this first step towards generalization, in Section 5.6.2, we had attempted to predict the possible outcome of slightly advanced experimental scenarios with the help of precursory knowledge related to $(N+1)$-wave mixing and pumped $(N+1)$-wave mixing. Henceforth, we had arrived at a few hypotheses. However, in real experiments, only one of these answers may be true. Hence, a clear understanding about such cases has to be sought. Thereupon, we should be able to predict the behaviour that results when

1. both two-mode three-wave and pumped three-wave mixing processes can simultaneously be operative.
2. both two-mode three-wave mixing and three-mode four-wave mixing processes can simultaneously be operative.
3. both $(N+1)$ -wave and/or pumped $(N+1)$ -wave mixing and different nonlinear mechanism(s) can simultaneously be operative.
4. three drive frequencies are applied.

This higher-level understanding will form the next step towards generalization of the results, and also is precursory for more advanced experimental studies of PFC and for the subsequent steps towards generalization.

Chapter 6

Conclusion

The Microelectromechanical Systems (MEMS) based resonator technology has now enabled high-sensitivity sensors and high-accuracy clocks. During the development of such practical devices, it was quickly discovered that the vibrations of such miniaturized mechanical entities also render access to new physical regimes. It has thus become our vision to utilize the matured MEMS resonator technology for exploring such interesting physical regimes. This thesis entitled, "Phononic Frequency Combs" is one of the initial results of this vision. Here, as the title suggests, the first experimental observations of PFC are recorded and the theoretical basis for the same is discussed.

The established resonant pathways including LR, DP and PR are the salient features of micromechanical resonator. The LR represents a manifestation of the nominal combination of forces including inertial, spring and damping. However, the DP and PR characterise specific deviations from the nominal case of LR and can be included in the broad category of 'nonlinear resonance'. The key feature of DP is the drive amplitude dependent resonant frequency modulation- also typically referred to as 'amplitude-to-frequency effect'. On the other hand, the noticeable aspect of PR is that the drive mode causes self-excitation of other modes through an associated intrinsic coupling.

These distinctive salient features of micromechanical resonator namely LR, DP and PR can be unified using a generalized Fermi-Pasta-Ulam (FPU) framework. This general formalism can not only demonstrate LR, DP and PR but also the new PFC. The numerical prediction of PFC [14] proves this aspect and the drive amplitude and frequency controls portray the underlying physical pathway of PFC.

However, owing to the long computation times, systematic numerical studies of complex FPU phenomena including PFC may not be practically possible. Hence, accessible experimental test-beds are important. The micromechanical resonator, due to the access to multiple modes

with strong modal couplings, ease of their experimental control and their informative experimental characterization, can be extremely useful for the exploration of FPU phenomena.

We have then shown the experimental evidences of PFC in a micromechanical resonator. These evidences include two-mode three-wave mixing (Section 5.2, [13]), two-mode pumped three-wave mixing (Section 5.3, [76-77]) and three-mode four-wave mixing (Section 5.4, [78]) (Figure 6.1).

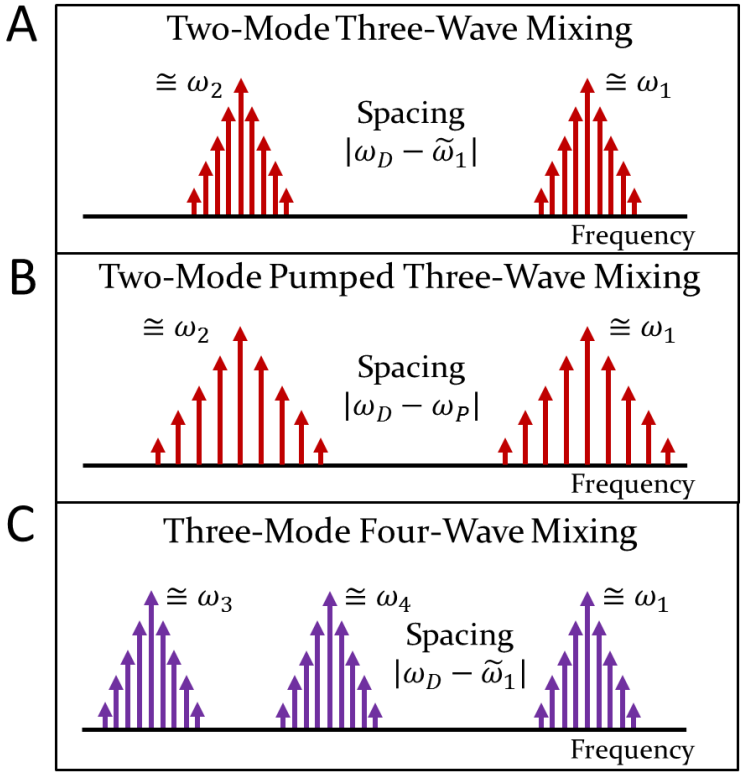

Figure 6.1: A-C: Phononic frequency combs via two-mode three-wave mixing (input frequency: ω_D); two-mode pumped three-wave mixing (input frequencies: ω_D and ω_P); three-mode four-wave mixing (input frequency: ω_D) respectively.

The two-mode three-wave mixing results from the intrinsic coupling among two phonon modes and one drive tone; The two-mode pumped three-wave mixing results from the intrinsic coupling among two phonon modes, drive and pump frequencies; three-mode four-wave mixing results from the intrinsic coupling among three phonon modes and one drive tone. Through these large number of experimental observations, PFC can thus emerge as a new salient feature of micromechanical resonator.

Chapter 7

Future Work

This thesis has presented the initial evidence for PFC in a micromechanical resonator. Hence, there exist a lot of new directions for the development of PFC. In this chapter, we discuss those opportunities under different sections.

7.1. Observation of New Frequency Combs in Micromechanical Resonator

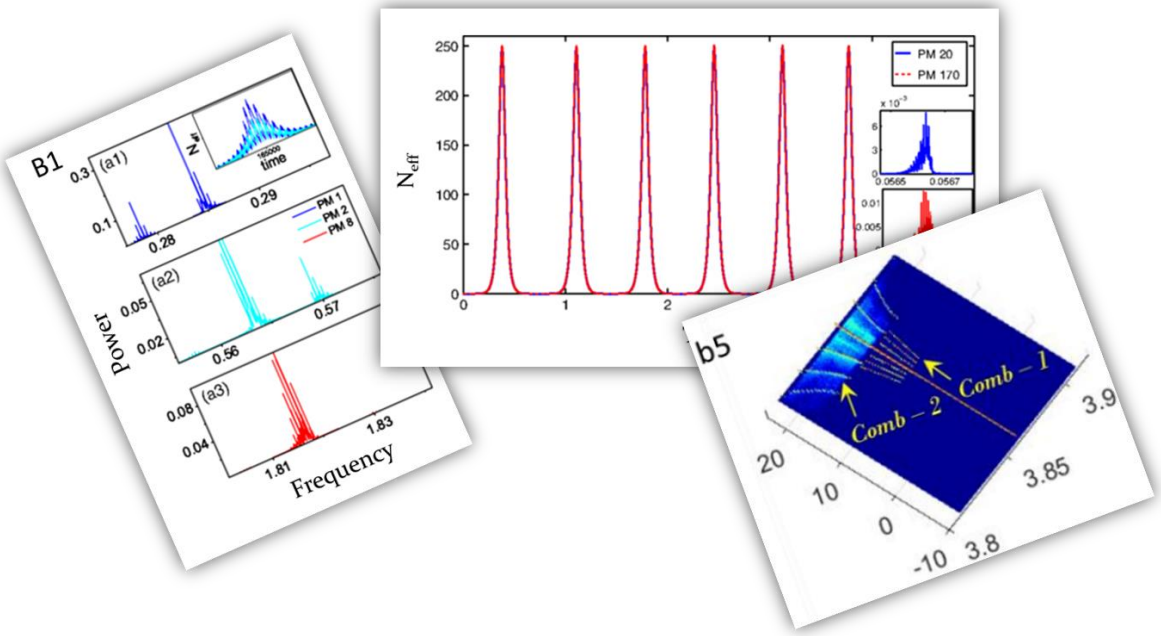

Figure 7.1: **Exploring New forms of Phononic Frequency Combs.** Reprinted figure with permission from [L. S. Cao, D. X. Qi, R. W. Peng, M. Wang, and P. Schmelcher, *Physical review letters,* vol. 112, p. 075505, 2014.] Copyright (2014) by the American Physical Society.

We have shown three representative kinds of PFC viz. 'two-mode three-wave mixing', 'two-mode pumped three-wave mixing' and 'three-mode four-wave mixing'. However, these may not be the only possible pathways for the generation of PFC. There may exist further new

types of PFC. This idea can straightforwardly be validated by the additional numerical evidences of [14] and our follow-on experimental results [79] (Figure 7.1). Hence, it will be an interesting experimental practice to actively research such new observations in micromechanical resonators through logical extension of the initial experimental results of PFC viz. increasing the number of coupling elements [80-84], the number of coupled normal modes [59-62] and the coupling strength [85-86].

7.2. First-Principles Modelling of Phononic Frequency Combs in Micromechanical Resonator

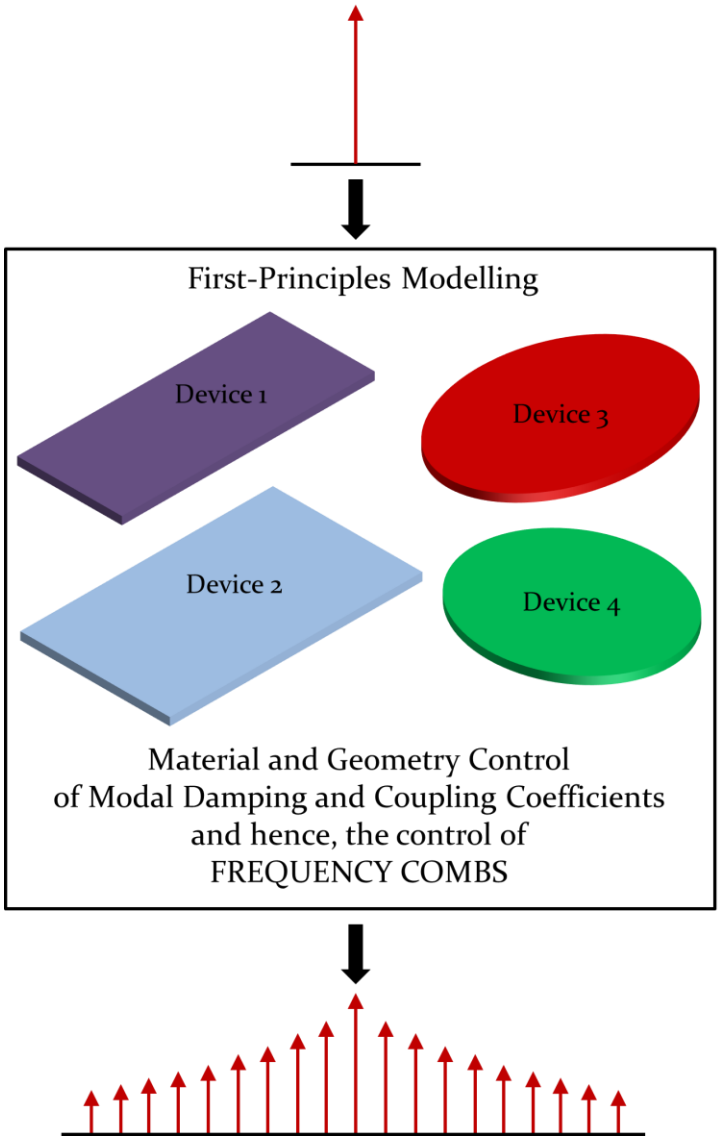

Figure 7.2: **First-Principles Modelling of Micromechanical Frequency Combs.**

While we have presented the conceptual understanding and feasibility of PFC, the real physical (mechanical) nonlinearities which are responsible for its emergence in a micromachined vibratory device should also be extracted through the first-principles modelling approaches including continuum elastic modelling [87-88]. Such studies are important for the predictive engineering of micromechanical frequency combs with high-reproducibility. In addition, the first-principles studies may also reveal the optimization protocols for such frequency combs.

7.3. Observation of New FPU Phenomena in Micromechanical Resonator

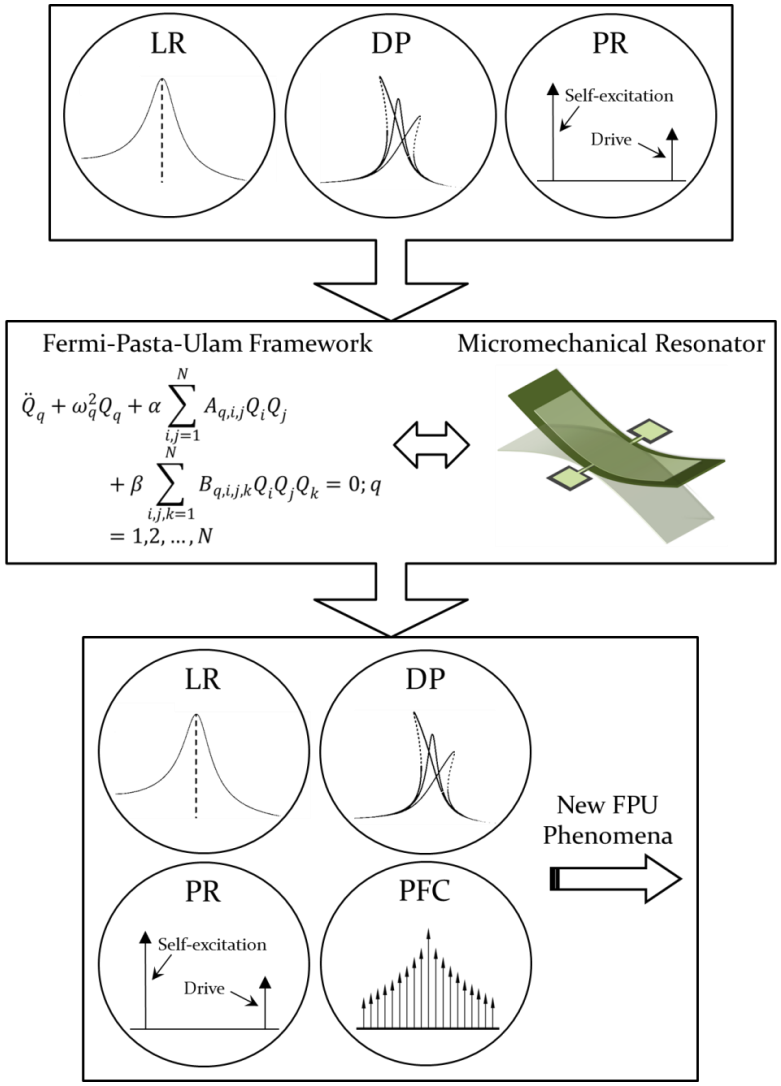

Figure 7.3: **Exploring New FPU Phenomena using Micromechanical Resonators.**

In this thesis, we have shown experimental results demonstrating the formation of PFC in micromechanical resonators. However, multiple unexplored FPU phenomena may also be equally feasible in this physical system. Hence, it will again be interesting to explore such possible mechanisms.

7.4. Mathematical Treatment of Phononic Frequency Combs

The mathematical solution of FPU framework for a single tone drive $P = P_D \cos(\omega_D t)\,; \omega_D \cong \omega_\theta; \theta \in \{1,2,\dots,N\}$ has historically been conceived as follows.

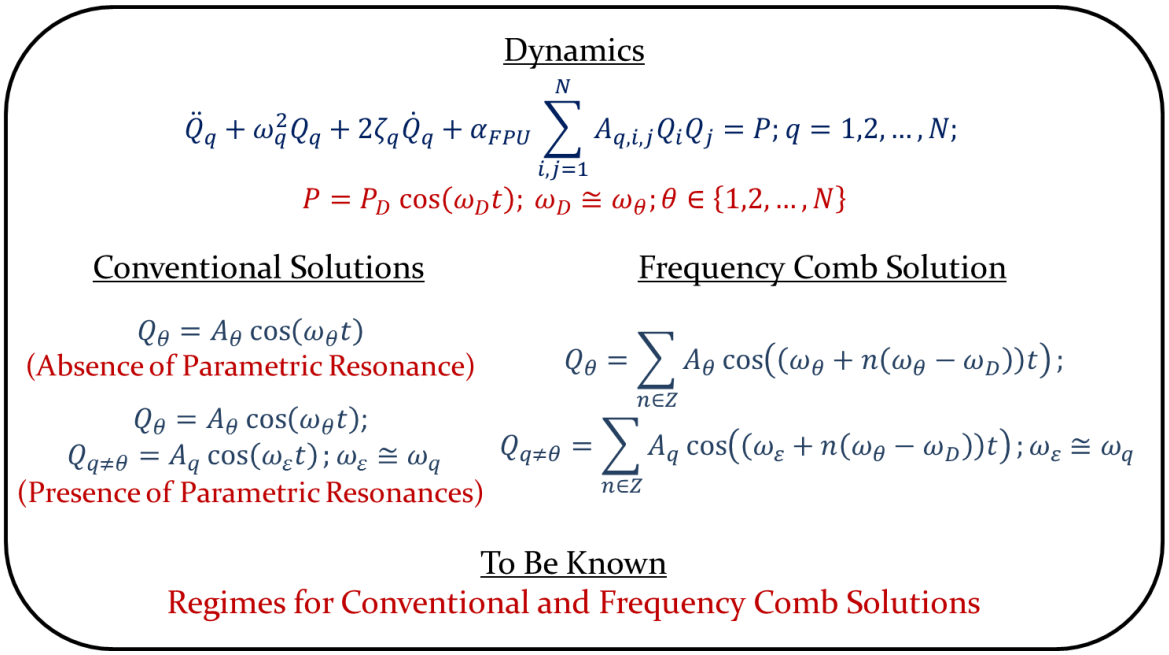

Figure 7.4: **Mathematical Understanding of Frequency Combs.**

In the absence of PR, the displacement of driven mode $Q_{\theta\in q}$ is $A_\theta \cos(\omega_\theta t)\,; \theta \in q$. However, in the presence of PR, the other coupled modes may also get excited and their motion can be captured as $A_q \cos(\omega_\varepsilon t)\,; \omega_\varepsilon \cong \omega_q$ (Section 2.3). The displacement amplitudes A_q are however dependent on the specific system parameters including $\omega_q, \zeta_q, \alpha_{FPU}, A_{q,i,j}, P_D \& \omega_D$.

Now, the experiments of [13, 78] and numericals of [14] had shown the possibility to obtain an alternative solution of 'frequency combs'. The modal displacement corresponding to this solution is

$$Q_\theta = \sum_{n\in Z} A_\theta \cos\Big(\big(\omega_\theta + n(\omega_\theta - \omega_D)\big)t\Big)$$
$$Q_{q\neq\theta} = \sum_{n\in Z} A_q \cos\Big(\big(\omega_\varepsilon + n(\omega_\theta - \omega_D)\big)t\Big);\ \omega_\varepsilon \cong \omega_q \tag{8.1}$$

Hence, fundamentally, we have two possible solutions for the same dynamics (Figure 7.4). This also means that the motion of a physical device which is engineered with a specific set of physical parameters $\omega_q, \zeta_q, \alpha, A_{q,i,j}$ can either be described by the standard solutions or our new solution of frequency combs (Figure 7.4). However, physically, only one of these solutions might actually materialize. Hence, rigorous mathematical efforts [89-92] are warranted to chart out the regimes specific to each of such patterns similar to the previous experimental [13, 78] and numerical [14] efforts.

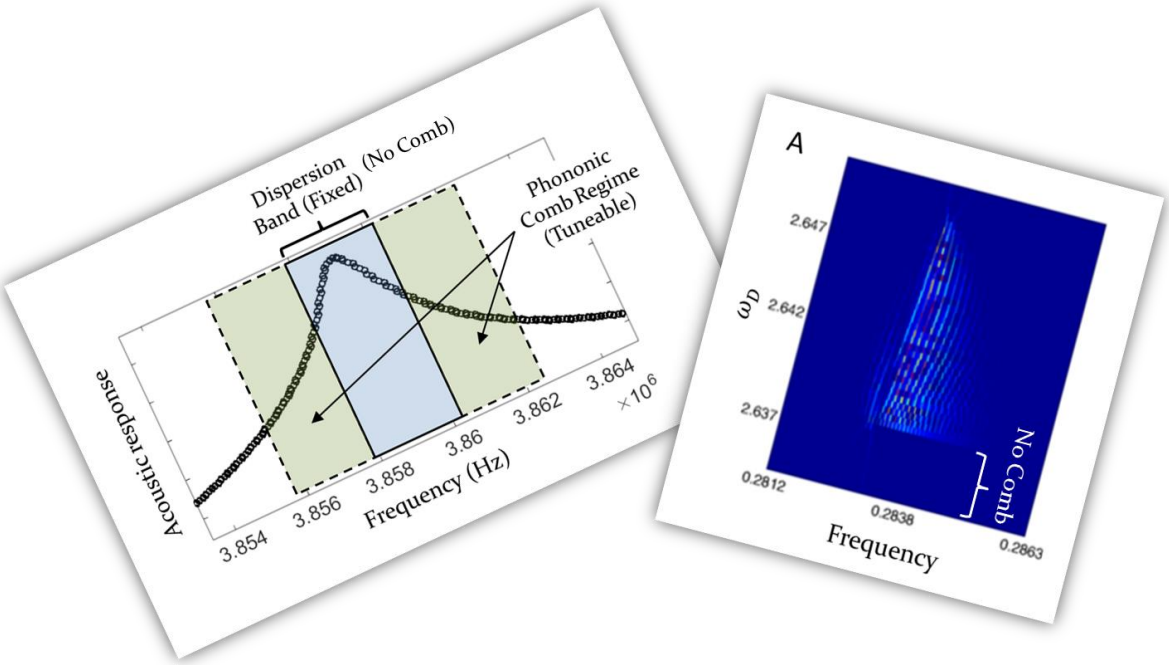

Figure 7.5: **Experimental and Numerical Mapping of Frequency Combs.** Reprinted figure with permission from [L. S. Cao, D. X. Qi, R. W. Peng, M. Wang, and P. Schmelcher, *Physical review letters,* vol. 112, p. 075505, 2014.] Copyright (2014) by the American Physical Society.

7.5. Micromechanical Resonant Frequency Tracking: A Key Application of Phononic Frequency Combs

The PFC is composed of spectral lines $(\omega_\theta + n(\omega_\theta - \omega_D)); (\omega_\varepsilon + n(\omega_\theta - \omega_D))$. If $A_{q\neq\theta} \ll A_\theta$, then the total motion of micromechanical resonator can be approximated to $\sum_{n\in Z} A_\theta \cos\left((\omega_\theta + n(\omega_\theta - \omega_D))t\right)$. While this represents a series of equidistant frequencies, the corresponding temporal signature is a train of periodic pulses which are mode-locked to the modal frequency ω_θ. In other words, we obtain an amplitude modulated sinusoidal wave of frequency ω_θ (Figure 7.6).

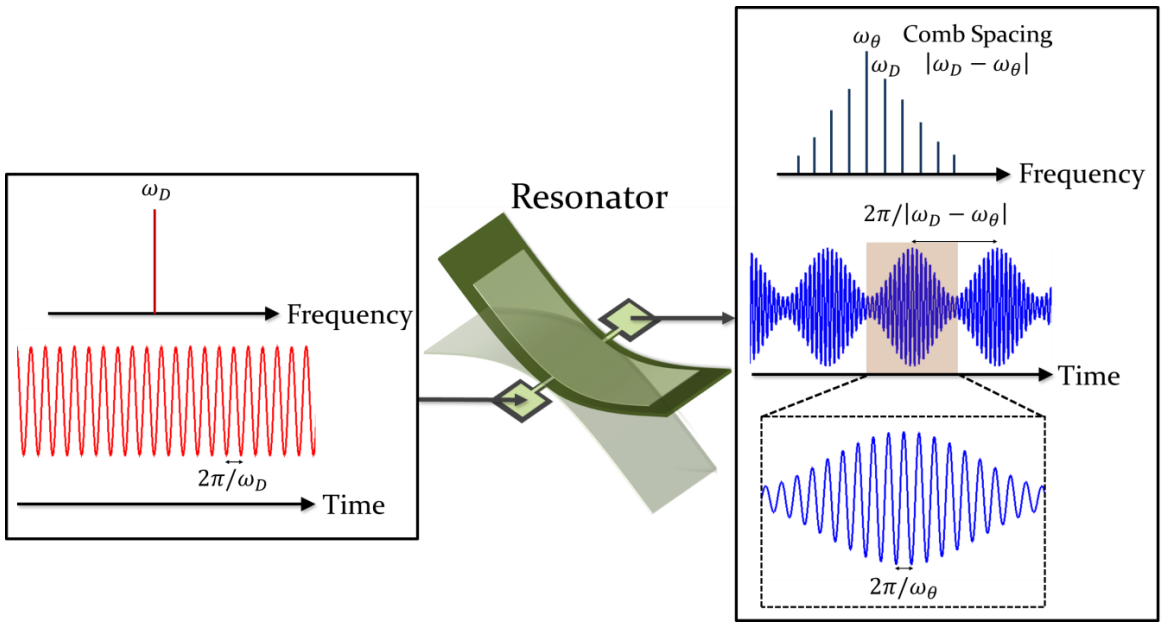

Figure 7.6: **Spectral and Temporal Manifestation of Phononic Frequency Combs.**

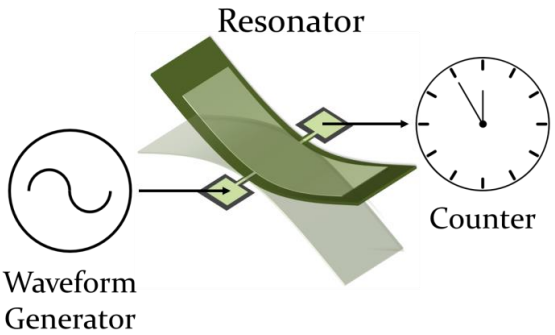

Figure 7.7: **Phononic Frequency Combs based Micromechanical Resonant Tracking.**

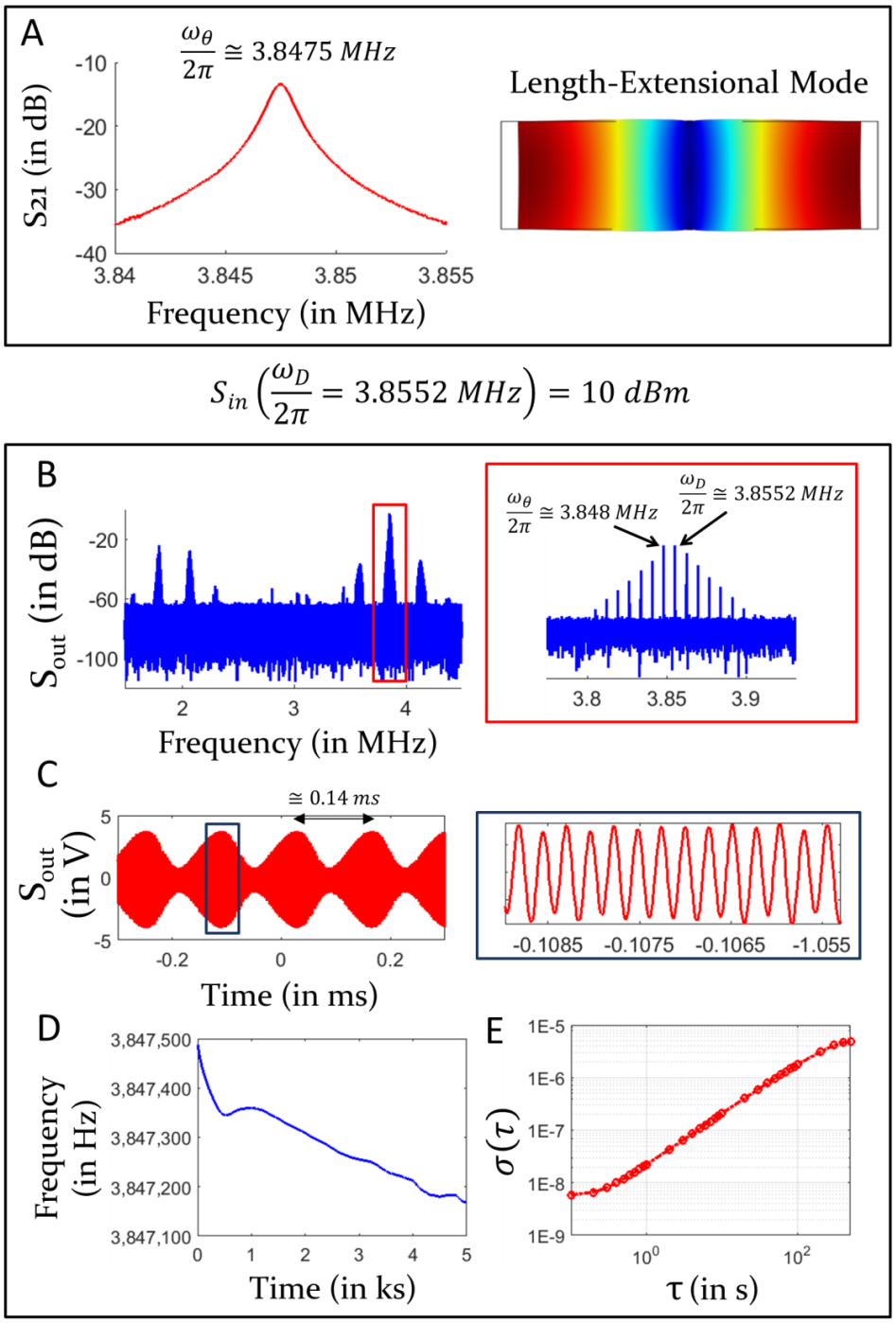

Figure 7.8: **First Experimental Demonstration of Resonant Tracking utilizing Phononic Frequency Combs.** A: The resonant response of length-extensional mode associated with the micromechanical resonator. B: The frequency spectrum and C: waveform corresponding to the output signal for the drive condition $S_{in}\left(\frac{\omega_D}{2\pi} = 3.8552\ MHz\right) = 10\ dBm$; D: The temporal evolution of self-excited resonant frequency (ω_θ) and E: the Allan Deviation $\sigma(\tau)$ of frequency counts.

While the signal of frequency $\omega_D \cong \omega_\theta$ which is synthesized by the waveform generator is fed into the micromechanical resonator (Figure 7.8), the output corresponds to a sinusoidal wave of frequency ω_θ. Now, to track micromechanical resonance frequency ω_θ, the output has to be simply probed using a frequency counter (Figure 7.8). Such an approach to resonant frequency tracking can be harnessed for timing [93-94] and sensing [95-106] applications. Figure 7.9 presents the experimental demonstration of this PFC based resonant tracking. Here, the evolution of resonant frequency (Figure 7.8A) associated with the length-extensional mode of micromechanical resonator is tracked (Figure 7.8D) using the frequency counter (Agilent 53220A) through the generation of PFC (Figures 7.8B and 7.8C)).

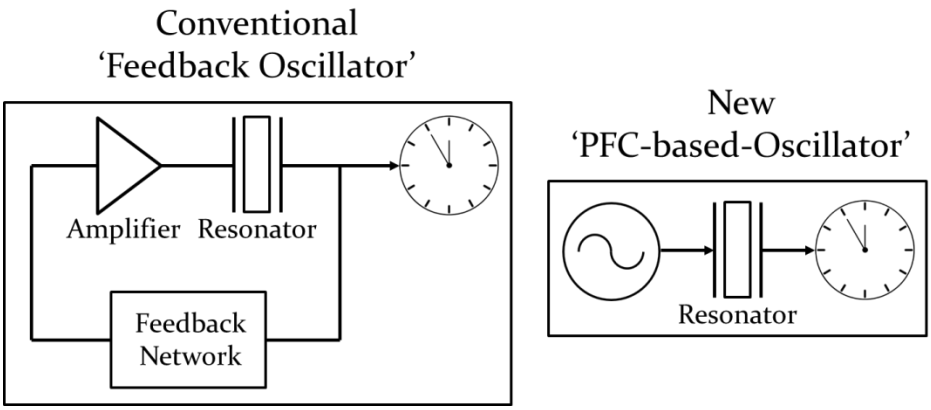

Figure 7.9: **Feedback Oscillator vs. Phononic Frequency Combs based Oscillator.**

The PFC based resonant tracking, unlike feedback oscillator-based approach [65, 67, 107-108], does not require an external electronic amplifier connected up in a feedback configuration (Figure 7.9). Hence, this new approach not only removes the additional design overhead associated with the amplifier but also eliminates associated electronic noise sources and the undesired dynamical electronic noise interactions with resonator dynamics [109-110]. As a result, high-stable measurements of resonant frequency can be achieved (Figure 7.8E). In addition to the stochastic fluctuations, Figure 7.8D also reveals the drift of resonant frequency with time. The physical origins of such drift can be either dynamical PFC process or ambient changes. While the PFC induced drift may reveal a new possibility to control the resonant frequency and its associated fluctuations, the ambience induced drift can be directly relevant to sensing applications. Hence, further investigations of PFC based resonant tracking are warranted for both fundamental understanding and its application in timing and sensing.

The PFC based resonant tracking approach may also in general be applicable to a number of other physical oscillators for instance, atomic clocks and may potentially be more useful than the standard feedback oscillator configuration [107-108].

7.6. Inspiring other Experimentalists

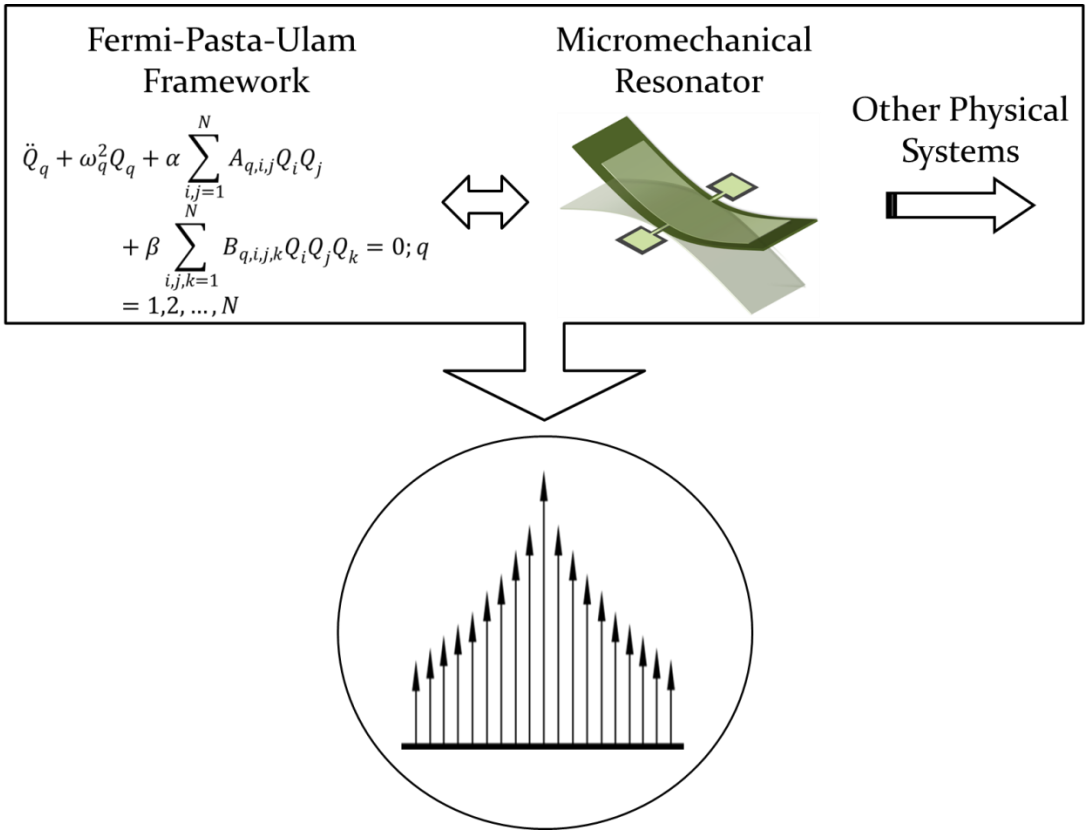

Figure 7.10: **Realization of Frequency Combs in Other Physical Systems.**

Up till now, the specific pathways associated with PFC have been evidenced in the numerical simulations of PFC chains [14] and experimental characterization of micromechanical resonator [13]. In this manner, a theoretical to experimental leap has already been achieved. However, the micromechanical resonator might not be the only physical system that exhibits such novel frequency comb pathways. Owing to the observations of other FPU phenomena (for instance, PR [43-52, 63-64]) in disparate physical systems, the reported frequency comb processes [13, 76-79] may also possibly emerge in such systems (Figure 7.10). In addition, the frequency combs may also appear in other mechanical systems including nanomechanics [111], optomechanics [112] and granular matter [113]. Hence, an active search for the systematic

observations of frequency combs in these experimental systems may be warranted. Meanwhile, using the first experimental venue of micromechanical resonator, we are interested in systematically charting out a wide-range of new concepts pertaining to frequency combs. Such systematic evaluation of frequency combs will serve as a guideline for other experimentalists who are motivated towards the realization of frequency combs in their physical systems.

Appendix A

Fabrication of Micromechanical Resonator by PiezoMUMPs Process

A.1. SOI Substrate

A n-type double-side polished silicon-on-insulator (SOI) wafer (Figure A.1) is the substrate for the PiezoMUMPs process. Its diameter and orientation are 150 mm and (100) respectively. The component layers of SOI wafer are as follows.

1. Top: Silicon layer of thickness: 10 ± 1 µm
2. Middle: Oxide layer of thickness: 1 ± 0.05 µm
3. Bottom: Substrate of thickness: 400 ± 5 µm

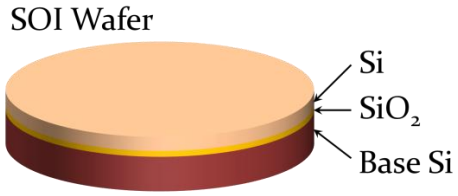

Figure A.1: **Schematic of SOI Wafer.**

A.2. Silicon Doping

A phosphosilicate glass (PSG) layer is deposited on top of the SOI substrate (Figure A.2A). Following this precursory step, the 'Silicon doping' is carried out. For this purpose, the SOI substrate is annealed at 1050°C for 1 hour in Argon (Figures A.2B and A.2C). Once the Silicon is doped through this annealing process, the previously deposited PSG layer is removed via wet chemical etching (Figure A.2D).

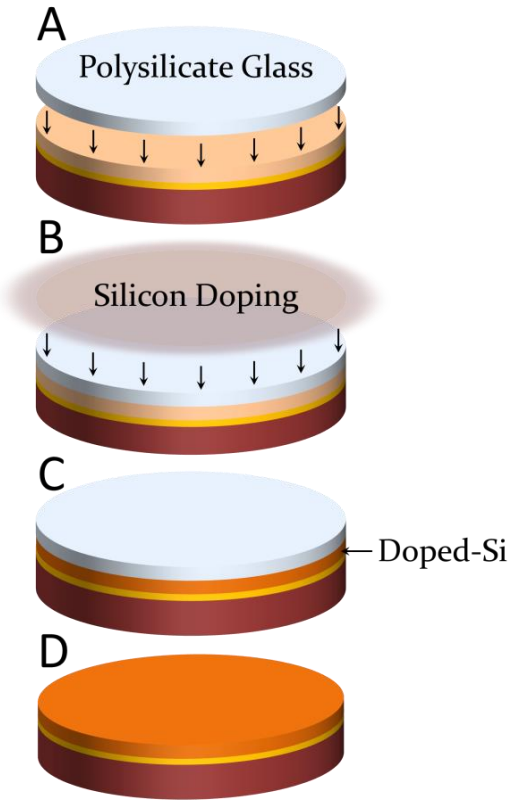

Figure A.2: **Silicon Doping.**

A.3. Growth of Thermal Oxide

A 2000 Å thermal oxide is grown on top of the doped SOI substrate (Figure A.3A). Now, the PADOXIDE mask (Figure A.3C) defines the area where the thermal oxide layer should be removed. Hence, for this patterning process, we first coat the doped SOI wafer with positive photoresist (Figure A.3B) and then expose this photoresist layer with light coming through the PADOXIDE mask (Figure A.3C). In this manner, the patterns associated with the PADOXIDE mask are lithographically transferred to the photoresist (Figure A.3C). Once the light-exposed regions of photoresist are removed, the oxide layer beneath the photoresist becomes unprotected. Hence, the oxide layer corresponding to these regions is removed by wet etching and acid resist strip. We will thus be left with the required oxide patterns on the SOI substrate (Figure A.3D).

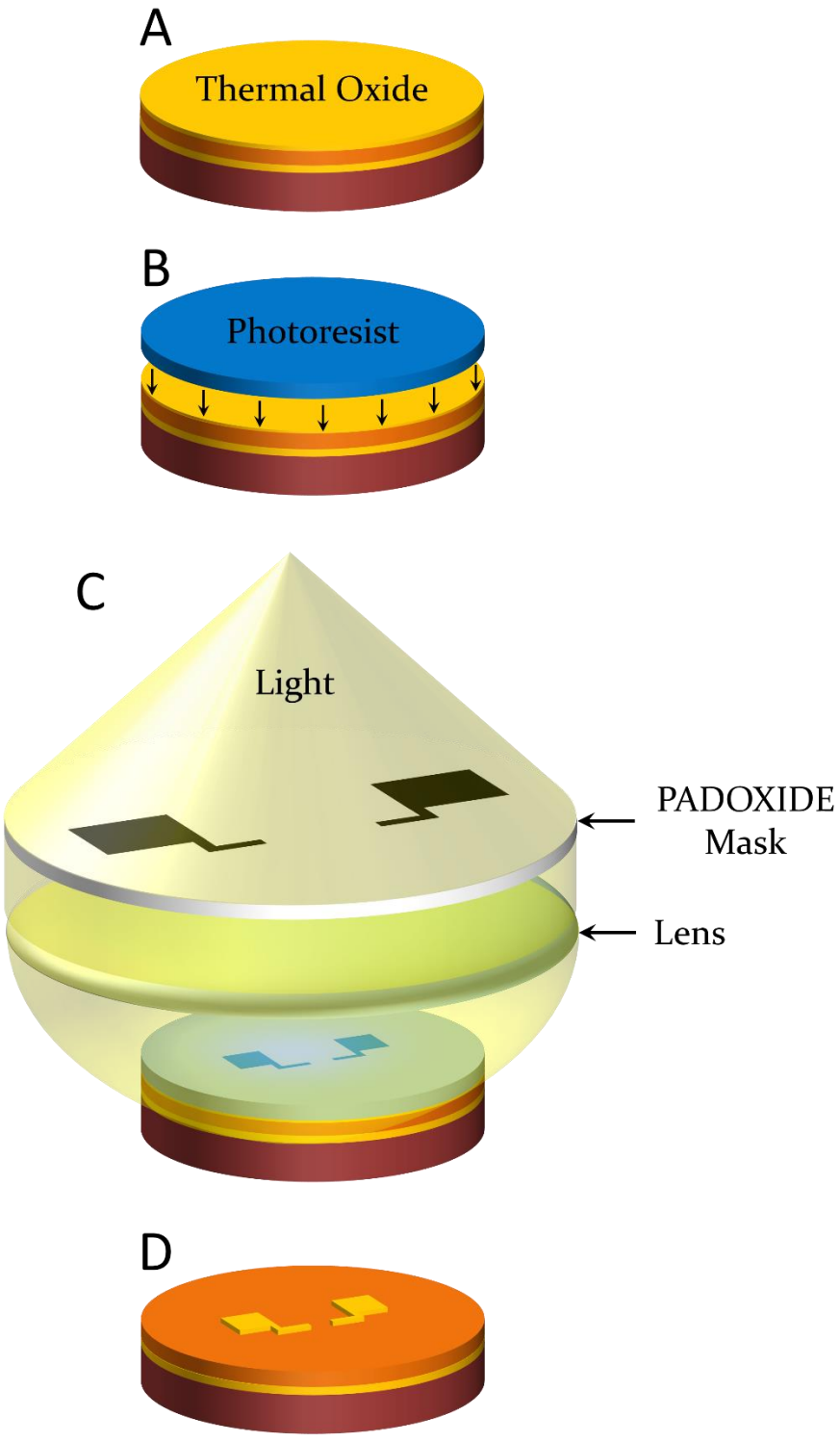

Figure A.3: **Thermal Oxide Growth.**

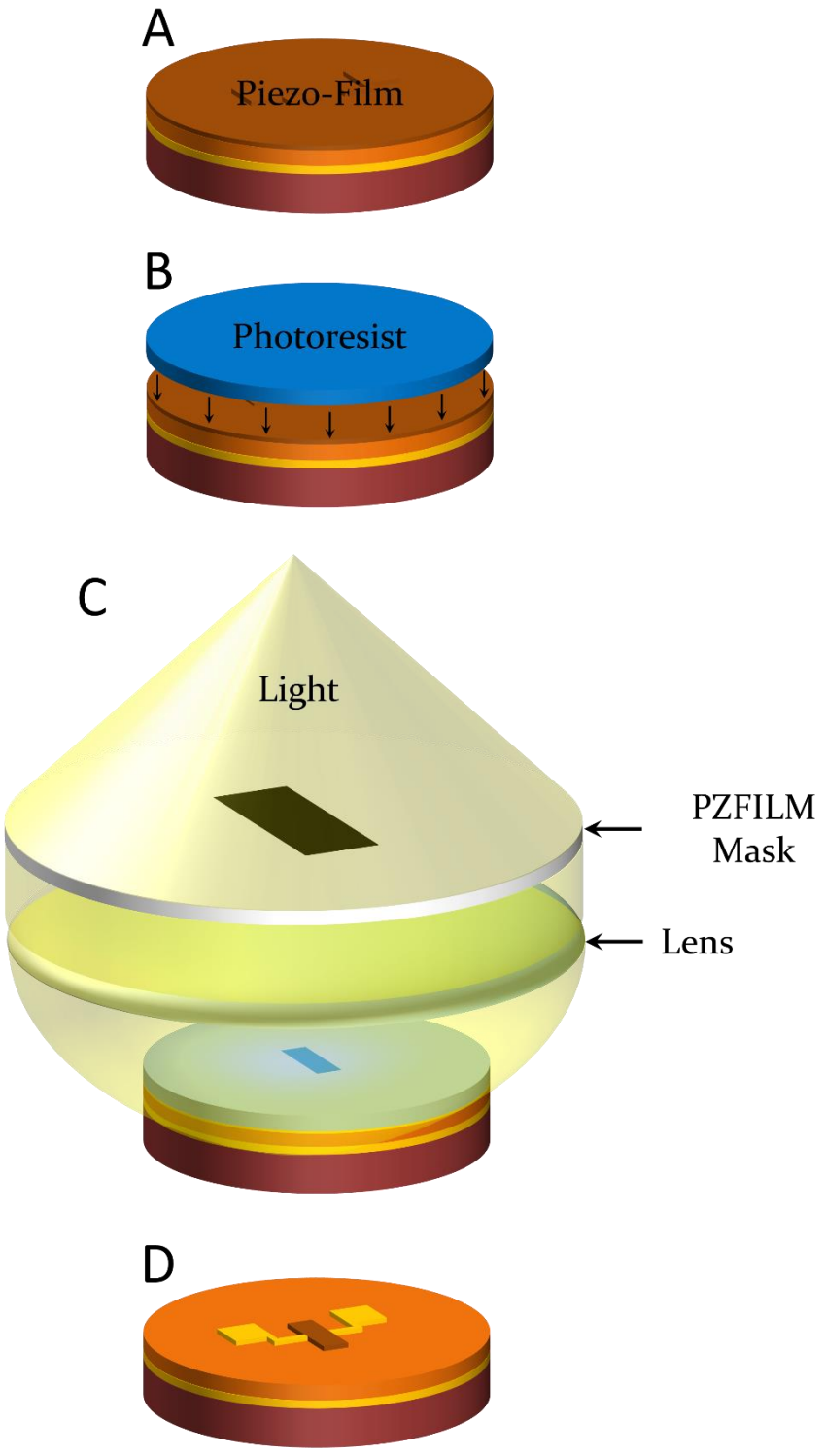

Figure A.4: **Piezoelectric Film Liftoff.**

A.4. Piezoelectric Film Liftoff

Aluminium Nitride (AlN) forms the functional component of our piezoelectric micromechanical resonator. The piezoelectric strain coefficient d33 of AlN is around $3.4 - 6.5\ pC/N$ [74]. First, we deposit a 0.5 μm thick AlN film on the processed SOI substrate (i.e. after SOI doping and thermal oxide growth) by reactive sputtering (Figure A.4A). Now, similar to the thermal oxide patterning process, the AlN film is also lithographically patterned using a PZFILM mask (Figures A.4B and A.4C). Hence, we will also be left with the AlN patterns on the SOI substrate along with the prior thermal oxide patterns (Figure A.4D).

A.5. Pad Metal Liftoff

Here, 20 nm thick Chromium and 1 μm thick Aluminium layers are deposited at first (Figure A.5A). The Chromium forms the intermediate adhesion layer connecting Aluminium with Silicon. Again, similar to the previous liftoff processes, these metal layers are also lithographically patterned (Figures A.5B and A.5C). However, a PADMETAL mask is used for this purpose. Hence, the Al patterns are formed on the SOI substrate (Figure A.5D).

A.6. Silicon Patterning

The SOI wafer is coated with the UV-sensitive photoresist (Figure A.6A). The photoresist is then patterned by exposing it to UV light coming through the SOI mask. The exposed sections of photoresist are then removed (Figure A.6B). Now, the unprotected oxide layer which is present underneath is cut off through Reactive Ion Etching (RIE). The Silicon is then etched down to the buried oxide layer of SOI substrate through Deep Reactive Ion Etching (DRIE) (Figure A.6C). This DRIE process is carried out through Inductively Coupled Plasma (ICP) technology and a special SOI recipe is utilized to avoid undercutting of Silicon once the Buried Oxide is reached during DRIE [74]. Once the SOI is patterned, the photoresist is then stripped-off.

A.6. Polyimide Coat

Prior to substrate patterning, the front side of SOI wafer bearing the Si, Al and AlN patterns should be protected. Hence, a polyimide layer is applied on the top surface of this side of the wafer (Figure A.7).

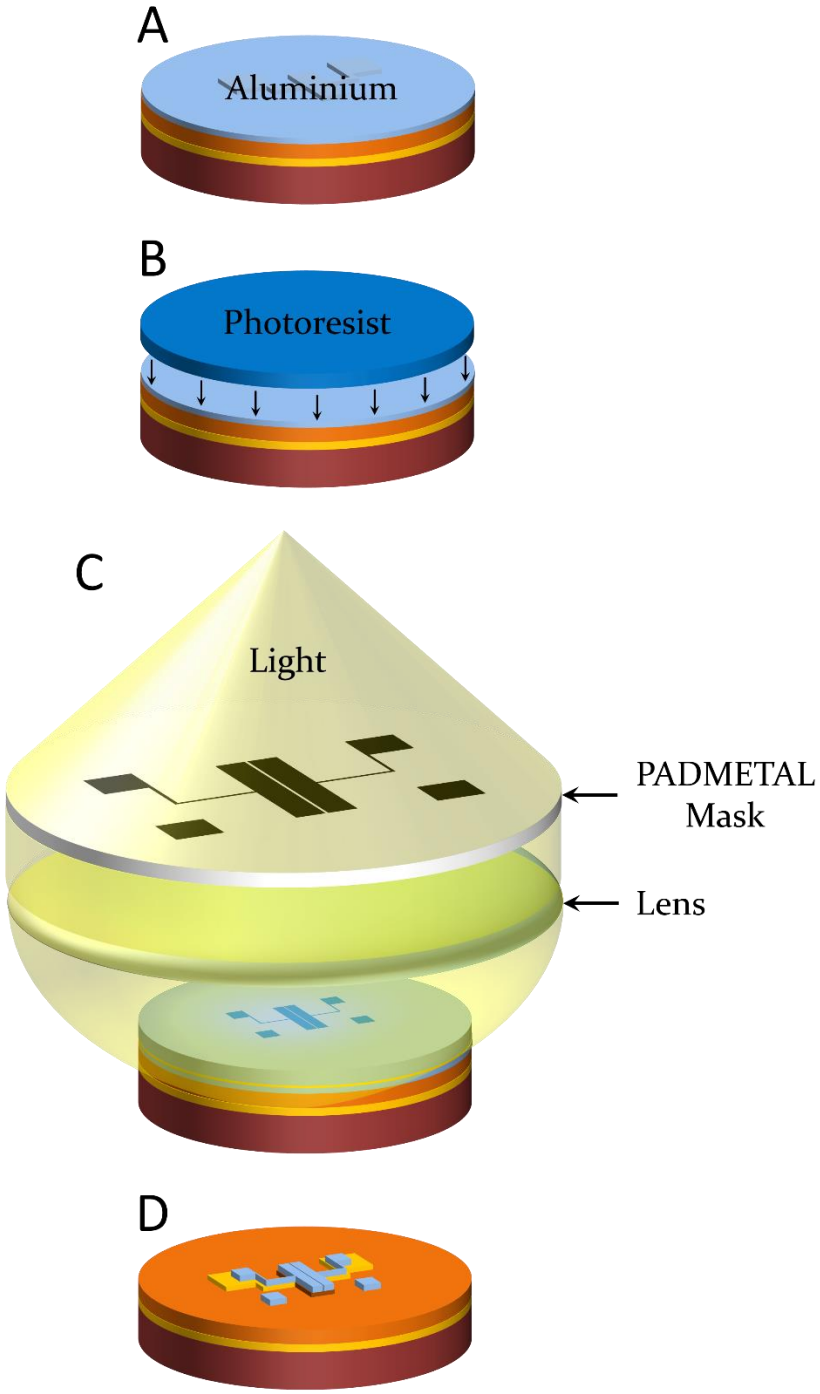

Figure A.5: **Pad Metal Liftoff.**

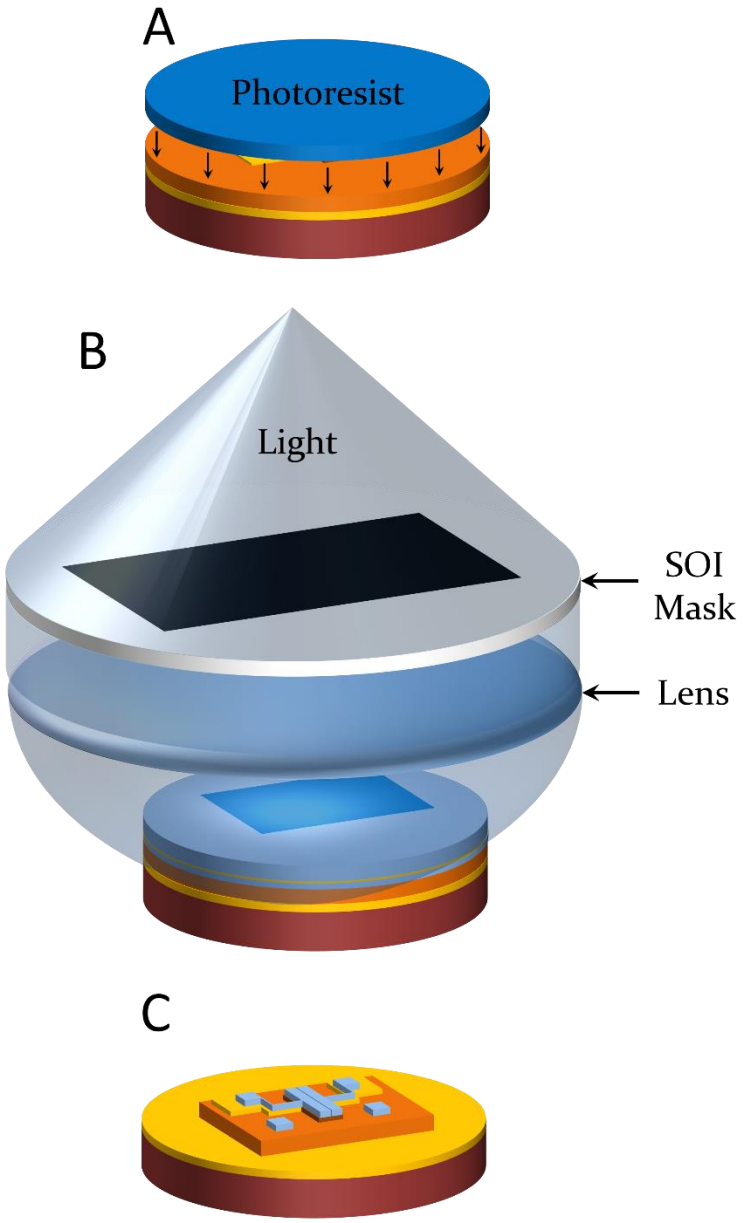

Figure A.6: **Silicon Patterning.**

A.8. Substrate Patterning

Now, the SOI wafer is reversed. The top surface of bottom side is coated with photoresist and is subsequently patterned through the TRENCH mask (Figures A.8A and A.8B). The bottom side oxide layer and substrate Silicon layer (down to the buried oxide layer) are removed through RIE and DRIE respectively. After these etching processes, the buried oxide gets

exposed in the regions defined by the TRENCH mask. Now, this unprotected oxide layer is removed through wet-etching. Hence, we obtain the backside trenches (Figure A.8C).

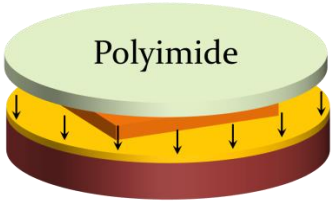

Figure A.7: **Polyimide Coating.**

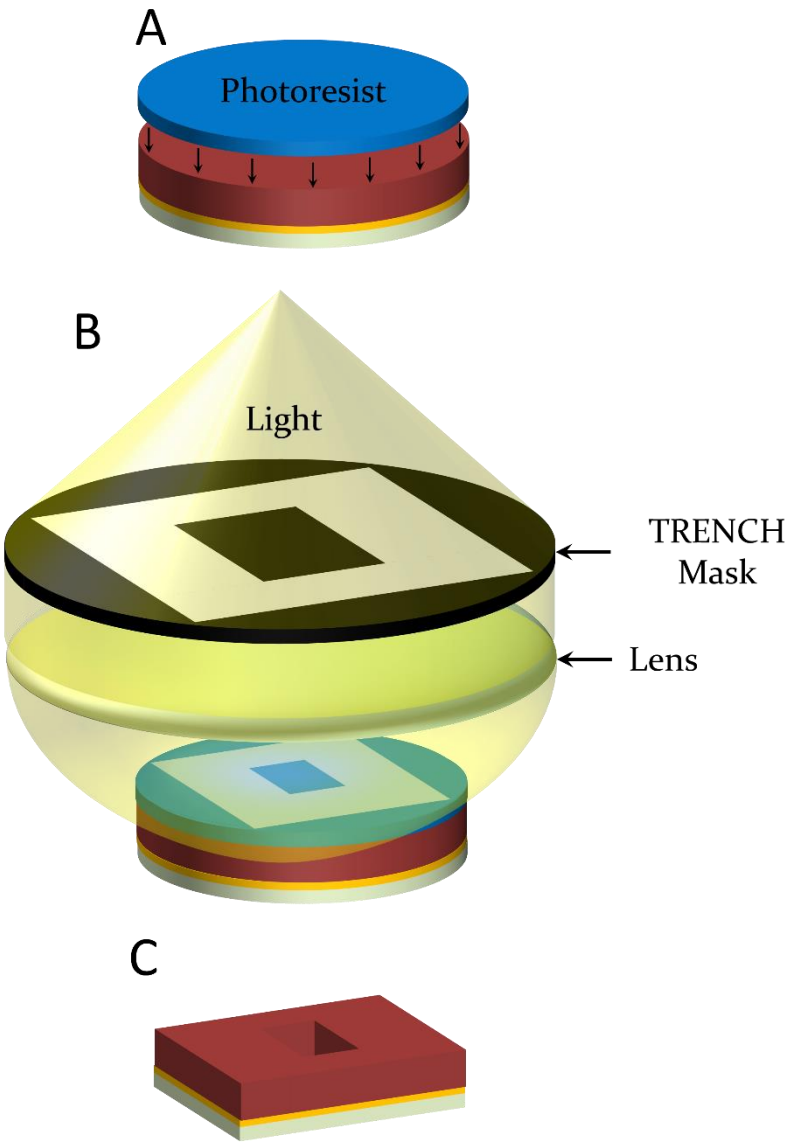

Figure A.8: **Substrate Patterning.**

A.9. Polyimide Removal

The front side protection material is now removed using a dry etching process.

Thus, the piezoelectric micromechanical resonator is fabricated (Figure A.9).

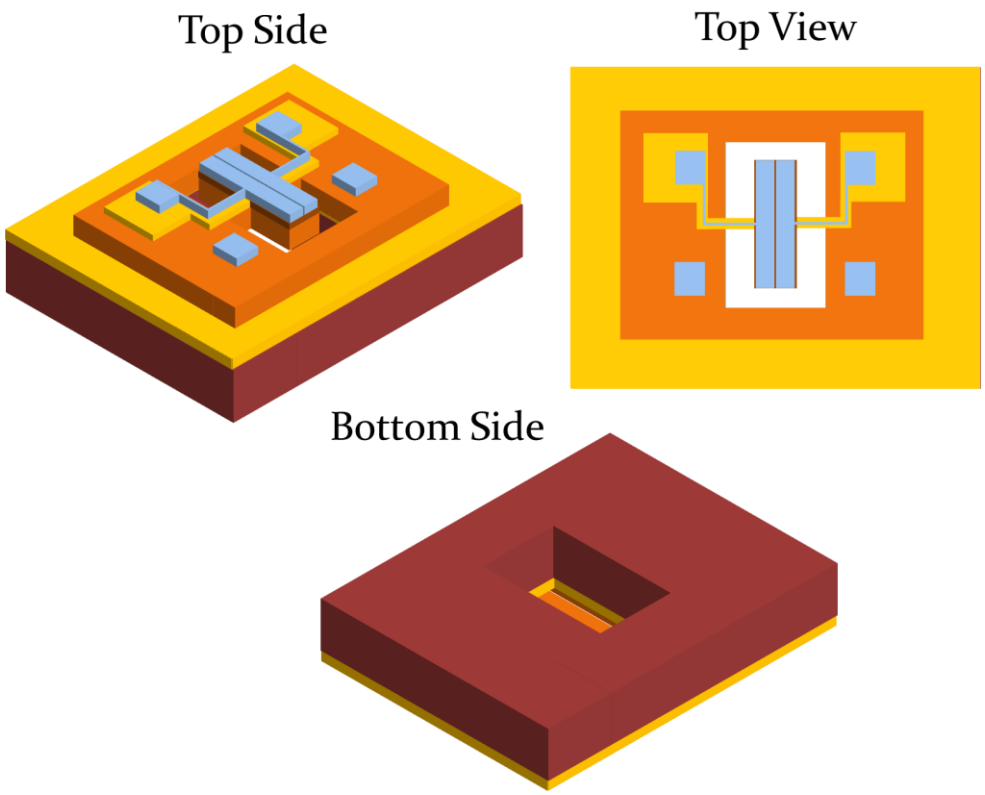

Figure A.9: **Microfabricated Piezoelectric Free-Free Beam Resonator.**

Appendix B

Analytical Formulation of Two-Mode Three-Wave Mixing

Motivated by the experimental results presented in Section 5.2, let us consider a truncated phase space spanning two normal modes Q_a, Q_b.

$$\ddot{Q}_a + \omega_a^2 Q_a + 2\zeta_a \dot{Q}_a + \alpha_{FPU} A_{a,b,b} Q_b^2 = P_D \cos(\omega_D t) \tag{B.1}$$

$$\ddot{Q}_b + \omega_b^2 Q_b + 2\zeta_b \dot{Q}_b + \alpha_{FPU} A_{b,a,b} Q_a Q_b = 0 \tag{B.2}$$

Now, based on the principles of PL method, the time t is first re-scaled to $\tau_q; q \in \{a, b\}$ as $\tau_q = \widetilde{\omega}_q t$. Consequently, the time derivative ∂_t^2 is re-written in terms of the derivative with respect to τ_q as $\partial_t^2 = \widetilde{\omega}_q^2 \partial_{\tau_q}^2$. After substituting these, the equations B.1 and B.2 become

$$\widetilde{\omega}_a^2 \partial_{\tau_a}^2 Q_a + \omega_a^2 Q_a + 2j\zeta_a \partial_{\tau_a} \widetilde{\omega}_a Q_a + \alpha_{FPU} A_{a,b,b} Q_b^2 = P_D \cos\left(\frac{\omega_D}{\widetilde{\omega}_a} \tau_a\right) \tag{B.3}$$

$$\widetilde{\omega}_b^2 \partial_{\tau_b}^2 Q_b + \omega_b^2 Q_b + 2j\zeta_b \partial_{\tau_b} \widetilde{\omega}_b Q_b + \alpha_{FPU} A_{b,a,b} Q_a Q_b = 0 \tag{B.4}$$

We now set the variables Q_q and $\widetilde{\omega}_q$ in terms of the order parameter ε as,

$$Q_q = \sum_{n=0} \varepsilon^n Q_q^{(n)}; \widetilde{\omega}_q^2 = \omega_q^2 + \sum_{n=1} \varepsilon^n \widetilde{\omega}_{q,n}^2 \tag{B.5}$$

$Q_a^{(0)}$ and $Q_b^{(0)}$ correspond to the solutions of equations B.3 and B.4 in the absence of nonlinear coupling terms respectively.

$$\omega_a^2 \partial_{\tau_a}^2 Q_a^{(0)} + \omega_a^2 Q_a^{(0)} + 2j\zeta_a \omega_a \partial_{\tau_a} Q_a^{(0)} = P_D \cos\left(\frac{\omega_D}{\widetilde{\omega}_a} \tau_a\right) \tag{B.6}$$

$$\omega_b^2 \partial_{\tau_b}^2 Q_b^{(0)} + \omega_b^2 Q_b^{(0)} + 2j\zeta_b \omega_b \partial_{\tau_b} Q_b^{(0)} = 0 \tag{B.7}$$

That is, $Q_a^{(0)}$ will simply be $\cos(\omega_D t)$ with amplitude $\frac{P_D}{\omega_a^2-\omega_D^2+2j\zeta\omega_D}$ and $Q_b^{(0)} \cong 0$.

$$\begin{aligned}\omega_a^2\partial_{\tau_a}^2 Q_a^{(1)} + \widetilde{\omega}_{a,1}^2\partial_{\tau_a}^2 Q_a^{(0)} + \omega_a^2 Q_a^{(1)} + 2j\zeta_a\omega_a\partial_{\tau_a}Q_a^{(1)} + 2j\zeta_a\widetilde{\omega}_{a,1}\partial_{\tau_a}Q_a^{(0)} \\ + \alpha_{FPU}A_{a,b,b}Q_b^{(0)}Q_b^{(0)} = P_D\cos\left(\frac{\omega_D}{\widetilde{\omega}_a}\tau_a\right)\end{aligned} \tag{B.8}$$

$$\begin{aligned}\omega_b^2\partial_{\tau_b}^2 Q_b^{(1)} + \widetilde{\omega}_{b,2}^2\partial_{\tau_b}^2 Q_b^{(0)} + \omega_b^2 Q_b^{(1)} + 2j\zeta_b\omega_b\partial_{\tau_b}Q_b^{(1)} + 2j\zeta_b\widetilde{\omega}_{b,1}\partial_{\tau_b}Q_b^{(0)} \\ + \alpha_{FPU}A_{b,a,c}Q_a^{(0)}Q_b^{(0)} = 0\end{aligned} \tag{B.9}$$

Motivated by the experimental results, the solution $Q_b^{(1)}$ is assumed to contain the tone $\cos\left(\frac{\widetilde{\omega}_a}{2}t\right)$. The amplitude of this tone will then be proportional to $\left[\left(\widetilde{\omega}_b^2 - \frac{\widetilde{\omega}_a^2}{4}\right)^2 + \zeta_b^2\widetilde{\omega}_a^2\right]^{-\frac{1}{2}}$. The solution $Q_a^{(1)}$ continues to contain only a single tone $\cos(\omega_D t)$.

$$\begin{aligned}\omega_a^2\partial_{\tau_a}^2 Q_a^{(2)} + \widetilde{\omega}_{a,0}^2\partial_{\tau_a}^2 Q_a^{(2)} + \widetilde{\omega}_{a,1}^2\partial_{\tau_a}^2 Q_a^{(1)} + \widetilde{\omega}_{a,2}^2\partial_{\tau_a}^2 Q_a^{(0)} + \omega_a^2 Q_a^{(2)} + \alpha_{FPU}A_{a,b,b}\left[2Q_b^{(0)}Q_b^{(1)}\right] \\ = P_D\cos\left(\frac{\omega_D}{\widetilde{\omega}_a}\tau_a\right)\end{aligned} \tag{B.10}$$

$$\begin{aligned}\omega_b^2\partial_{\tau_b}^2 Q_b^{(2)} + \widetilde{\omega}_{b,0}^2\partial_{\tau_b}^2 Q_b^{(2)} + \widetilde{\omega}_{b,1}^2\partial_{\tau_b}^2 Q_b^{(1)} + \widetilde{\omega}_{b,2}^2\partial_{\tau_b}^2 Q_b^{(0)} + \omega_b^2 Q_b^{(2)} \\ + \alpha_{FPU}A_{b,a,b}\left[Q_a^{(0)}Q_b^{(1)} + Q_a^{(1)}Q_b^{(0)}\right] = 0\end{aligned} \tag{B.11}$$

$Q_a^{(2)}$ will still be a single tone solution of $\cos(\omega_D t)$. $Q_b^{(2)}$ will however contain an additional tone $\cos\left(\left(\omega_D - \frac{\widetilde{\omega}_a}{2}\right)t\right) = \cos\left(\left(\frac{\widetilde{\omega}_a}{2} + (\omega_D - \widetilde{\omega}_a)\right)t\right)$ which is generated through $Q_a^{(0)}Q_b^{(1)}$.

$$\begin{aligned}\omega_a^2\partial_{\tau_a}^2 Q_a^{(3)} + \widetilde{\omega}_{a,0}^2\partial_{\tau_a}^2 Q_a^{(3)} + \widetilde{\omega}_{a,1}^2\partial_{\tau_a}^2 Q_a^{(2)} + \widetilde{\omega}_{a,2}^2\partial_{\tau_a}^2 Q_a^{(1)} + \widetilde{\omega}_{a,3}^2\partial_{\tau_a}^2 Q_a^{(0)} + \omega_a^2 Q_a^{(3)} \\ + \alpha_{FPU}A_{a,b,b}\left[2Q_b^{(0)}Q_b^{(2)} + Q_b^{(1)}Q_b^{(1)}\right] = P_D\cos\left(\frac{\omega_D}{\widetilde{\omega}_a}\tau_a\right)\end{aligned} \tag{B.12}$$

$$\begin{aligned}\omega_b^2\partial_{\tau_b}^2 Q_b^{(3)} + \widetilde{\omega}_{b,0}^2\partial_{\tau_b}^2 Q_b^{(3)} + \widetilde{\omega}_{b,1}^2\partial_{\tau_b}^2 Q_b^{(2)} + \widetilde{\omega}_{b,2}^2\partial_{\tau_b}^2 Q_b^{(1)} + \widetilde{\omega}_{b,3}^2\partial_{\tau_b}^2 Q_b^{(0)} + \omega_b^2 Q_b^{(3)} \\ + \alpha_{FPU}A_{b,a,b}\left[Q_a^{(0)}Q_b^{(2)} + Q_a^{(1)}Q_b^{(1)} + Q_a^{(2)}Q_b^{(0)}\right] = 0\end{aligned} \tag{B.13}$$

Now, $Q_a^{(3)}$ will also contain the tone $\cos(\widetilde{\omega}_a t)$ which is generated through $Q_b^{(1)}Q_b^{(1)}$. $Q_b^{(3)}$ will however not contain any additional tones compared to $Q_b^{(2)}$.

$$\omega_a^2\partial_{\tau_a}^2 Q_a^{(4)} + \widetilde{\omega}_{a,0}^2\partial_{\tau_a}^2 Q_a^{(4)} + \widetilde{\omega}_{a,1}^2\partial_{\tau_a}^2 Q_a^{(3)} + \widetilde{\omega}_{a,2}^2\partial_{\tau_a}^2 Q_a^{(2)} + \widetilde{\omega}_{a,3}^2\partial_{\tau_a}^2 Q_a^{(1)} + \widetilde{\omega}_{a,4}^2\partial_{\tau_a}^2 Q_a^{(0)} + \omega_a^2 Q_a^{(4)} + \alpha_{FPU}A_{a,b,b}\left[2Q_b^{(0)}Q_b^{(3)} + 2Q_b^{(1)}Q_b^{(2)}\right] = P_D\cos\left(\frac{\omega_D}{\widetilde{\omega}_a}\tau_a\right) \tag{B.14}$$

$$\omega_b^2\partial_{\tau_b}^2 Q_b^{(4)} + \widetilde{\omega}_{b,0}^2\partial_{\tau_b}^2 Q_b^{(4)} + \widetilde{\omega}_{b,1}^2\partial_{\tau_b}^2 Q_b^{(3)} + \widetilde{\omega}_{b,2}^2\partial_{\tau_b}^2 Q_b^{(2)} + \widetilde{\omega}_{b,3}^2\partial_{\tau_b}^2 Q_b^{(1)} + \widetilde{\omega}_{b,4}^2\partial_{\tau_b}^2 Q_b^{(0)} + \omega_b^2 Q_b^{(4)} + \alpha_{FPU}A_{b,a,b}\left[Q_a^{(0)}Q_b^{(3)} + Q_a^{(1)}Q_b^{(2)} + Q_a^{(2)}Q_b^{(1)} + Q_a^{(3)}Q_b^{(0)}\right] = 0 \tag{B.15}$$

$Q_a^{(4)}$ and $Q_b^{(4)}$ will not contain any additional terms compared to $Q_a^{(3)}$ to $Q_b^{(3)}$ respectively.

$$\omega_a^2\partial_{\tau_a}^2 Q_a^{(5)} + \widetilde{\omega}_{a,0}^2\partial_{\tau_a}^2 Q_a^{(5)} + \widetilde{\omega}_{a,1}^2\partial_{\tau_a}^2 Q_a^{(4)} + \widetilde{\omega}_{a,2}^2\partial_{\tau_a}^2 Q_a^{(3)} + \widetilde{\omega}_{a,3}^2\partial_{\tau_a}^2 Q_a^{(2)} + \widetilde{\omega}_{a,4}^2\partial_{\tau_a}^2 Q_a^{(1)} + \widetilde{\omega}_{a,5}^2\partial_{\tau_a}^2 Q_a^{(0)} + \omega_a^2 Q_a^{(5)} + \alpha_{FPU}A_{a,b,b}\left[2Q_b^{(0)}Q_b^{(4)} + 2Q_b^{(1)}Q_b^{(3)} + Q_b^{(2)}Q_b^{(2)}\right] = P_D\cos\left(\frac{\omega_D}{\widetilde{\omega}_a}\tau_a\right) \tag{B.16}$$

$$\omega_b^2\partial_{\tau_b}^2 Q_b^{(5)} + \widetilde{\omega}_{b,0}^2\partial_{\tau_b}^2 Q_b^{(5)} + \widetilde{\omega}_{b,1}^2\partial_{\tau_b}^2 Q_b^{(4)} + \widetilde{\omega}_{b,2}^2\partial_{\tau_b}^2 Q_b^{(3)} + \widetilde{\omega}_{b,3}^2\partial_{\tau_b}^2 Q_b^{(2)} + \widetilde{\omega}_{b,4}^2\partial_{\tau_b}^2 Q_b^{(1)} + \widetilde{\omega}_{b,5}^2\partial_{\tau_b}^2 Q_b^{(0)} + \omega_b^2 Q_b^{(5)} + \alpha_{FPU}A_{b,a,b}\left[Q_a^{(0)}Q_b^{(4)} + Q_a^{(1)}Q_b^{(3)} + Q_a^{(2)}Q_b^{(2)} + Q_a^{(3)}Q_b^{(1)} + Q_a^{(4)}Q_b^{(0)}\right] = 0 \tag{B.17}$$

$Q_a^{(5)}$ will contain the tone $\cos\big((2\omega_D - \widetilde{\omega}_a)t\big) = \cos\Big(\big(\widetilde{\omega}_a + 2(\omega_D - \widetilde{\omega}_a)\big)t\Big)$ in addition to $\cos(\widetilde{\omega}_a t)$ and $\cos(\omega_D t) = \cos\Big(\big(\widetilde{\omega}_a + (\omega_D - \widetilde{\omega}_a)\big)t\Big)$ and is generated through $Q_b^{(2)}Q_b^{(2)}$. $Q_b^{(5)}$ will not contain any additional tones compared to $Q_b^{(4)}$.

$$\omega_a^2\partial_{\tau_a}^2 Q_a^{(6)} + \widetilde{\omega}_{a,0}^2\partial_{\tau_a}^2 Q_a^{(6)} + \widetilde{\omega}_{a,1}^2\partial_{\tau_a}^2 Q_a^{(5)} + \widetilde{\omega}_{a,2}^2\partial_{\tau_a}^2 Q_a^{(4)} + \widetilde{\omega}_{a,3}^2\partial_{\tau_a}^2 Q_a^{(3)} + \widetilde{\omega}_{a,4}^2\partial_{\tau_a}^2 Q_a^{(2)} + \widetilde{\omega}_{a,5}^2\partial_{\tau_a}^2 Q_a^{(1)} + \widetilde{\omega}_{a,6}^2\partial_{\tau_a}^2 Q_a^{(0)} + \omega_a^2 Q_a^{(6)} + \alpha_{FPU}A_{a,b,b}\left[2Q_b^{(0)}Q_b^{(5)} + 2Q_b^{(1)}Q_b^{(4)} + 2Q_b^{(2)}Q_b^{(3)}\right] = P_D\cos\left(\frac{\omega_D}{\widetilde{\omega}_a}\tau_a\right) \tag{B.18}$$

$$\omega_b^2\partial_{\tau_b}^2 Q_b^{(6)} + \widetilde{\omega}_{b,0}^2\partial_{\tau_b}^2 Q_b^{(6)} + \widetilde{\omega}_{b,1}^2\partial_{\tau_b}^2 Q_b^{(5)} + \widetilde{\omega}_{b,2}^2\partial_{\tau_b}^2 Q_b^{(4)} + \widetilde{\omega}_{b,3}^2\partial_{\tau_b}^2 Q_b^{(3)} + \widetilde{\omega}_{b,4}^2\partial_{\tau_b}^2 Q_b^{(2)} + \widetilde{\omega}_{b,5}^2\partial_{\tau_b}^2 Q_b^{(1)} + \widetilde{\omega}_{b,6}^2\partial_{\tau_b}^2 Q_b^{(0)} + \omega_b^2 Q_b^{(6)} + \alpha_{FPU}A_{b,a,b}\left[Q_a^{(0)}Q_b^{(5)} + Q_a^{(1)}Q_b^{(4)} + Q_a^{(2)}Q_b^{(3)} + Q_a^{(3)}Q_b^{(2)} + Q_a^{(4)}Q_b^{(1)} + Q_a^{(5)}Q_b^{(0)}\right] = 0 \tag{B.19}$$

$Q_a^{(6)}$ will not contain any additional tones compared to $Q_a^{(5)}$. However, $Q_b^{(6)}$ will contain an additional tone of $\cos\left(\left(\frac{\widetilde{\omega}_a}{2} - (\omega_D - \widetilde{\omega}_a)\right)t\right)$ through the term $Q_a^{(3)}Q_b^{(2)}$.

$$\begin{aligned}
&\omega_a^2\partial_{\tau_a}^2 Q_a^{(7)} + \widetilde{\omega}_{a,0}^2\partial_{\tau_a}^2 Q_a^{(7)} + \widetilde{\omega}_{a,1}^2\partial_{\tau_a}^2 Q_a^{(6)} + \widetilde{\omega}_{a,2}^2\partial_{\tau_a}^2 Q_a^{(5)} + \widetilde{\omega}_{a,3}^2\partial_{\tau_a}^2 Q_a^{(4)} + \widetilde{\omega}_{a,4}^2\partial_{\tau_a}^2 Q_a^{(3)} \\
&\quad + \widetilde{\omega}_{a,5}^2\partial_{\tau_a}^2 Q_a^{(2)} + \widetilde{\omega}_{a,6}^2\partial_{\tau_a}^2 Q_a^{(1)} + \widetilde{\omega}_{a,7}^2\partial_{\tau_a}^2 Q_a^{(0)} + \omega_a^2 Q_a^{(7)} \\
&\quad + \alpha_{FPU}A_{a,b,b}\left[2Q_b^{(0)}Q_b^{(6)} + 2Q_b^{(1)}Q_b^{(5)} + 2Q_b^{(2)}Q_b^{(4)} + Q_b^{(3)}Q_b^{(3)}\right] \\
&\quad = P_D\cos\left(\frac{\omega_D}{\widetilde{\omega}_a}\tau_a\right)
\end{aligned} \tag{B.20}$$

$$\begin{aligned}
&\omega_b^2\partial_{\tau_b}^2 Q_b^{(7)} + \widetilde{\omega}_{b,0}^2\partial_{\tau_b}^2 Q_b^{(7)} + \widetilde{\omega}_{b,1}^2\partial_{\tau_b}^2 Q_b^{(6)} + \widetilde{\omega}_{b,2}^2\partial_{\tau_b}^2 Q_b^{(5)} + \widetilde{\omega}_{b,3}^2\partial_{\tau_b}^2 Q_b^{(4)} + \widetilde{\omega}_{b,4}^2\partial_{\tau_b}^2 Q_b^{(3)} \\
&\quad + \widetilde{\omega}_{b,5}^2\partial_{\tau_b}^2 Q_b^{(2)} + \widetilde{\omega}_{b,6}^2\partial_{\tau_b}^2 Q_b^{(1)} + \widetilde{\omega}_{b,7}^2\partial_{\tau_b}^2 Q_b^{(0)} + \omega_b^2 Q_b^{(7)} \\
&\quad + \alpha_{FPU}A_{b,a,b}\left[Q_a^{(0)}Q_b^{(6)} + Q_a^{(1)}Q_b^{(5)} + Q_a^{(2)}Q_b^{(4)} + Q_a^{(3)}Q_b^{(3)} + Q_a^{(4)}Q_b^{(2)}\right. \\
&\quad \left. + Q_a^{(5)}Q_b^{(1)} + Q_a^{(6)}Q_b^{(0)}\right] = 0
\end{aligned} \tag{B.21}$$

$Q_a^{(7)}$ will not contain any additional tones compared to $Q_a^{(6)}$. However, $Q_b^{(7)}$ will contain an additional tone of $\cos\left(\left(\frac{\widetilde{\omega}_a}{2} + 2(\omega_D - \widetilde{\omega}_a)\right)t\right)$ through the term $Q_a^{(5)}Q_b^{(1)}$. Hence, $Q_a^{(7)}$ will consist of the tones $\cos(\widetilde{\omega}_a t)$, $\cos\left(\left(\widetilde{\omega}_a + (\omega_D - \widetilde{\omega}_a)\right)t\right)$ and $\cos\left(\left(\widetilde{\omega}_a + 2(\omega_D - \widetilde{\omega}_a)\right)t\right)$ and $Q_b^{(7)}$ will consist of the tones $\cos\left(\left(\frac{\widetilde{\omega}_a}{2} - (\omega_D - \widetilde{\omega}_a)\right)t\right)$, $\cos\left(\frac{\widetilde{\omega}_a}{2}t\right)$, $\cos\left(\left(\frac{\widetilde{\omega}_a}{2} + (\omega_D - \widetilde{\omega}_a)\right)t\right)$ and $\cos\left(\left(\frac{\widetilde{\omega}_a}{2} + 2(\omega_D - \widetilde{\omega}_a)\right)t\right)$.

$$\begin{aligned}
&\omega_a^2\partial_{\tau_a}^2 Q_a^{(n)} + \sum_{n_1+n_2=n}\widetilde{\omega}_{a,n_1}^2\partial_{\tau_a}^2 Q_a^{(n_2)} + \omega_a^2 Q_a^{(n)} + \alpha_{FPU}A_{a,b,b}\sum_{n_1+n_2=n-1}Q_b^{(n_1)}Q_b^{(n_2)} \\
&\quad = P_D\cos\left(\frac{\omega_D}{\widetilde{\omega}_a}\tau_a\right)
\end{aligned} \tag{B.22}$$

$$\omega_b^2\partial_{\tau_b}^2 Q_b^{(n)} + \sum_{n_1+n_2=n}\widetilde{\omega}_{b,n_1}^2\partial_{\tau_b}^2 Q_b^{(n_2)} + \omega_b^2 Q_b^{(n)} + \alpha_{FPU}A_{b,a,b}\sum_{n_1+n_2=n-1}Q_a^{(n_1)}Q_b^{(n_2)} = 0 \tag{B.23}$$

By sequentially solving the equations B.22 and B.23, high-order solutions $Q_a^{(n>7)}$ and $Q_b^{(n>7)}$ can be obtained. Through these iterations, a series of near-resonant tones $\cos\left(\left(\widetilde{\omega}_a \pm p(\omega_D - \widetilde{\omega}_a)\right)t\right)$ & $\cos\left(\left(\frac{\widetilde{\omega}_a}{2} \pm p(\omega_D - \widetilde{\omega}_a)\right)t\right); p \in Z$ can be generated. Hence, the general solution for $Q_{a(b)}$ is given by

$$Q_a = A_0^{(a)} \cos(\widetilde{\omega}_a t) + \sum_{p\neq 0} A_p^{(a)} \cos\big((\widetilde{\omega}_a + p\Delta\omega)t\big) \tag{B.24}$$

$$Q_b = A_0^{(b)} \cos\left(\frac{\widetilde{\omega}_a}{2} t\right) + \sum_{p\neq 0} A_p^{(b)} \cos\left(\left(\frac{\widetilde{\omega}_a}{2} + p\Delta\omega\right)t\right) \tag{B.25}$$

with the amplitude $\left|A_p^{(a)}\right| \sim [(\widetilde{\omega}_a^2 - (\widetilde{\omega}_a + p\Delta\omega)^2)^2 + 4\zeta_a^2(\widetilde{\omega}_a + p\Delta\omega)^2]^{-\frac{1}{2}}$; $\left|A_p^{(b)}\right| \sim \left[\left(\widetilde{\omega}_b^2 - \left(\frac{\widetilde{\omega}_a}{2} + p\Delta\omega\right)^2\right)^2 + 4\zeta_b^2\left(\frac{\widetilde{\omega}_a}{2} + p\Delta\omega\right)^2\right]^{-\frac{1}{2}}$; $p \in Z$ and the frequency spacing $\Delta\omega = |\omega_D - \widetilde{\omega}_a|$. It should be noted that $\widetilde{\omega}_a$ is the re-normalized resonant frequency. While it is difficult to derive an analytical expression for $\widetilde{\omega}_a$ by PL method, its relationship can be understood by phenomenology. As shown in Figure 5.3, $\widetilde{\omega}_a$ stays constant at its nominal value ω_a up till the electrical drive power level $S_{in} = 5\ dBm$. However, when S_{in} is increased above this threshold value, $\widetilde{\omega}_a$ starts to linearly increase with ω_D.

Appendix C

Analytical Formulation of Two-Mode Pumped Three-Wave Mixing

Motivated by the experimental results presented in Section 5.3, let us consider a truncated phase space spanning two normal modes Q_a, Q_b.

$$\ddot{Q}_a + \omega_a^2 Q_a + 2\zeta_a \dot{Q}_a + \alpha_{FPU} A_{a,b,b} Q_b^2 = P_D \cos(\omega_D t) + P_P \cos(\omega_P t) \tag{C.1}$$

$$\ddot{Q}_b + \omega_b^2 Q_b + 2\zeta_b \dot{Q}_b + \alpha_{FPU} A_{b,a,b} Q_a Q_b = 0 \tag{C.2}$$

Now, based on the principles of PL method, the time t is first re-scaled to $\tau_q; q \in \{a, b\}$ as $\tau_q = \widetilde{\omega}_q t$. Consequently, the time derivative ∂_t^2 is re-written in terms of the derivative with respect to τ_q as $\partial_t^2 = \widetilde{\omega}_q^2 \partial_{\tau_q}^2$. After substituting these, the equations C.1 and C.2 become

$$\widetilde{\omega}_a^2 \partial_{\tau_a}^2 Q_a + \omega_a^2 Q_a + 2j\zeta_a \partial_{\tau_a} \widetilde{\omega}_a Q_a + \alpha_{FPU} A_{a,b,b} Q_b^2 = P_D \cos\left(\frac{\omega_D}{\widetilde{\omega}_a}\tau_a\right) + P_P \cos\left(\frac{\omega_P}{\widetilde{\omega}_a}\tau_a\right) \tag{C.3}$$

$$\widetilde{\omega}_b^2 \partial_{\tau_b}^2 Q_b + \omega_b^2 Q_b + 2j\zeta_b \partial_{\tau_b} \widetilde{\omega}_b Q_b + \alpha_{FPU} A_{b,a,b} Q_a Q_b = 0 \tag{C.4}$$

We now set the variables Q_q and $\widetilde{\omega}_q$ in terms of ε as,

$$Q_q = \sum_{n=0} \varepsilon^n Q_q^{(n)}; \widetilde{\omega}_q^2 = \omega_q^2 + \sum_{n=1} \varepsilon^n \widetilde{\omega}_{q,n}^2 \tag{C.5}$$

$Q_a^{(0)}$ and $Q_b^{(0)}$ correspond to the solutions of equations C.3 and C.4 in the absence of nonlinear coupling terms respectively.

$$\omega_a^2 \partial_{\tau_a}^2 Q_a^{(0)} + \omega_a^2 Q_a^{(0)} + 2j\zeta_a \omega_a \partial_{\tau_a} Q_a^{(0)} = P_D \cos\left(\frac{\omega_D}{\widetilde{\omega}_a}\tau_a\right) + P_P \cos\left(\frac{\omega_P}{\widetilde{\omega}_a}\tau_a\right) \tag{C.6}$$

$$\omega_b^2 \partial_{\tau_b}^2 Q_b^{(0)} + \omega_b^2 Q_b^{(0)} + 2j\zeta_b \omega_b \partial_{\tau_b} Q_b^{(0)} = 0 \tag{C.7}$$

That is, $Q_a^{(0)}$ will consist of two tones $\cos(\omega_D t)$ and $\cos(\omega_P t)$ with amplitudes $\frac{P_D}{\omega_a^2-\omega_D^2+2j\zeta\omega_D}$ and $\frac{P_P}{\omega_a^2-\omega_P^2+2j\zeta\omega_P}$ respectively. However, $Q_b^{(0)} \cong 0$.

$$\omega_a^2\partial_{\tau_a}^2 Q_a^{(1)} + \widetilde{\omega}_{a,1}^2\partial_{\tau_a}^2 Q_a^{(0)} + \omega_a^2 Q_a^{(1)} + 2j\zeta_a\omega_a\partial_{\tau_a} Q_a^{(1)} + 2j\zeta_a\widetilde{\omega}_{a,1}\partial_{\tau_a} Q_a^{(0)} + \alpha_{FPU}A_{a,b,b}Q_b^{(0)}Q_b^{(0)} = P_D\cos\left(\frac{\omega_D}{\widetilde{\omega}_a}\tau_a\right) + P_P\cos\left(\frac{\omega_P}{\widetilde{\omega}_a}\tau_a\right) \quad \text{(C.8)}$$

$$\omega_b^2\partial_{\tau_b}^2 Q_b^{(1)} + \widetilde{\omega}_{b,2}^2\partial_{\tau_b}^2 Q_b^{(0)} + \omega_b^2 Q_b^{(1)} + 2j\zeta_b\omega_b\partial_{\tau_b} Q_b^{(1)} + 2j\zeta_b\widetilde{\omega}_{b,1}\partial_{\tau_b} Q_b^{(0)} + \alpha_{FPU}A_{b,a,c}Q_a^{(0)}Q_b^{(0)} = 0 \quad \text{(C.9)}$$

Motivated by the experimental results presented in Figure 5.14, the solution $Q_b^{(1)}$ can either contain $\cos\left(\frac{\omega_D}{2}t\right)$ or $\cos\left(\frac{\omega_P}{2}t\right)$. For the sake of this analysis, we consider the case where $Q_b^{(1)}$ contains $\cos\left(\frac{\omega_D}{2}t\right)$. The amplitude of this tone will then be proportional to $\left[\left(\widetilde{\omega}_b^2 - \frac{\omega_D^2}{4}\right)^2 + \zeta_b^2\omega_D^2\right]^{-\frac{1}{2}}$. The solution $Q_a^{(1)}$ continues to contain the previously generated tones $\cos(\omega_D t)$ and $\cos(\omega_P t)$.

$$\omega_a^2\partial_{\tau_a}^2 Q_a^{(2)} + \widetilde{\omega}_{a,0}^2\partial_{\tau_a}^2 Q_a^{(2)} + \widetilde{\omega}_{a,1}^2\partial_{\tau_a}^2 Q_a^{(1)} + \widetilde{\omega}_{a,2}^2\partial_{\tau_a}^2 Q_a^{(0)} + \omega_a^2 Q_a^{(2)} + \alpha_{FPU}A_{a,b,b}\left[2Q_b^{(0)}Q_b^{(1)}\right] = P_D\cos\left(\frac{\omega_D}{\widetilde{\omega}_a}\tau_a\right) + P_P\cos\left(\frac{\omega_P}{\widetilde{\omega}_a}\tau_a\right) \quad \text{(C.10)}$$

$$\omega_b^2\partial_{\tau_b}^2 Q_b^{(2)} + \widetilde{\omega}_{b,0}^2\partial_{\tau_b}^2 Q_b^{(2)} + \widetilde{\omega}_{b,1}^2\partial_{\tau_b}^2 Q_b^{(1)} + \widetilde{\omega}_{b,2}^2\partial_{\tau_b}^2 Q_b^{(0)} + \omega_b^2 Q_b^{(2)} + \alpha_{FPU}A_{b,a,b}\left[Q_a^{(0)}Q_b^{(1)} + Q_a^{(1)}Q_b^{(0)}\right] = 0 \quad \text{(C.11)}$$

$Q_a^{(2)}$ will not contain any additional tones compared to $Q_a^{(1)}$. $Q_b^{(2)}$ will however contain an additional tone $\cos\left(\left(\omega_P - \frac{\omega_D}{2}\right)t\right) = \cos\left(\left(\frac{\omega_D}{2} + (\omega_P - \omega_D)\right)t\right)$ which is generated through $Q_a^{(0)}Q_b^{(1)}$.

$$\omega_a^2\partial_{\tau_a}^2 Q_a^{(3)} + \widetilde{\omega}_{a,0}^2\partial_{\tau_a}^2 Q_a^{(3)} + \widetilde{\omega}_{a,1}^2\partial_{\tau_a}^2 Q_a^{(2)} + \widetilde{\omega}_{a,2}^2\partial_{\tau_a}^2 Q_a^{(1)} + \widetilde{\omega}_{a,3}^2\partial_{\tau_a}^2 Q_a^{(0)} + \omega_a^2 Q_a^{(3)} + \alpha_{FPU}A_{a,b,b}\left[2Q_b^{(0)}Q_b^{(2)} + Q_b^{(1)}Q_b^{(1)}\right] = P_D\cos\left(\frac{\omega_D}{\widetilde{\omega}_a}\tau_a\right) + P_P\cos\left(\frac{\omega_P}{\widetilde{\omega}_a}\tau_a\right) \quad \text{(C.12)}$$

$$\omega_b^2\partial_{\tau_b}^2 Q_b^{(3)} + \widetilde{\omega}_{b,0}^2\partial_{\tau_b}^2 Q_b^{(3)} + \widetilde{\omega}_{b,1}^2\partial_{\tau_b}^2 Q_b^{(2)} + \widetilde{\omega}_{b,2}^2\partial_{\tau_b}^2 Q_b^{(1)} + \widetilde{\omega}_{b,3}^2\partial_{\tau_b}^2 Q_b^{(0)} + \omega_b^2 Q_b^{(3)} + \alpha_{FPU}A_{b,a,b}\left[Q_a^{(0)}Q_b^{(2)} + Q_a^{(1)}Q_b^{(1)} + Q_a^{(2)}Q_b^{(0)}\right] = 0 \quad \text{(C.13)}$$

$Q_a^{(3)}$ and $Q_b^{(3)}$ will not contain any additional tones compared to $Q_a^{(2)}$ and $Q_b^{(2)}$ respectively.

$$\begin{aligned}\omega_a^2\partial_{\tau_a}^2 Q_a^{(4)} + \widetilde{\omega}_{a,0}^2\partial_{\tau_a}^2 Q_a^{(4)} + \widetilde{\omega}_{a,1}^2\partial_{\tau_a}^2 Q_a^{(3)} + \widetilde{\omega}_{a,2}^2\partial_{\tau_a}^2 Q_a^{(2)} + \widetilde{\omega}_{a,3}^2\partial_{\tau_a}^2 Q_a^{(1)} + \widetilde{\omega}_{a,4}^2\partial_{\tau_a}^2 Q_a^{(0)} \\ + \omega_a^2 Q_a^{(4)} + \alpha_{FPU}A_{a,b,b}\left[2Q_b^{(0)}Q_b^{(3)} + 2Q_b^{(1)}Q_b^{(2)}\right] \\ = P_D\cos\left(\frac{\omega_D}{\widetilde{\omega}_a}\tau_a\right) + P_P\cos\left(\frac{\omega_P}{\widetilde{\omega}_a}\tau_a\right)\end{aligned} \tag{C.14}$$

$$\begin{aligned}\omega_b^2\partial_{\tau_b}^2 Q_b^{(4)} + \widetilde{\omega}_{b,0}^2\partial_{\tau_b}^2 Q_b^{(4)} + \widetilde{\omega}_{b,1}^2\partial_{\tau_b}^2 Q_b^{(3)} + \widetilde{\omega}_{b,2}^2\partial_{\tau_b}^2 Q_b^{(2)} + \widetilde{\omega}_{b,3}^2\partial_{\tau_b}^2 Q_b^{(1)} + \widetilde{\omega}_{b,4}^2\partial_{\tau_b}^2 Q_b^{(0)} \\ + \omega_b^2 Q_b^{(4)} + \alpha_{FPU}A_{b,a,b}\left[Q_a^{(0)}Q_b^{(3)} + Q_a^{(1)}Q_b^{(2)} + Q_a^{(2)}Q_b^{(1)} + Q_a^{(3)}Q_b^{(0)}\right] = 0\end{aligned} \tag{C.15}$$

$Q_a^{(4)}$ and $Q_b^{(4)}$ will not contain any additional terms compared to $Q_a^{(3)}$ to $Q_b^{(3)}$ respectively.

$$\begin{aligned}\omega_a^2\partial_{\tau_a}^2 Q_a^{(5)} + \widetilde{\omega}_{a,0}^2\partial_{\tau_a}^2 Q_a^{(5)} + \widetilde{\omega}_{a,1}^2\partial_{\tau_a}^2 Q_a^{(4)} + \widetilde{\omega}_{a,2}^2\partial_{\tau_a}^2 Q_a^{(3)} + \widetilde{\omega}_{a,3}^2\partial_{\tau_a}^2 Q_a^{(2)} + \widetilde{\omega}_{a,4}^2\partial_{\tau_a}^2 Q_a^{(1)} \\ + \widetilde{\omega}_{a,5}^2\partial_{\tau_a}^2 Q_a^{(0)} + \omega_a^2 Q_a^{(5)} + \alpha_{FPU}A_{a,b,b}\left[2Q_b^{(0)}Q_b^{(4)} + 2Q_b^{(1)}Q_b^{(3)} + Q_b^{(2)}Q_b^{(2)}\right] \\ = P_D\cos\left(\frac{\omega_D}{\widetilde{\omega}_a}\tau_a\right) + P_P\cos\left(\frac{\omega_P}{\widetilde{\omega}_a}\tau_a\right)\end{aligned} \tag{C.16}$$

$$\begin{aligned}\omega_b^2\partial_{\tau_b}^2 Q_b^{(5)} + \widetilde{\omega}_{b,0}^2\partial_{\tau_b}^2 Q_b^{(5)} + \widetilde{\omega}_{b,1}^2\partial_{\tau_b}^2 Q_b^{(4)} + \widetilde{\omega}_{b,2}^2\partial_{\tau_b}^2 Q_b^{(3)} + \widetilde{\omega}_{b,3}^2\partial_{\tau_b}^2 Q_b^{(2)} + \widetilde{\omega}_{b,4}^2\partial_{\tau_b}^2 Q_b^{(1)} \\ + \widetilde{\omega}_{b,5}^2\partial_{\tau_b}^2 Q_b^{(0)} + \omega_b^2 Q_b^{(5)} \\ + \alpha_{FPU}A_{b,a,b}\left[Q_a^{(0)}Q_b^{(4)} + Q_a^{(1)}Q_b^{(3)} + Q_a^{(2)}Q_b^{(2)} + Q_a^{(3)}Q_b^{(1)} + Q_a^{(4)}Q_b^{(0)}\right] = 0\end{aligned} \tag{C.17}$$

$Q_a^{(5)}$ will contain the tone $\cos\big((2\omega_P - \omega_D)t\big) = \cos\Big(\big(\omega_D + 2(\omega_P - \omega_D)\big)t\Big)$ in addition to $\cos(\omega_D t)$ and $\cos(\omega_P t) = \cos\Big(\big(\omega_D + (\omega_P - \omega_D)\big)t\Big)$ and is generated through $Q_b^{(2)}Q_b^{(2)}$. $Q_b^{(5)}$ will not contain any additional tones compared to $Q_b^{(4)}$.

$$\begin{aligned}\omega_a^2\partial_{\tau_a}^2 Q_a^{(6)} + \widetilde{\omega}_{a,0}^2\partial_{\tau_a}^2 Q_a^{(6)} + \widetilde{\omega}_{a,1}^2\partial_{\tau_a}^2 Q_a^{(5)} + \widetilde{\omega}_{a,2}^2\partial_{\tau_a}^2 Q_a^{(4)} + \widetilde{\omega}_{a,3}^2\partial_{\tau_a}^2 Q_a^{(3)} + \widetilde{\omega}_{a,4}^2\partial_{\tau_a}^2 Q_a^{(2)} \\ + \widetilde{\omega}_{a,5}^2\partial_{\tau_a}^2 Q_a^{(1)} + \widetilde{\omega}_{a,6}^2\partial_{\tau_a}^2 Q_a^{(0)} + \omega_a^2 Q_a^{(6)} \\ + \alpha_{FPU}A_{a,b,b}\left[2Q_b^{(0)}Q_b^{(5)} + 2Q_b^{(1)}Q_b^{(4)} + 2Q_b^{(2)}Q_b^{(3)}\right] \\ = P_D\cos\left(\frac{\omega_D}{\widetilde{\omega}_a}\tau_a\right) + P_P\cos\left(\frac{\omega_P}{\widetilde{\omega}_a}\tau_a\right)\end{aligned} \tag{C.18}$$

$$\begin{aligned}\omega_b^2\partial_{\tau_b}^2 Q_b^{(6)} + \widetilde{\omega}_{b,0}^2\partial_{\tau_b}^2 Q_b^{(6)} + \widetilde{\omega}_{b,1}^2\partial_{\tau_b}^2 Q_b^{(5)} + \widetilde{\omega}_{b,2}^2\partial_{\tau_b}^2 Q_b^{(4)} + \widetilde{\omega}_{b,3}^2\partial_{\tau_b}^2 Q_b^{(3)} + \widetilde{\omega}_{b,4}^2\partial_{\tau_b}^2 Q_b^{(2)} \\ + \widetilde{\omega}_{b,5}^2\partial_{\tau_b}^2 Q_b^{(1)} + \widetilde{\omega}_{b,6}^2\partial_{\tau_b}^2 Q_b^{(0)} + \omega_b^2 Q_b^{(6)} \\ + \alpha_{FPU}A_{b,a,b}\left[Q_a^{(0)}Q_b^{(5)} + Q_a^{(1)}Q_b^{(4)} + Q_a^{(2)}Q_b^{(3)} + Q_a^{(3)}Q_b^{(2)} + Q_a^{(4)}Q_b^{(1)}\right. \\ \left. + Q_a^{(5)}Q_b^{(0)}\right] = 0\end{aligned} \tag{C.19}$$

$Q_a^{(6)}$ will not contain any additional tones compared to $Q_a^{(5)}$. However, $Q_b^{(6)}$ will contain an additional tone of $\cos\left(\left(\frac{\omega_D}{2} - (\omega_P - \omega_D)\right)t\right)$ through the term $Q_a^{(3)}Q_b^{(2)}$.

$$\begin{aligned}\omega_a^2\partial_{\tau_a}^2 Q_a^{(7)} + \widetilde{\omega}_{a,0}^2\partial_{\tau_a}^2 Q_a^{(7)} + \widetilde{\omega}_{a,1}^2\partial_{\tau_a}^2 Q_a^{(6)} + \widetilde{\omega}_{a,2}^2\partial_{\tau_a}^2 Q_a^{(5)} + \widetilde{\omega}_{a,3}^2\partial_{\tau_a}^2 Q_a^{(4)} + \widetilde{\omega}_{a,4}^2\partial_{\tau_a}^2 Q_a^{(3)} \\ + \widetilde{\omega}_{a,5}^2\partial_{\tau_a}^2 Q_a^{(2)} + \widetilde{\omega}_{a,6}^2\partial_{\tau_a}^2 Q_a^{(1)} + \widetilde{\omega}_{a,7}^2\partial_{\tau_a}^2 Q_a^{(0)} + \omega_a^2 Q_a^{(7)} \\ + \alpha_{FPU}A_{a,b,b}\left[2Q_b^{(0)}Q_b^{(6)} + 2Q_b^{(1)}Q_b^{(5)} + 2Q_b^{(2)}Q_b^{(4)} + Q_b^{(3)}Q_b^{(3)}\right] \\ = P_D\cos\left(\frac{\omega_D}{\widetilde{\omega}_a}\tau_a\right) + P_P\cos\left(\frac{\omega_P}{\widetilde{\omega}_a}\tau_a\right)\end{aligned} \tag{C.20}$$

$$\begin{aligned}\omega_b^2\partial_{\tau_b}^2 Q_b^{(7)} + \widetilde{\omega}_{b,0}^2\partial_{\tau_b}^2 Q_b^{(7)} + \widetilde{\omega}_{b,1}^2\partial_{\tau_b}^2 Q_b^{(6)} + \widetilde{\omega}_{b,2}^2\partial_{\tau_b}^2 Q_b^{(5)} + \widetilde{\omega}_{b,3}^2\partial_{\tau_b}^2 Q_b^{(4)} + \widetilde{\omega}_{b,4}^2\partial_{\tau_b}^2 Q_b^{(3)} \\ + \widetilde{\omega}_{b,5}^2\partial_{\tau_b}^2 Q_b^{(2)} + \widetilde{\omega}_{b,6}^2\partial_{\tau_b}^2 Q_b^{(1)} + \widetilde{\omega}_{b,7}^2\partial_{\tau_b}^2 Q_b^{(0)} + \omega_b^2 Q_b^{(7)} \\ + \alpha_{FPU}A_{b,a,b}\left[Q_a^{(0)}Q_b^{(6)} + Q_a^{(1)}Q_b^{(5)} + Q_a^{(2)}Q_b^{(4)} + Q_a^{(3)}Q_b^{(3)} + Q_a^{(4)}Q_b^{(2)}\right. \\ \left. + Q_a^{(5)}Q_b^{(1)} + Q_a^{(6)}Q_b^{(0)}\right] = 0\end{aligned} \tag{C.21}$$

$Q_a^{(7)}$ will not contain any additional tones compared to $Q_a^{(6)}$. However, $Q_b^{(7)}$ will contain an additional tone of $\cos\left(\left(\frac{\omega_D}{2} + 2(\omega_P - \omega_D)\right)t\right)$ through the term $Q_a^{(5)}Q_b^{(1)}$.

Hence, $Q_a^{(7)}$ will consist of the tones $\cos(\omega_D t)$, $\cos\left(\left(\omega_D + (\omega_P - \omega_D)\right)t\right)$ and $\cos\left(\left(\omega_D + 2(\omega_P - \omega_D)\right)t\right)$ and $Q_b^{(7)}$ will consist of the tones $\cos\left(\left(\frac{\omega_D}{2} - (\omega_P - \omega_D)\right)t\right)$, $\cos\left(\frac{\omega_D}{2}t\right)$, $\cos\left(\left(\frac{\omega_D}{2} + (\omega_P - \omega_D)\right)t\right)$ and $\cos\left(\left(\frac{\omega_D}{2} + 2(\omega_P - \omega_D)\right)t\right)$.

$$\begin{aligned}\omega_a^2\partial_{\tau_a}^2 Q_a^{(n)} + \sum_{n_1+n_2=n}\widetilde{\omega}_{a,n_1}^2\partial_{\tau_a}^2 Q_a^{(n_2)} + \omega_a^2 Q_a^{(n)} + \alpha_{FPU}A_{a,b,b}\sum_{n_1+n_2=n-1}Q_b^{(n_1)}Q_b^{(n_2)} \\ = P_D\cos\left(\frac{\omega_D}{\widetilde{\omega}_a}\tau_a\right) + P_P\cos\left(\frac{\omega_P}{\widetilde{\omega}_a}\tau_a\right)\end{aligned} \tag{C.22}$$

$$\omega_b^2 \partial_{\tau_b}^2 Q_b^{(n)} + \sum_{n_1+n_2=n} \widetilde{\omega}_{b,n_1}^2 \partial_{\tau_b}^2 Q_b^{(n_2)} + \omega_b^2 Q_b^{(n)} + \alpha_{FPU} A_{b,a,b} \sum_{n_1+n_2=n-1} Q_a^{(n_1)} Q_b^{(n_2)} = 0 \qquad \text{(C.23)}$$

By sequentially solving the equations C.22 and C.23, high-order solutions $Q_a^{(n>7)}$ and $Q_b^{(n>7)}$ can be obtained. Through these iterations, a series of near-resonant tones $\cos\Big(\big(\omega_D + p(\omega_P - \omega_D)\big)t\Big)$ & $\cos\left(\left(\frac{\omega_D}{2} + p(\omega_P - \omega_D)\right)t\right); p \in Z$ can be generated. Hence, the general solution for $Q_{a(b)}$ is given by

$$Q_a = A_0^{(a)} \cos(\omega_D t) + \sum_{p\neq 0} A_p^{(a)} \cos\big((\omega_D + p\Delta\omega)t\big) \qquad \text{(C.24)}$$

$$Q_b = A_0^{(b)} \cos\left(\frac{\omega_D}{2} t\right) + \sum_{p\neq 0} A_p^{(b)} \cos\left(\left(\frac{\omega_D}{2} + p\Delta\omega\right)t\right) \qquad \text{(C.25)}$$

with the amplitude $\left|A_p^{(a)}\right| \sim [(\widetilde{\omega}_a^2 - (\omega_D + p\Delta\omega)^2)^2 + 4\zeta_a^2(\omega_D + p\Delta\omega)^2]^{-\frac{1}{2}}; \left|A_p^{(b)}\right| \sim \left[\left(\widetilde{\omega}_b^2 - \left(\frac{\omega_D}{2} + p\Delta\omega\right)^2\right)^2 + 4\zeta_b^2\left(\frac{\omega_D}{2} + p\Delta\omega\right)^2\right]^{-\frac{1}{2}}; p \in Z$ and $\Delta\omega = |\omega_P - \omega_D|$.

Appendix D

Analytical Formulation of Three-Mode Four-Wave Mixing

Motivated by the experimental results presented in Section 5.4, let us consider a truncated phase space spanning three normal modes Q_a, Q_b, Q_c.

$$\ddot{Q}_a + \omega_a^2 Q_a + 2\zeta_a \dot{Q}_a + \alpha_{FPU} A_{a,b,c} Q_b Q_c = P_D \cos(\omega_D t) \tag{D.1}$$

$$\ddot{Q}_b + \omega_b^2 Q_b + 2\zeta_b \dot{Q}_b + \alpha_{FPU} A_{b,a,c} Q_a Q_c = 0 \tag{D.2}$$

$$\ddot{Q}_c + \omega_c^2 Q_c + 2\zeta_c \dot{Q}_c + \alpha_{FPU} A_{c,a,b} Q_a Q_b = 0 \tag{D.3}$$

Now, based on the principles of PL method, the time t is first re-scaled to $\tau_q; q \in \{a, b, c\}$ as $\tau_q = \widetilde{\omega}_q t$. Consequently, the time derivative ∂_t^2 is re-written in terms of the derivative with respect to τ_q as $\partial_t^2 = \widetilde{\omega}_q^2 \partial_{\tau_q}^2$. After substituting these, the equations D.1-D-3 become

$$\widetilde{\omega}_a^2 \partial_{\tau_a}^2 Q_a + \omega_a^2 Q_a + 2j\zeta_a \partial_{\tau_a} \widetilde{\omega}_a Q_a + \alpha_{FPU} A_{a,b,c} Q_b Q_c = P_D \cos\left(\frac{\omega_D}{\widetilde{\omega}_a} \tau_a\right) \tag{D.4}$$

$$\widetilde{\omega}_b^2 \partial_{\tau_b}^2 Q_b + \omega_b^2 Q_b + 2j\zeta_b \partial_{\tau_b} \widetilde{\omega}_b Q_b + \alpha_{FPU} A_{b,a,c} Q_a Q_c = 0 \tag{D.5}$$

$$\widetilde{\omega}_c^2 \partial_{\tau_c}^2 Q_c + \omega_c^2 Q_c + 2j\zeta_c \partial_{\tau_c} \widetilde{\omega}_c Q_c + \alpha_{FPU} A_{c,a,b} Q_a Q_b = 0 \tag{D.6}$$

We now set the variables Q_q and $\widetilde{\omega}_q$ in terms of ε as,

$$Q_q = \sum_{n=0} \varepsilon^n Q_q^{(n)}; \widetilde{\omega}_q^2 = \omega_q^2 + \sum_{n=1} \varepsilon^n \widetilde{\omega}_{q,n}^2 \tag{D.7}$$

$Q_a^{(0)}$, $Q_b^{(0)}$ and $Q_c^{(0)}$ correspond to the solutions of equations D.4-D.7 in the absence of nonlinear coupling terms respectively.

$$\omega_a^2 \partial_{\tau_a}^2 Q_a^{(0)} + \omega_a^2 Q_a^{(0)} + 2j\zeta_a \omega_a \partial_{\tau_a} Q_a^{(0)} = P_D \cos\left(\frac{\omega_D}{\widetilde{\omega}_a} \tau_a\right) \tag{D.8}$$

$$\omega_b^2 \partial_{\tau_b}^2 Q_b^{(0)} + \omega_b^2 Q_b^{(0)} + 2j\zeta_b \omega_b \partial_{\tau_b} Q_b^{(0)} = 0 \tag{D.9}$$

$$\omega_c^2 \partial_{\tau_c}^2 Q_c^{(0)} + \omega_c^2 Q_c^{(0)} + 2j\zeta_c \omega_c \partial_{\tau_c} Q_c^{(0)} = 0 \tag{D.10}$$

That is, $Q_a^{(0)}$ will simply be $\cos(\omega_D t)$ with amplitude $\frac{P_D}{\omega_a^2 - \omega_D^2 + 2j\zeta\omega_D}$. $\cos(\omega_D t)$. However, $Q_b^{(0)} = Q_c^{(0)} = 0$.

$$\begin{aligned} &\omega_a^2 \partial_{\tau_a}^2 Q_a^{(1)} + \widetilde{\omega}_{a,1}^2 \partial_{\tau_a}^2 Q_a^{(0)} + \omega_a^2 Q_a^{(1)} + 2j\zeta_a \omega_a \partial_{\tau_a} Q_a^{(1)} + 2j\zeta_a \widetilde{\omega}_{a,1} \partial_{\tau_a} Q_a^{(0)} \\ &\qquad + \alpha_{FPU} A_{a,b,c} Q_b^{(0)} Q_c^{(0)} = P_D \cos\left(\frac{\omega_D}{\widetilde{\omega}_a} \tau_a\right) \end{aligned} \tag{D.11}$$

$$\begin{aligned} &\omega_b^2 \partial_{\tau_b}^2 Q_b^{(1)} + \widetilde{\omega}_{b,2}^2 \partial_{\tau_b}^2 Q_b^{(0)} + \omega_b^2 Q_b^{(1)} + 2j\zeta_b \omega_b \partial_{\tau_b} Q_b^{(1)} + 2j\zeta_b \widetilde{\omega}_{b,1} \partial_{\tau_b} Q_b^{(0)} \\ &\qquad + \alpha_{FPU} A_{b,a,c} Q_a^{(0)} Q_c^{(0)} = 0 \end{aligned} \tag{D.12}$$

$$\begin{aligned} &\omega_c^2 \partial_{\tau_c}^2 Q_c^{(1)} + \widetilde{\omega}_{c,2}^2 \partial_{\tau_c}^2 Q_c^{(0)} + \omega_c^2 Q_c^{(1)} + 2j\zeta_c \omega_c \partial_{\tau_c} Q_c^{(1)} + 2j\zeta_c \widetilde{\omega}_{c,1} \partial_{\tau_c} Q_c^{(0)} \\ &\qquad + \alpha_{FPU} A_{c,a,b} Q_a^{(0)} Q_b^{(0)} = 0 \end{aligned} \tag{D.13}$$

Motivated by the experimental results, the solution $Q_b^{(1)}$ and $Q_c^{(1)}$ are assumed to contain the tones $\cos(\omega_m t)$ and $\cos(\omega_n t)$ respectively such that $\omega_m + \omega_n = \widetilde{\omega}_a$. The amplitudes of these tones will then be proportional to $\left[\left(\widetilde{\omega}_b^2 - \omega_m^2\right)^2 + 4\zeta_b^2 \omega_m^2\right]^{-\frac{1}{2}}$ and $\left[\left(\widetilde{\omega}_b^2 - \omega_n^2\right)^2 + 4\zeta_b^2 \omega_n^2\right]^{-\frac{1}{2}}$ respectively. The solution $Q_a^{(1)}$ continues to contain only $\cos(\omega_D t)$.

$$\begin{aligned} &\omega_a^2 \partial_{\tau_a}^2 Q_a^{(2)} + \widetilde{\omega}_{a,0}^2 \partial_{\tau_a}^2 Q_a^{(2)} + \widetilde{\omega}_{a,1}^2 \partial_{\tau_a}^2 Q_a^{(1)} + \widetilde{\omega}_{a,2}^2 \partial_{\tau_a}^2 Q_a^{(0)} + \omega_a^2 Q_a^{(2)} \\ &\qquad + \alpha_{FPU} A_{a,b,c} \left[Q_b^{(0)} Q_c^{(1)} + Q_b^{(1)} Q_c^{(0)}\right] = P_D \cos\left(\frac{\omega_D}{\widetilde{\omega}_a} \tau_a\right) \end{aligned} \tag{D.14}$$

$$\begin{aligned} &\omega_b^2 \partial_{\tau_b}^2 Q_b^{(2)} + \widetilde{\omega}_{b,0}^2 \partial_{\tau_b}^2 Q_b^{(2)} + \widetilde{\omega}_{b,1}^2 \partial_{\tau_b}^2 Q_b^{(1)} + \widetilde{\omega}_{b,2}^2 \partial_{\tau_b}^2 Q_b^{(0)} + \omega_b^2 Q_b^{(2)} \\ &\qquad + \alpha_{FPU} A_{b,a,c} \left[Q_a^{(0)} Q_c^{(1)} + Q_a^{(1)} Q_c^{(0)}\right] = 0 \end{aligned} \tag{D.15}$$

$$\begin{aligned} &\omega_c^2 \partial_{\tau_c}^2 Q_c^{(2)} + \widetilde{\omega}_{c,0}^2 \partial_{\tau_c}^2 Q_c^{(2)} + \widetilde{\omega}_{c,1}^2 \partial_{\tau_c}^2 Q_c^{(1)} + \widetilde{\omega}_{c,2}^2 \partial_{\tau_c}^2 Q_c^{(0)} + \omega_c^2 Q_c^{(2)} \\ &\qquad + \alpha_{FPU} A_{c,a,b} \left[Q_a^{(0)} Q_b^{(1)} + Q_a^{(1)} Q_b^{(0)}\right] = 0 \end{aligned} \tag{D.16}$$

$Q_a^{(2)}$ will still be a single tone solution of $\cos(\omega_D t)$. $Q_b^{(2)}$ and $Q_c^{(2)}$ will however contain the additional tones $\cos\big((\omega_D - \omega_n)t\big)$ and $\cos\big((\omega_D - \omega_m)t\big)$ respectively. These tones are generated through $Q_a^{(0)} Q_c^{(1)}$ and $Q_a^{(0)} Q_b^{(1)}$ respectively.

$$\omega_a^2\partial_{\tau_a}^2 Q_a^{(3)} + \widetilde{\omega}_{a,0}^2\partial_{\tau_a}^2 Q_a^{(3)} + \widetilde{\omega}_{a,1}^2\partial_{\tau_a}^2 Q_a^{(2)} + \widetilde{\omega}_{a,2}^2\partial_{\tau_a}^2 Q_a^{(1)} + \widetilde{\omega}_{a,3}^2\partial_{\tau_a}^2 Q_a^{(0)} + \omega_a^2 Q_a^{(3)} + \alpha_{FPU}A_{a,b,c}\left[Q_b^{(0)}Q_c^{(2)} + Q_b^{(1)}Q_c^{(1)} + Q_b^{(2)}Q_c^{(0)}\right] = P_D\cos\left(\frac{\omega_D}{\widetilde{\omega}_a}\tau_a\right) \tag{D.17}$$

$$\omega_b^2\partial_{\tau_b}^2 Q_b^{(3)} + \widetilde{\omega}_{b,0}^2\partial_{\tau_b}^2 Q_b^{(3)} + \widetilde{\omega}_{b,1}^2\partial_{\tau_b}^2 Q_b^{(2)} + \widetilde{\omega}_{b,2}^2\partial_{\tau_b}^2 Q_b^{(1)} + \widetilde{\omega}_{b,3}^2\partial_{\tau_b}^2 Q_b^{(0)} + \omega_b^2 Q_b^{(3)} + \alpha_{FPU}A_{b,a,c}\left[Q_a^{(0)}Q_c^{(2)} + Q_a^{(1)}Q_c^{(1)} + Q_a^{(2)}Q_c^{(0)}\right] = 0 \tag{D.18}$$

$$\omega_c^2\partial_{\tau_c}^2 Q_c^{(3)} + \widetilde{\omega}_{c,0}^2\partial_{\tau_c}^2 Q_c^{(3)} + \widetilde{\omega}_{c,1}^2\partial_{\tau_c}^2 Q_c^{(2)} + \widetilde{\omega}_{c,2}^2\partial_{\tau_c}^2 Q_c^{(1)} + \widetilde{\omega}_{c,3}^2\partial_{\tau_c}^2 Q_c^{(0)} + \omega_c^2 Q_c^{(3)} + \alpha_{FPU}A_{c,a,b}\left[Q_a^{(0)}Q_b^{(2)} + Q_a^{(1)}Q_b^{(1)} + Q_a^{(2)}Q_b^{(0)}\right] = 0 \tag{D.19}$$

Now, $Q_a^{(3)}$ will also contain the tone $\cos(\widetilde{\omega}_a t)$ which is generated through $Q_b^{(1)}Q_c^{(1)}$. $Q_b^{(3)}$ and $Q_c^{(3)}$ will however not contain any additional tones compared to $Q_b^{(2)}$ and $Q_c^{(2)}$ respectively.

$$\omega_a^2\partial_{\tau_a}^2 Q_a^{(4)} + \widetilde{\omega}_{a,0}^2\partial_{\tau_a}^2 Q_a^{(4)} + \widetilde{\omega}_{a,1}^2\partial_{\tau_a}^2 Q_a^{(3)} + \widetilde{\omega}_{a,2}^2\partial_{\tau_a}^2 Q_a^{(2)} + \widetilde{\omega}_{a,3}^2\partial_{\tau_a}^2 Q_a^{(1)} + \widetilde{\omega}_{a,4}^2\partial_{\tau_a}^2 Q_a^{(0)} + \omega_a^2 Q_a^{(4)} + \alpha_{FPU}A_{a,b,c}\left[Q_b^{(0)}Q_c^{(3)} + Q_b^{(1)}Q_c^{(2)} + Q_b^{(2)}Q_c^{(1)} + Q_b^{(3)}Q_c^{(0)}\right] = P_D\cos\left(\frac{\omega_D}{\widetilde{\omega}_a}\tau_a\right) \tag{D.20}$$

$$\omega_b^2\partial_{\tau_b}^2 Q_b^{(4)} + \widetilde{\omega}_{b,0}^2\partial_{\tau_b}^2 Q_b^{(4)} + \widetilde{\omega}_{b,1}^2\partial_{\tau_b}^2 Q_b^{(3)} + \widetilde{\omega}_{b,2}^2\partial_{\tau_b}^2 Q_b^{(2)} + \widetilde{\omega}_{b,3}^2\partial_{\tau_b}^2 Q_b^{(1)} + \widetilde{\omega}_{b,4}^2\partial_{\tau_b}^2 Q_b^{(0)} + \omega_b^2 Q_b^{(4)} + \alpha_{FPU}A_{b,a,c}\left[Q_a^{(0)}Q_c^{(3)} + Q_a^{(1)}Q_c^{(2)} + Q_a^{(2)}Q_c^{(1)} + Q_a^{(3)}Q_c^{(0)}\right] = 0 \tag{D.21}$$

$$\omega_c^2\partial_{\tau_c}^2 Q_c^{(4)} + \widetilde{\omega}_{c,0}^2\partial_{\tau_c}^2 Q_c^{(4)} + \widetilde{\omega}_{c,1}^2\partial_{\tau_c}^2 Q_c^{(3)} + \widetilde{\omega}_{c,2}^2\partial_{\tau_c}^2 Q_c^{(2)} + \widetilde{\omega}_{c,3}^2\partial_{\tau_c}^2 Q_c^{(1)} + \widetilde{\omega}_{c,4}^2\partial_{\tau_c}^2 Q_c^{(0)} + \omega_c^2 Q_c^{(4)} + \alpha_{FPU}A_{c,a,b}\left[Q_a^{(0)}Q_b^{(3)} + Q_a^{(1)}Q_b^{(2)} + Q_a^{(2)}Q_b^{(1)} + Q_a^{(3)}Q_b^{(0)}\right] = 0 \tag{D.22}$$

$Q_a^{(4)}$ and $Q_b^{(4)}$ will not contain any additional terms compared to $Q_a^{(3)}$ to $Q_b^{(3)}$ respectively.

$$\omega_a^2\partial_{\tau_a}^2 Q_a^{(5)} + \widetilde{\omega}_{a,0}^2\partial_{\tau_a}^2 Q_a^{(5)} + \widetilde{\omega}_{a,1}^2\partial_{\tau_a}^2 Q_a^{(4)} + \widetilde{\omega}_{a,2}^2\partial_{\tau_a}^2 Q_a^{(3)} + \widetilde{\omega}_{a,3}^2\partial_{\tau_a}^2 Q_a^{(2)} + \widetilde{\omega}_{a,4}^2\partial_{\tau_a}^2 Q_a^{(1)} + \widetilde{\omega}_{a,5}^2\partial_{\tau_a}^2 Q_a^{(0)} + \omega_a^2 Q_a^{(5)} + \alpha_{FPU}A_{a,b,c}\left[Q_b^{(0)}Q_c^{(4)} + Q_b^{(1)}Q_c^{(3)} + Q_b^{(2)}Q_c^{(2)} + Q_b^{(3)}Q_c^{(1)} + Q_b^{(4)}Q_c^{(0)}\right] = P_D\cos\left(\frac{\omega_D}{\widetilde{\omega}_a}\tau_a\right) \tag{D.23}$$

$$\omega_b^2\partial_{\tau_b}^2 Q_b^{(5)} + \widetilde{\omega}_{b,0}^2\partial_{\tau_b}^2 Q_b^{(5)} + \widetilde{\omega}_{b,1}^2\partial_{\tau_b}^2 Q_b^{(4)} + \widetilde{\omega}_{b,2}^2\partial_{\tau_b}^2 Q_b^{(3)} + \widetilde{\omega}_{b,3}^2\partial_{\tau_b}^2 Q_b^{(2)} + \widetilde{\omega}_{b,4}^2\partial_{\tau_b}^2 Q_b^{(1)} + \widetilde{\omega}_{b,5}^2\partial_{\tau_b}^2 Q_b^{(0)} + \omega_b^2 Q_b^{(5)} + \alpha_{FPU}A_{b,a,c}\left[Q_a^{(0)}Q_c^{(4)} + Q_a^{(1)}Q_c^{(3)} + Q_a^{(2)}Q_c^{(2)} + Q_a^{(3)}Q_c^{(1)} + Q_a^{(4)}Q_c^{(0)}\right] = 0 \tag{D.24}$$

$$\omega_c^2\partial_{\tau_c}^2 Q_c^{(5)} + \widetilde{\omega}_{c,0}^2\partial_{\tau_c}^2 Q_c^{(5)} + \widetilde{\omega}_{c,1}^2\partial_{\tau_c}^2 Q_c^{(4)} + \widetilde{\omega}_{c,2}^2\partial_{\tau_c}^2 Q_c^{(3)} + \widetilde{\omega}_{c,3}^2\partial_{\tau_c}^2 Q_c^{(2)} + \widetilde{\omega}_{c,4}^2\partial_{\tau_c}^2 Q_c^{(1)} + \widetilde{\omega}_{c,5}^2\partial_{\tau_c}^2 Q_c^{(0)} + \omega_c^2 Q_c^{(5)} + \alpha_{FPU}A_{c,a,b}\left[Q_a^{(0)}Q_b^{(4)} + Q_a^{(1)}Q_b^{(3)} + Q_a^{(2)}Q_b^{(2)} + Q_a^{(3)}Q_b^{(1)} + Q_a^{(4)}Q_b^{(0)}\right] = 0 \quad \text{(D.25)}$$

$Q_a^{(5)}$ will contain the tone $\cos\big((2\omega_D - \widetilde{\omega}_a)t\big) = \cos\Big(\big(\widetilde{\omega}_a + 2(\omega_D - \widetilde{\omega}_a)\big)t\Big)$ in addition to $\cos(\widetilde{\omega}_a t)$ and $\cos(\omega_D t) = \cos\Big(\big(\widetilde{\omega}_a + (\omega_D - \widetilde{\omega}_a)\big)t\Big)$ and is generated through $Q_b^{(2)}Q_c^{(2)}$. $Q_b^{(5)}$ and $Q_c^{(5)}$ will not contain any additional tones compared to $Q_b^{(4)}$ and $Q_c^{(4)}$ respectively.

$$\omega_a^2\partial_{\tau_a}^2 Q_a^{(6)} + \widetilde{\omega}_{a,0}^2\partial_{\tau_a}^2 Q_a^{(6)} + \widetilde{\omega}_{a,1}^2\partial_{\tau_a}^2 Q_a^{(5)} + \widetilde{\omega}_{a,2}^2\partial_{\tau_a}^2 Q_a^{(4)} + \widetilde{\omega}_{a,3}^2\partial_{\tau_a}^2 Q_a^{(3)} + \widetilde{\omega}_{a,4}^2\partial_{\tau_a}^2 Q_a^{(2)} + \widetilde{\omega}_{a,5}^2\partial_{\tau_a}^2 Q_a^{(1)} + \widetilde{\omega}_{a,6}^2\partial_{\tau_a}^2 Q_a^{(0)} + \omega_a^2 Q_a^{(6)} + \alpha_{FPU}A_{a,b,c}\left[Q_b^{(0)}Q_c^{(5)} + Q_b^{(1)}Q_c^{(4)} + Q_b^{(2)}Q_c^{(3)} + Q_b^{(3)}Q_c^{(2)} + Q_b^{(4)}Q_c^{(1)} + Q_b^{(5)}Q_c^{(0)}\right] = P_D\cos\left(\frac{\omega_D}{\widetilde{\omega}_a}\tau_a\right) \quad \text{(D.26)}$$

$$\omega_b^2\partial_{\tau_b}^2 Q_b^{(6)} + \widetilde{\omega}_{b,0}^2\partial_{\tau_b}^2 Q_b^{(6)} + \widetilde{\omega}_{b,1}^2\partial_{\tau_b}^2 Q_b^{(5)} + \widetilde{\omega}_{b,2}^2\partial_{\tau_b}^2 Q_b^{(4)} + \widetilde{\omega}_{b,3}^2\partial_{\tau_b}^2 Q_b^{(3)} + \widetilde{\omega}_{b,4}^2\partial_{\tau_b}^2 Q_b^{(2)} + \widetilde{\omega}_{b,5}^2\partial_{\tau_b}^2 Q_b^{(1)} + \widetilde{\omega}_{b,6}^2\partial_{\tau_b}^2 Q_b^{(0)} + \omega_b^2 Q_b^{(6)} + \alpha_{FPU}A_{b,a,c}\left[Q_a^{(0)}Q_c^{(5)} + Q_a^{(1)}Q_c^{(4)} + Q_a^{(2)}Q_c^{(3)} + Q_a^{(3)}Q_c^{(2)} + Q_a^{(4)}Q_c^{(1)} + Q_b^{(5)}Q_c^{(0)}\right] = 0 \quad \text{(D.27)}$$

$$\omega_c^2\partial_{\tau_c}^2 Q_c^{(6)} + \widetilde{\omega}_{c,0}^2\partial_{\tau_c}^2 Q_c^{(6)} + \widetilde{\omega}_{c,1}^2\partial_{\tau_c}^2 Q_c^{(5)} + \widetilde{\omega}_{c,2}^2\partial_{\tau_c}^2 Q_c^{(4)} + \widetilde{\omega}_{c,3}^2\partial_{\tau_c}^2 Q_c^{(3)} + \widetilde{\omega}_{c,4}^2\partial_{\tau_c}^2 Q_c^{(2)} + \widetilde{\omega}_{c,5}^2\partial_{\tau_c}^2 Q_c^{(1)} + \widetilde{\omega}_{c,6}^2\partial_{\tau_c}^2 Q_c^{(0)} + \omega_c^2 Q_c^{(6)} + \alpha_{FPU}A_{c,a,b}\left[Q_a^{(0)}Q_b^{(5)} + Q_a^{(1)}Q_b^{(4)} + Q_a^{(2)}Q_b^{(3)} + Q_a^{(3)}Q_b^{(2)} + Q_a^{(4)}Q_b^{(1)} + Q_a^{(5)}Q_b^{(0)}\right] = 0 \quad \text{(D.28)}$$

$Q_a^{(6)}$ will not contain any additional tones compared to $Q_a^{(5)}$. However, $Q_b^{(6)}$ will contain an additional tone of $\cos\Big(\big(\omega_m - (\omega_D - \widetilde{\omega}_a)\big)t\Big)$ through the term $Q_a^{(3)}Q_c^{(2)}$ and $Q_c^{(6)}$ will contain an additional tone of $\cos\Big(\big(\omega_n - (\omega_D - \widetilde{\omega}_a)\big)t\Big)$ through the term $Q_a^{(3)}Q_b^{(2)}$.

$$\begin{aligned}\omega_a^2\partial_{\tau_a}^2 Q_a^{(7)} + \widetilde{\omega}_{a,0}^2\partial_{\tau_a}^2 Q_a^{(7)} + \widetilde{\omega}_{a,1}^2\partial_{\tau_a}^2 Q_a^{(6)} + \widetilde{\omega}_{a,2}^2\partial_{\tau_a}^2 Q_a^{(5)} + \widetilde{\omega}_{a,3}^2\partial_{\tau_a}^2 Q_a^{(4)} + \widetilde{\omega}_{a,4}^2\partial_{\tau_a}^2 Q_a^{(3)} \\ + \widetilde{\omega}_{a,5}^2\partial_{\tau_a}^2 Q_a^{(2)} + \widetilde{\omega}_{a,6}^2\partial_{\tau_a}^2 Q_a^{(1)} + \widetilde{\omega}_{a,7}^2\partial_{\tau_a}^2 Q_a^{(0)} + \omega_a^2 Q_a^{(7)} \\ + \alpha_{FPU}A_{a,b,c}\left[Q_b^{(0)}Q_c^{(6)} + Q_b^{(1)}Q_c^{(5)} + Q_b^{(2)}Q_c^{(4)} + Q_b^{(3)}Q_c^{(3)} + Q_b^{(4)}Q_c^{(2)}\right. \\ \left. + Q_b^{(5)}Q_c^{(1)} + Q_b^{(6)}Q_c^{(0)}\right] = P_D\cos\left(\frac{\omega_D}{\widetilde{\omega}_a}\tau_a\right)\end{aligned} \tag{D.29}$$

$$\begin{aligned}\omega_b^2\partial_{\tau_b}^2 Q_b^{(7)} + \widetilde{\omega}_{b,0}^2\partial_{\tau_b}^2 Q_b^{(7)} + \widetilde{\omega}_{b,1}^2\partial_{\tau_b}^2 Q_b^{(6)} + \widetilde{\omega}_{b,2}^2\partial_{\tau_b}^2 Q_b^{(5)} + \widetilde{\omega}_{b,3}^2\partial_{\tau_b}^2 Q_b^{(4)} + \widetilde{\omega}_{b,4}^2\partial_{\tau_b}^2 Q_b^{(3)} \\ + \widetilde{\omega}_{b,5}^2\partial_{\tau_b}^2 Q_b^{(2)} + \widetilde{\omega}_{b,6}^2\partial_{\tau_b}^2 Q_b^{(1)} + \widetilde{\omega}_{b,7}^2\partial_{\tau_b}^2 Q_b^{(0)} + \omega_b^2 Q_b^{(7)} \\ + \alpha_{FPU}A_{b,a,c}\left[Q_a^{(0)}Q_c^{(6)} + Q_a^{(1)}Q_c^{(5)} + Q_a^{(2)}Q_c^{(4)} + Q_a^{(3)}Q_c^{(3)} + Q_a^{(4)}Q_c^{(2)}\right. \\ \left. + Q_b^{(5)}Q_c^{(1)} + Q_b^{(6)}Q_c^{(0)}\right] = 0\end{aligned} \tag{D.30}$$

$$\begin{aligned}\omega_c^2\partial_{\tau_c}^2 Q_c^{(7)} + \widetilde{\omega}_{c,0}^2\partial_{\tau_c}^2 Q_c^{(7)} + \widetilde{\omega}_{c,1}^2\partial_{\tau_c}^2 Q_c^{(6)} + \widetilde{\omega}_{c,2}^2\partial_{\tau_c}^2 Q_c^{(5)} + \widetilde{\omega}_{c,3}^2\partial_{\tau_c}^2 Q_c^{(4)} + \widetilde{\omega}_{c,4}^2\partial_{\tau_c}^2 Q_c^{(3)} \\ + \widetilde{\omega}_{c,5}^2\partial_{\tau_c}^2 Q_c^{(2)} + \widetilde{\omega}_{c,6}^2\partial_{\tau_c}^2 Q_c^{(1)} + \widetilde{\omega}_{c,7}^2\partial_{\tau_c}^2 Q_c^{(0)} + \omega_c^2 Q_c^{(7)} \\ + \alpha_{FPU}A_{c,a,b}\left[Q_a^{(0)}Q_b^{(6)} + Q_a^{(1)}Q_b^{(5)} + Q_a^{(2)}Q_b^{(4)} + Q_a^{(3)}Q_b^{(3)} + Q_a^{(4)}Q_b^{(2)}\right. \\ \left. + Q_a^{(5)}Q_b^{(1)} + Q_a^{(6)}Q_b^{(0)}\right] = 0\end{aligned} \tag{D.31}$$

$Q_a^{(7)}$ will not contain any additional tones compared to $Q_a^{(6)}$. However, $Q_b^{(7)}$ will contain an additional tone of $\cos\left(\left(\omega_m + 2(\omega_D - \widetilde{\omega}_a)\right)t\right)$ through the term $Q_a^{(5)}Q_c^{(1)}$ and $Q_c^{(7)}$ will contain an additional tone of $\cos\left(\left(\omega_n + 2(\omega_D - \widetilde{\omega}_a)\right)t\right)$ through the term $Q_a^{(5)}Q_b^{(1)}$.

Hence, $Q_a^{(7)}$ will consist of the tones $\cos(\widetilde{\omega}_a t)$, $\cos\left(\left(\widetilde{\omega}_a + (\omega_D - \widetilde{\omega}_a)\right)t\right)$ and $\cos\left(\left(\widetilde{\omega}_a + 2(\omega_D - \widetilde{\omega}_a)\right)t\right)$, $Q_b^{(7)}$ will consist of the tones $\cos\left(\left(\omega_m - (\omega_D - \widetilde{\omega}_a)\right)t\right)$, $\cos(\omega_m t)$, $\cos\left(\left(\omega_m + (\omega_D - \widetilde{\omega}_a)\right)t\right)$ and $\cos\left(\left(\omega_m + 2(\omega_D - \widetilde{\omega}_a)\right)t\right)$ and $Q_c^{(7)}$ will consist of the tones $\cos\left(\left(\omega_n - (\omega_D - \widetilde{\omega}_a)\right)t\right)$, $\cos(\widetilde{\omega}_n t)$, $\cos\left(\left(\omega_n + (\omega_D - \widetilde{\omega}_a)\right)t\right)$ and $\cos\left(\left(\omega_n + 2(\omega_D - \widetilde{\omega}_a)\right)t\right)$.

$$\begin{aligned}\omega_a^2\partial_{\tau_a}^2 Q_a^{(n)} + \sum_{n_1+n_2=n}\widetilde{\omega}_{a,n_1}^2\partial_{\tau_a}^2 Q_a^{(n_2)} + \omega_a^2 Q_a^{(n)} + \alpha_{FPU}A_{a,b,c}\sum_{n_1+n_2=n-1}Q_b^{(n_1)}Q_c^{(n_2)} \\ = P_D\cos\left(\frac{\omega_D}{\widetilde{\omega}_a}\tau_a\right)\end{aligned} \tag{D.32}$$

$$\omega_b^2\partial_{\tau_b}^2 Q_b^{(n)} + \sum_{n_1+n_2=n}\widetilde{\omega}_{b,n_1}^2\partial_{\tau_b}^2 Q_b^{(n_2)} + \omega_b^2 Q_b^{(n)} + \alpha_{FPU}A_{b,a,c}\sum_{n_1+n_2=n-1}Q_a^{(n_1)}Q_c^{(n_2)} = 0 \tag{D.33}$$

$$\omega_c^2\partial_{\tau_c}^2 Q_c^{(n)} + \sum_{n_1+n_2=n}\widetilde{\omega}_{c,n_1}^2\partial_{\tau_c}^2 Q_c^{(n_2)} + \omega_c^2 Q_c^{(n)} + \alpha_{FPU}A_{c,a,b}\sum_{n_1+n_2=n-1}Q_a^{(n_1)}Q_b^{(n_2)} = 0 \tag{D.34}$$

By sequentially solving the equations D.32-D.34, high-order solutions $Q_a^{(n>7)}$, $Q_b^{(n>7)}$ and $Q_c^{(n>7)}$ can be obtained. Through these iterations, a series of near-resonant tones $\cos\left(\left(\widetilde{\omega}_a \pm p(\omega_D - \widetilde{\omega}_a)\right)t\right), \cos\left(\left(\omega_m \pm p(\omega_D - \widetilde{\omega}_a)\right)t\right)$ & $\cos\left(\left(\omega_n \pm p(\omega_D - \widetilde{\omega}_a)\right)t\right); p \in Z$ can be generated. Hence, the general solutions for Q_a, Q_b and Q_c are given by

$$Q_a = A_0^{(a)}\cos(\widetilde{\omega}_a t) + \sum_{p\neq 0} A_p^{(a)}\cos\left((\widetilde{\omega}_a + p\Delta\omega)t\right) \tag{D.35}$$

$$Q_b = A_0^{(b)}\cos(\omega_m t) + \sum_{p\neq 0} A_p^{(b)}\cos\left((\omega_m + p\Delta\omega)t\right) \tag{D.36}$$

$$Q_c = A_0^{(c)}\cos(\omega_n t) + \sum_{p\neq 0} A_p^{(c)}\cos\left((\omega_n + p\Delta\omega)t\right) \tag{D.37}$$

with the amplitude:

$$\left|A_p^{(a)}\right| \sim [(\widetilde{\omega}_a^2 - (\widetilde{\omega}_a + p\Delta\omega)^2)^2 + 4\zeta_a^2(\widetilde{\omega}_a + p\Delta\omega)^2]^{-\frac{1}{2}}; \left|A_p^{(b)}\right| \sim \left[\left(\widetilde{\omega}_b^2 - (\omega_m + p\Delta\omega)^2\right)^2 + 4\zeta_b^2(\omega_m + p\Delta\omega)^2\right]^{-\frac{1}{2}}; \left|A_p^{(c)}\right| \sim [(\widetilde{\omega}_c^2 - (\omega_n + p\Delta\omega)^2)^2 + 4\zeta_c^2(\omega_n + p\Delta\omega)^2]^{-\frac{1}{2}}; p \in Z$$

and the frequency spacing: $\Delta\omega = |\omega_D - \widetilde{\omega}_a|$. It should be noted that $\widetilde{\omega}_a$, ω_m and ω_n can be drive amplitude dependent. While it is difficult to derive an analytical expression for such dependences by PL method, these can be understood by phenomenology. As shown in Figure 5.18, $\widetilde{\omega}_a$ linearly increases with the electrical drive power level S_{in}. On the other hand, there exists a nonlinear relationship between $\omega_{m(n)}$ with S_{in} (Figure 5.17).

References

Chapter 1: Introduction

[1] T. Udem, R. Holzwarth, and T. W. Hansch, "Optical frequency metrology," *Nature,* vol. 416, pp. 233-237, 2002.

[2] S. T. Cundiff and J. Ye, "Colloquium: Femtosecond optical frequency combs," *Reviews of Modern Physics,* vol. 75, p. 325, 2003.

[3] T. W. Haensch, "Measuring the frequency of light with ultrashort pulses," in *Lasers and Electro-Optics, 2001. CLEO'01. Technical Digest. Summaries of papers presented at the Conference on*, 2001, pp. 507-508.

[4] J.L. Hall. Defining and measuring optical frequencies. Nobel Lecture, 8 Dec. 2005, available at: http://nobelprize.org/physics/laureates/2005/hall-lecture.html

[5] S.T. Cundiff and L. Hollberg. Absolute Optical Frequency Metrology in *Encyclopedia of Modern Optics* (.pdf; download Acrobat Reader)(link is external), B.D. Guenther and D.G. Steel, eds, (Academic Press, 2004).

[6] D. J. Jones, S. A. Diddams, J. K. Ranka, A. Stentz, R. S. Windeler, J. L. Hall, and S. T. Cundiff, "Carrier-envelope phase control of femtosecond mode-locked lasers and direct optical frequency synthesis," *Science,* vol. 288, pp. 635-639, 200

[7] S. T. Cundiff, "Metrology: new generation of combs," *Nature,* vol. 450, pp. 1175-1176, 2007.

[8] P. Del'Haye, A. Schliesser, O. Arcizet, T. Wilken, R. Holzwarth, and T. J. Kippenberg, "Optical frequency comb generation from a monolithic microresonator," *Nature,* vol. 450, pp. 1214-1217, 2007.

[9] P. J. Delfyett, I. Ozdur, N. Hoghooghi, M. Akbulut, J. Davila-Rodriguez, and S. Bhooplapur, "Advanced ultrafast technologies based on optical frequency combs," *IEEE Journal of Selected Topics in Quantum Electronics,* vol. 18, pp. 258-274, 2012.

[10] T. Steinmetz, T. Wilken, C. Araujo-Hauck, R. Holzwarth, T. W. Hansch, L. Pasquini, A. Manescau, S. D'Odorico, M. T. Murphy, and T. Kentischer, "Laser frequency combs for astronomical observations," *Science,* vol. 321, pp. 1335-1337, 2008.

[11] M. Takamoto, H. Feng-Lei, R. Higashi, and H. Katori, "An optical lattice clock," *Nature,* vol. 435, p. 321, 2005.

[12] T. W. Hansch, "Nobel lecture: passion for precision," *Reviews of Modern Physics,* vol. 78, p. 1297, 2006.

[13] A. Ganesan, C. Do, and A. Seshia, "Phononic Frequency Comb via Intrinsic Three-Wave Mixing," *Physical review letters,* vol. 118, p. 033903, 2017.

[14] L. S. Cao, D. X. Qi, R. W. Peng, M. Wang, and P. Schmelcher, "Phononic Frequency Combs through Nonlinear Resonances," *Physical review letters,* vol. 112, p. 075505, 2014.

[15] "Optical Frequency Combs", https://www.nist.gov/director/pao/optical-frequency-combs

Chapter 2: Established Resonant Phenomena

[16] L. Rayleigh, "XVIII. Acoustical notes VIII," *The London, Edinburgh, and Dublin Philosophical Magazine and Journal of Science,* vol. 16, pp. 235-246, 1908.

[17] S. Spinner, "A method for determining mechanical resonance frequencies and for calculation elastic moduli from these frequencies," in *Proc. ASTM*, 1961, pp. 1221-1238.

[18] K. Y. Billah and R. H. Scanlan, "Resonance, Tacoma Narrows bridge failure, and undergraduate physics textbooks," *American Journal of Physics,* vol. 59, pp. 118-124, 1991.

[19] M. Tooley, *Electronic Circuits-Fundamentals & Applications*: Routledge, 2007.

[20] L. Rayleigh, "CXII. The problem of the whispering gallery," *The London, Edinburgh, and Dublin Philosophical Magazine and Journal of Science,* vol. 20, pp. 1001-1004, 1910.

[21] C. V. Raman and G. A. Sutherland, "On the whispering-gallery phenomenon," *Proceedings of the Royal Society of London. Series A, Containing Papers of a Mathematical and Physical Character,* vol. 100, pp. 424-428, 1922.

[22] A. E. Siegman, "Laser beams and resonators: beyond the 1960s," *IEEE Journal of Selected Topics in Quantum Electronics,* vol. 6, pp. 1389-1399, 2000.

[23] A. E. Roy, *Orbital motion*: CRC Press, 2004.

[24] E. Zavoisky, "Spin-magnetic resonance in paramagnetics," *J Phys USSR,* vol. 9, pp. 211-245, 1945.

[25] P. Slichter Charles, "Principles of Magnetic Resonance: with Examples from Solid State Physics," Harper & Row Publishers, 1963.

[26] G. Duffing, *Erzwungene Schwingungen bei veranderlicher Eigenfrequenz und ihre technische Bedeutung*: R, Vieweg & Sohn, 1918.

[27] M. Kumar, B. Choubey, and H. Bhaskaran, "Nanomechanical resonators show higher order nonlinearity at room temperature," *arXiv preprint arXiv:1703.03094,* 2017.

[28] M. Faraday, "On a peculiar class of acoustical figures; and on certain forms assumed by groups of particles upon vibrating elastic surfaces," *Philosophical transactions of the Royal Society of London,* vol. 121, pp. 299-340, 1831.

Chapter 3: Fermi-Pasta-Ulam Chains and Phononic Frequency Combs

[29] I. E. Fermi, P. Pasta, S. Ulam, and M. Tsingou, "Studies of the nonlinear problems," Los Alamos Scientific Lab., N. Mex. 1955.

[30] M. Onorato, L. Vozella, D. Proment, and Y. V. Lvov, "Route to thermalization in the α-Fermi-Pasta-Ulam system," *Proceedings of the National Academy of Sciences,* vol. 112, pp. 4208-4213, 2015.

[31] N. J. Zabusky, Z. Sun, and G. Peng, "Measures of chaos and equipartition in integrable and nonintegrable lattices," *Chaos: An Interdisciplinary Journal of Nonlinear Science,* vol. 16, p. 013130, 2006.

[32] G. Miloshevich, R. Khomeriki, and S. Ruffo, "Stochastic resonance in the Fermi-Pasta-Ulam chain," *Physical review letters,* vol. 102, p. 020602, 2009.

[33] S. Flach, M. V. Ivanchenko, and O. I. Kanakov, "q-Breathers and the Fermi-Pasta-Ulam problem," *Physical review letters,* vol. 95, p. 064102, 2005.

[34] N. Li, B. Li, and S. Flach, "Energy carriers in the Fermi-Pasta-Ulam β-lattice: Solitons or Phonons?," *Physical review letters,* vol. 105, p. 054102, 2010.

[35] P. Poggi and S. Ruffo, "Exact solutions in the FPU oscillator chain," *Physica D: Nonlinear Phenomena,* vol. 103, pp. 251-272, 1997.

[36] S. Flach, M. V. Ivanchenko, O. I. Kanakov, and K. G. Mishagin, "Periodic orbits, localization in normal mode space, and the Fermi-Pasta-Ulam problem," *American Journal of Physics,* vol. 76, pp. 453-459, 2008.

[37] K. i. Fukamachi, "1/f fluctuations in FPU lattices," *EPL (Europhysics Letters),* vol. 26, p. 449, 1994.

[38] G. P. Drago and S. Ridella, "Some more observations on the superperiod of the non-linear FPU system," *Physics Letters A,* vol. 122, pp. 407-412, 1987.

[39] G. M. Zaslavsky, "Long way from the FPU-problem to chaos," *Chaos: An Interdisciplinary Journal of Nonlinear Science,* vol. 15, p. 015103, 2005.

[40] G. M. Chechin, N. V. Novikova, and A. A. Abramenko, "Bushes of vibrational modes for Fermi-Pasta-Ulam chains," *Physica D: Nonlinear Phenomena,* vol. 166, pp. 208-238, 2002.

[41] D. Campbell, D. Farmer, J. Crutchfield, and E. Jen, "Experimental mathematics: the role of computation in nonlinear science," *Communications of the ACM,* vol. 28, pp. 374-384, 1985.

[42] D. K. Campbell, P. Rosenau, and G. M. Zaslavsky, "Introduction: the Fermi-Pasta-Ulam problem - the first fifty years," *Chaos: An Interdisciplinary Journal of Nonlinear Science,* vol. 15, p. 015101, 2005.

Chapter 4: Micromechanical Resonator – An Experimental Analogue of Fermi-Pasta-Ulam Chains

[43] I. Zlatev, G. Huey, and P. J. Steinhardt, "Parametric resonance in an expanding universe," *Physical Review D,* vol. 57, p. 2152, 1998.

[44] S. Mukohyama, "Excitation of a Kaluza-Klein mode by parametric resonance," *Physical Review D,* vol. 57, p. 6191, 1998.

[45] D. Moss, "Parametric resonance and bisymmetric dynamo solutions in spiral galaxies," *Astronomy and Astrophysics,* vol. 308, pp. 381-386, 1996.

[46] P. M. Gresho and R. L. Sani, "The effects of gravity modulation on the stability of a heated fluid layer," *Journal of Fluid Mechanics,* vol. 40, pp. 783-806, 1970.

[47] G. Ahlers, P. C. Hohenberg, and M. Lacke, "Thermal convection under external modulation of the driving force. I. The Lorenz model," *Physical Review A,* vol. 32, p. 3493, 1985.

[48] J. W. Miles, "Parametrically excited solitary waves," *Journal of Fluid Mechanics,* vol. 148, pp. 451-460, 1984.

[49] H. Suhl, "The theory of ferromagnetic resonance at high signal powers," *Journal of Physics and Chemistry of Solids,* vol. 1, pp. 209-227, 1957.

[50] I. A. Aronov, O. N. Baranets, and M. O. Osmanov, "Gunn effect under conditions of cyclotron parametric resonance," *Physics Letters A,* vol. 146, pp. 141-146, 1990.

[51] R. L. Byer, "Optical parametric oscillators," *Quantum Electronics: A Treatise,* vol. 1, 1975.

[52] M. H. Dunn and M. Ebrahimzadeh, "Parametric generation of tunable light from continuous-wave to femtosecond pulses," *Science,* vol. 286, pp. 1513-1517, 1999.

[53] A. H. Nayfeh and D. T. Mook, *Nonlinear oscillations*: John Wiley & Sons, 2008.

[54] K. L. Turner, S. A. Miller, P. G. Hartwell, and N. C. MacDonald, "Five parametric resonances in a microelectromechanical system," *Nature,* vol. 396, p. 149, 1998.

[55] D. W. Carr, S. Evoy, L. Sekaric, H. G. Craighead, and J. M. Parpia, "Parametric amplification in a torsional microresonator," *Applied Physics Letters,* vol. 77, pp. 1545-1547, 2000.

[56] R. B. Karabalin, X. L. Feng, and M. L. Roukes, "Parametric nanomechanical amplification at very high frequency," *Nano letters,* vol. 9, pp. 3116-3123, 2009.

[57] A. Eichler, J. Chaste, J. Moser, and A. Bachtold, "Parametric amplification and self-oscillation in a nanotube mechanical resonator," *Nano letters,* vol. 11, pp. 2699-2703, 2011.

[58] Y. Jia, S. Du, and A. A. Seshia, "Twenty-eight orders of parametric resonance in a microelectromechanical device for multi-band vibration energy harvesting," *Scientific reports,* vol. 6, p. 30167, 2017.

[59] A. Ganesan, C. Do, and A. Seshia, "Observation of three-mode parametric instability in a micromechanical resonator," *Applied Physics Letters,* vol. 109, p. 193501, 2016.

[60] A. Ganesan, C. Do, and A. Seshia, "Excitation of multiple 2-mode parametric resonances by a single driven mode," *Europhysics Letters,* vol. 119, p. 10002, 2017.

[61] M. J. Seitner, M. Abdi, A. Ridolfo, M. J. Hartmann, and E. M. Weig, "Parametric Oscillation, Frequency Mixing, and Injection Locking of Strongly Coupled Nanomechanical Resonator Modes," *Physical review letters,* vol. 118, p. 254301, 2017.

[62] A. Ganesan, C. Do, and A. Seshia, "Towards N-mode parametric electromechanical resonances," *arXiv preprint arXiv:1708.01660,* 2017.

[63] N. I. Markevich and E. E. Sel'kov, "Parametric resonance and amplification in excitable membranes. The Hodgkin-Huxley model," *Journal of theoretical biology,* vol. 140, pp. 27-38, 1989.

[64] M. Schienbein and H. Gruler, "Enzyme kinetics, self-organized molecular machines, and parametric resonance," *Physical Review E,* vol. 56, p. 7116, 1997.

[65] C.-C. Nguyen and R. T. Howe, "CMOS micromechanical resonator oscillator," in *Electron Devices Meeting, 1993. IEDM'93. Technical Digest., International*, 1993, pp. 199-202.

[66] B. Ha, Y. Oh, and C. Song, "A capacitive silicon microaccelerometer with force-balancing electrodes," *Japanese journal of applied physics,* vol. 37, p. 7052, 1998.

[67] J. E. Y. Lee, B. Bahreyni, Y. Zhu, and A. A. Seshia, "A single-crystal-silicon bulk-acoustic-mode microresonator oscillator," *IEEE Electron Device Letters,* vol. 29, pp. 701-703, 2008.

[68] J. E. Y. Lee, J. Yan, and A. A. Seshia, "Low loss HF band SOI wine glass bulk mode capacitive square-plate resonator," *Journal of Micromechanics and Microengineering,* vol. 19, p. 074003, 2009.

[69] D. L. DeVoe, "Piezoelectric thin film micromechanical beam resonators," *Sensors and Actuators A: Physical,* vol. 88, pp. 263-272, 2001.

[70] G. Piazza, P. J. Stephanou, J. M. Porter, M. B. J. Wijesundara, and A. P. Pisano, "Low motional resistance ring-shaped contour-mode aluminum nitride piezoelectric micromechanical resonators for UHF applications," in *Micro Electro Mechanical Systems, 2005. MEMS 2005. 18th IEEE International Conference on*, 2005, pp. 20-23.

[71] G. K. Ho, R. Abdolvand, A. Sivapurapu, S. Humad, and F. Ayazi, "Piezoelectric-on-silicon lateral bulk acoustic wave micromechanical resonators," *Journal of microelectromechanical systems,* vol. 17, pp. 512-520, 2008.

[72] Y. Hui, Z. Qian, and M. Rinaldi, "A 2.8 GHz combined mode of vibration aluminum nitride MEMS resonator with high figure of merit exceeding 45," in *European Frequency and Time Forum & International Frequency Control Symposium (EFTF/IFC), 2013 Joint*, 2013, pp. 930-932.

[73] "Piezoelectric Simulations," https://cdn.comsol.com/wordpress/2014/12/Piezo_COMSOL_50.compressed.pdf

[74] A. Cowen, G. Hames, K. Glukh, and B. Hardy, "PiezoMUMPs design handbook," *MEMSCAP Inc,* 2014.

[75] L. L. P. Wong, S. Na, A. I. Chen, Z. Li, M. Macecek, and J. T. W. Yeow, "A feasibility study of piezoelectric micromachined ultrasonic transducers fabrication using a multi-user MEMS process," *Sensors and Actuators A: Physical,* vol. 247, pp. 430-439, 2016.

Chapter 5: Observation of Phononic Frequency Combs in a Micromechanical Resonator

[76] A. Ganesan, C. Do, and A. A. Seshia, "Phononic four-wave mixing," *arXiv preprint arXiv:1610.08008,* 2016.

[77] A. Ganesan, C. Do, and A. Seshia, "Frequency transitions in phononic four-wave mixing," *Applied Physics Letters,* vol. 111, p. 064101, 2017.

[78] A. Ganesan, C. Do, and A. Seshia, "Phononic frequency comb via three-mode parametric resonance," *Applied Physics Letters,* vol. 112, p. 021906, 2018.

Chapter 7: Future Work

[79] A. Ganesan, C. Do, and A. Seshia, "Excitation of coupled phononic frequency combs via two-mode parametric three-wave mixing," *Physical Review B,* vol. 97, p. 014302, 2018.

[80] D. K. Agrawal, J. Woodhouse, and A. A. Seshia, "Observation of locked phase dynamics and enhanced frequency stability in synchronized micromechanical oscillators," *Physical review letters,* vol. 111, p. 084101, 2017.

[81] P. Thiruvenkatanathan, J. Woodhouse, J. Yan, and A. A. Seshia, "Manipulating vibration energy confinement in electrically coupled microelectromechanical resonator arrays," *Journal of microelectromechanical systems,* vol. 20, pp. 157-164, 2017.

[82] D. S. Greywall and P. A. Busch, "Coupled micromechanical drumhead resonators with practical application as electromechanical bandpass filters," *Journal of Micromechanics and Microengineering,* vol. 12, p. 925, 2002.

[83] E. Buks and M. L. Roukes, "Electrically tunable collective response in a coupled micromechanical array," *Journal of microelectromechanical systems,* vol. 11, pp. 802-807, 2002.

[84] V. Kaajakari, J. K. Koskinen, and T. Mattila, "Phase noise in capacitively coupled micromechanical oscillators," *IEEE transactions on ultrasonics, ferroelectrics, and frequency control,* vol. 52, pp. 2322-2331, 2005.

[85] H. J. R. Westra, M. Poot, H. S. J. Van Der Zant, and W. J. Venstra, "Nonlinear modal interactions in clamped-clamped mechanical resonators," *Physical review letters,* vol. 105, p. 117205, 2010.

[86] A. Eichler, M. del Alamo Ruiz, J. A. Plaza, and A. Bachtold, "Strong coupling between mechanical modes in a nanotube resonator," *Physical review letters,* vol. 109, p. 025503, 2012.

[87] R. E. Rudd and J. Q. Broughton, "Atomistic simulation of MEMS resonators through the coupling of length scales," *J. Model. Simul. Microsyst,* vol. 1, pp. 29-38, 1999.

[88] J. Atalaya, A. Isacsson, and J. M. Kinaret, "Continuum elastic modeling of graphene resonators," *Nano letters,* vol. 8, pp. 4196-4200, 2008.

[89] M. Cross and H. Greenside, *Pattern formation and dynamics in nonequilibrium systems*: Cambridge University Press, 2009.

[90] Y. Bromberg, M. C. Cross, and R. Lifshitz, "Response of discrete nonlinear systems with many degrees of freedom," *Physical Review E,* vol. 73, p. 016214, 2006.

[91] G. Heinrich, M. Ludwig, J. Qian, B. Kubala, and F. Marquardt, "Collective dynamics in optomechanical arrays," *Physical review letters,* vol. 107, p. 043603, 2011.

[92] E. Kenig, R. Lifshitz, and M. C. Cross, "Pattern selection in parametrically driven arrays of nonlinear resonators," *Physical Review E,* vol. 79, p. 026203, 2009.

[93] C. T. C. Nguyen, "MEMS technology for timing and frequency control," *IEEE transactions on ultrasonics, ferroelectrics, and frequency control,* vol. 54, 2007.

[94] J. T. M. Van Beek and R. Puers, "A review of MEMS oscillators for frequency reference and timing applications," *Journal of Micromechanics and Microengineering,* vol. 22, p. 013001, 2011.

[95] Y. T. Yang, C. Callegari, X. L. Feng, K. L. Ekinci, and M. L. Roukes, "Zeptogram-scale nanomechanical mass sensing," *Nano letters,* vol. 6, pp. 583-586, 2006.

[96] J. L. Arlett, E. B. Myers, and M. L. Roukes, "Comparative advantages of mechanical biosensors," *Nature nanotechnology,* vol. 6, pp. 203-215, 2011.

[97] Y. Zhu, J. E. Y. Lee, and A. A. Seshia, "A resonant micromachined electrostatic charge sensor," *IEEE Sensors Journal,* vol. 8, pp. 1499-1505, 2008.

[98] A. N. Cleland and M. L. Roukes, "A nanometre-scale mechanical electrometer," *Nature,* vol. 392, p. 160, 1998.

[99] A. A. Seshia, R. T. Howe, and S. Montague, "An integrated microelectromechanical resonant output gyroscope," in *Micro Electro Mechanical Systems, 2002. The Fifteenth IEEE International Conference on*, 2002, pp. 722-726.

[100] R. P. Middlemiss, A. Samarelli, D. J. Paul, J. Hough, S. Rowan, and G. D. Hammond, "Measurement of the Earth tides with a MEMS gravimeter," *Nature,* vol. 531, pp. 614-617, 2016.

[101] Y. Hui, J. S. Gomez-Diaz, Z. Qian, A. Alu, and M. Rinaldi, "Plasmonic piezoelectric nanomechanical resonator for spectrally selective infrared sensing," *Nature communications,* vol. 7, 2016.

[102] A. A. Seshia, M. Palaniapan, T. A. Roessig, R. T. Howe, R. W. Gooch, T. R. Schimert, and S. Montague, "A vacuum packaged surface micromachined resonant accelerometer," *Journal of microelectromechanical systems,* vol. 11, pp. 784-793, 2002.

[103] C. M. Jha, G. Bahl, R. Melamud, S. A. Chandorkar, M. A. Hopcroft, B. Kim, M. Agarwal, J. Salvia, H. Mehta, and T. W. Kenny, "CMOS-compatible dual-resonator MEMS temperature sensor with milli-degree accuracy," in *Solid-State Sensors, Actuators and Microsystems Conference, 2007. TRANSDUCERS 2007. International*, 2007, pp. 229-232.

[104] D. Rugar, O. Zuger, S. Hoen, C. S. Yannoni, H. M. Vieth, and R. D. Kendrick, "Force detection of nuclear magnetic resonance," *Science,* pp. 1560-1563, 1994.

[105] A. C. Bleszynski-Jayich, W. E. Shanks, B. Peaudecerf, E. Ginossar, F. Von Oppen, L. Glazman, and J. G. E. Harris, "Persistent currents in normal metal rings," *Science,* vol. 326, pp. 272-275, 2009.

[106] C. Do, A. Ganesan, and A. A. Seshia, "Low power sub-milligram resonant MEMS load sensor," in *2017 19th International Conference on Solid-State Sensors, Actuators and Microsystems (TRANSDUCERS)*, 2017, pp. 974-977.

[107] E. H. Colpitts, "Oscillation generator." U.S. Patent 1,624,537, issued April 12, 1927.

[108] G. W. Pierce, "Piezoelectric crystal resonators and crystal oscillators applied to the precision calibration of wavemeters," in *Proceedings of the American Academy of Arts and Sciences*, 1923, pp. 81-106.

[109] D. B. Lesson, "A simple model of feedback oscillator noise spectrum," *Proc. IEEE,* vol. 54, pp. 329-330, 1966.

[110] E. Rubiola, *Phase noise and frequency stability in oscillators*: Cambridge University Press, 2008.

[111] R. B. Karabalin, M. C. Cross, and M. L. Roukes, "Nonlinear dynamics and chaos in two coupled nanomechanical resonators," *Physical Review B,* vol. 79, p. 165309, 2009.

[112] S. Tallur and S. A. Bhave, "Non-linear dynamics in opto-mechanical oscillators," in *Solid-State Sensors, Actuators and Microsystems (TRANSDUCERS), 2015 Transducers-2015 18th International Conference on*, 2015, pp. 993-996.

[113] N. Boechler, G. Theocharis, and C. Daraio, "Bifurcation-based acoustic switching and rectification," *Nature materials,* vol. 10, p. 665, 2011.